To the Graduate Council:

I am submitting herewith a dissertation written by Sean Robert Fischbach entitled "Streaming Effects in Liquid Injection Rocket Engines with Transverse Mode Oscillations." I have examined the final electronic copy of this dissertation for form and content and recommend that it be accepted in partial fulfillment of the requirements for the degree of Doctor of Philosophy, with a major in Aerospace Engineering.

_____
Dr. Joseph Majdalani, Major Professor

We have read this thesis
and recommend its acceptance:

_____
Dr. Gary Flandro

_____
Dr. Stephen Corda

Accepted for the Council:

_____
Dr. Kenneth Kimble

_____
Carolyn R. Hodges, Vice Provost and
Dean of the Graduate School

Streaming Effects in Liquid Injection Rocket Engines with Transverse Mode Oscillations

A Dissertation

Presented for the

Doctor of Philosophy

Degree

The University of Tennessee, Knoxville

Sean Robert Fischbach

December 2007

Acknowledgements

I would like to voice immense gratitude towards the faculty and staff of the University of Tennessee Space Institute. Dr. Majdalani deserves and is given my greatest respect and thanks. As my advisor he served as scientific tutor and literary editor. His skills with the pen and perturbation theories are matched by none and were crucial in the completion of my studies. The assistance of Dr. Kimble and Dr. Corda is also greatly valued. Dr. Kimble's abilities as a mathematician lent insight and rigor to the study. While, Dr. Corda's extensive work in the "real world" as well as the academic world supplied well posed and stimulating questions that help me in a more comprehensive understanding and thorough explanation of the analysis and its results. Dr. Flandro's experience with Combustion Instability spans many decades and his labors resonate within the community. Dr. Flandro's multiple suggestions and advice were essential to the successful completion of this analysis. His ability to draw a student to the correct conclusion without "selling the farm" is a skill that I can only hope to cultivate within myself.

The friends/colleagues that I have made at UTSI, the "varsity," are a testament to the uniqueness and possible greatness of the Space Institute. Joshua Batterson deserves considerable thanks for helping with my paperwork. Without his efforts I could not have completed my studies. My family has given me more love and encouragement than any one person could ever need. I could never thank them enough, but only hope that their investment in me pays bountiful dividends and that someday I may return the favor or at the least pass it on. Thank you mom and dad!

Abstract

This research is an analytical investigation of wave interactions in a simulated liquid rocket engine with uniform injection imposed at the faceplate. Of significant interest are the secondary nonlinear flows, particularly acoustic streaming, induced by transverse wave impingement over the engine injector surface. The corresponding cylindrical chamber has a small length-to-diameter ratio with respect to solid and hybrid rockets. Given their low chamber aspect ratios, liquid thrust engines are known to experience severe tangential and radial oscillation modes more often than longitudinal ones. Experimental evidence demonstrates the production of large peak-to-trough amplitude flow oscillations along with the development of a strong central vortex structure in many unstable liquid engines. These phenomena are accompanied by elevated heat transfer to the injector faceplates, strong roll torques and chamber over pressurization. In order to model this behavior, tangential and radial waves are superimposed onto a basic mean-flow model that consists of a steady, uniform axial velocity throughout the chamber. Considerable effort is given to correctly satisfy the no-slip condition at the chamber's injector face. The viscous boundary layer used to satisfy the no-slip condition is the location at which acoustic streaming develops. Sidewall boundary layers that develop at the lateral wall are not considered, being inconsequential to the flow in the vicinity of the headwall. Using perturbation tools, both potential and viscous flow equations are linearized in the pressure wave amplitude and solved to the second order. The effects of the headwall Mach number are leveraged as well. While the potential flow analysis does not predict

any acoustic streaming effects, the viscous solution carried out to the second-order approximation gives rise to steady secondary flow patterns near the headwall. These axisymmetric, steady contributions to the tangential and radial traveling waves are induced by the convective flow motion through interactions with inertial and viscous forces. Suppressing either the convective terms or viscosity at the headwall can lead to spurious solutions that are free from streaming. In the present research, streaming is initiated at the headwall, within the boundary layer, and extends throughout the chamber. The study suggests that nonlinear streaming effects of tangential and radial waves inside a cylinder with headwall injection act to alter the outer solution. As a result of streaming, the radial wave velocities are intensified in one half of the domain and reduced in the opposite half at any instant of time. Similarly, the tangential wave velocities are either enhanced or weakened in two opposing sectors that are at a 90 degree angle to the radial velocity counterparts. The second-order viscous solution that is obtained clearly displays both an oscillating and a steady flow component. It is found that the steady contribution due to streaming can potentially promote the development of large amplitude steepened wave forms. The delineation of this mechanism is crucial for the advancement of analytical tools employed in the prediction of combustion instability. In the present study, streaming is examined in the context of traveling transverse waves. Extending the analysis to standing wave motion is carried out and reported in a straightforward fashion.

Table of Contents

1. INTRODUCTION 1

1.1. Combustion Instability Overview 1

1.2. Nonlinear Combustion Instability 3

1.3. Acoustic Streaming 4

1.4. Present Investigation 6

2. MATHEMATICAL MODEL 10

2.1. Representative Geometry 10

2.2. Assumptions 12

2.3. Equations of Motion 12

2.4. Boundary Conditions 14

2.5. Headwall Injection Flowfield 15

3. INVISCID THEORY 16

3.1. First Order Potential Solution 16

3.2. Second Order Potential Solution 23

4. VISCOUS THEORY 35

4.1. First Order Boundary Layer 35

4.2. Second Order Boundary Layer 44

4.3. Streaming Analysis 53

5. RESULTS AND DISCUSSION 56

5.1. First Order Viscous Solution 56

5.1.1. Wave Characteristics 62

5.1.2. Effect of Turbulence 67

5.2. Second Order Viscous Solution 69

5.3. Acoustic Streaming 75

6. CONCLUSIONS 84

REFERENCES 85

APPENDIX 92

A.1. First Order Potential Flow 93

A.2. Second Order Potential Flow 94

A.3. First Order Boundary Layer Flow 98

A.4. Second Order Boundary Layer Flow 99

VITA 106

List of Figures

Figure 1 Reproduction of the experimental apparatus used by Clayton, Sotter, and Rogerro.[1] 7

Figure 2 Radial dependent pressure trace. 7

Figure 3. Axial pressure distribution data reproduced from Clayton, Sotter and Rogerro.[1] 8

Figure 4. Chamber geometry and coordinate system used in analytical study. 11

Figure 5. The main regions of interest are delineated along with their pertinent equations. 55

Figure 6. Comparison of the radial velocity approximation with numerical solution 57

Figure 7. Numerical verification of first-order tangential velocity approximation 58

Figure 8. First-order approximations for a) radial and b) tangential velocities. The scale on the left-hand-side is for injection Mach numbers of 0.3 and 0.03. The scale on the right-hand-side is for $M_b = 0.003$. 59

Figure 9. The depth of penetration, z_p, versus the Strouhal number,S, for increasing kinetic Reynolds number. 64

Figure 10. The depth of penetration, z_p, versus the penetration number, S_p, for increasing kinetic Reynolds number. 66

Figure 11. Eddy viscosity distribution in typical tactical rocket.[50] 68

Figure 12 Effect of turbulence on axial wave amplitude (Shuttle SRM).[50] 68

Figure 13. Numerical verification of second-order radial velocity 70

Figure 14. Numerical verification of second-order steady tangential velocity..... 71

Figure 15. Steady second-order approximations for a) radial and b) tangential velocities. The scale on the left-hand-side is for injection Mach numbers of 0.3. The scale on the right-hand-side is for M_b = 0.03 and 0.003. 72

Figure 16. First-order traveling wave vector plot at z = 0.01 and three headwall injection Mach numbers of a) M_b = 0.3, b) 0.03, and c) 0.003. 74

Figure 17. Steady second-order boundary layer velocity vector plot at z = 0.01 and three headwall injection Mach numbers of a) M_b = 0.3, b) 0.03, and c) 0.003..... 74

Figure 18. Total vector plot in the outer region illustrating the behavior of a) the purely inviscid potential approximation up to the second order and b-c) the same total potential solution augmented by the streaming contribution. Results are shown for t = 0, n = 1, ε = 0.01, M_b = 0.3 and (a) δ = 0, (b) 0.00647, and (c) 0.0647. 77

Figure 19. Sectors in which oscillatory waves are enhanced or weakened by virtue of streaming. These illustrate the outcome of interactions between a) radial and b) tangential velocities with the streaming motion 77

Figure 20. Comparison of streaming velocities in the limit that $M_b/\delta \to 0$. 79

Figure 21. Velocity magnitude contours for a) second-order potential flow and b) second-order potential flow with streaming contributions. 83

Nomenclature

a_0	mean speed of sound
$\boldsymbol{e}_r, \boldsymbol{e}_\theta, \boldsymbol{e}_z$	unit vectors in r, θ and z directions
f	Hertzian frequency of oscillations, $\omega_0 / (2\pi)$
K	dimensionless frequency, $\omega_0 R / a_0$
k_{mn}	wave number for tangential and radial modes m and n
m	tangential oscillation mode shape number
M_b	headwall injection Mach number, V_b / a_0
$\boldsymbol{n}$	outward pointing unit normal vector
n	radial oscillation mode shape number
p	pressure
r, θ, z	radial, tangential, and axial coordinates
R	chamber radius
Re_k	kinetic Reynolds number, k_{mn} / δ^2
t	time

T temperature

$\boldsymbol{u}$ total velocity vector

$\boldsymbol{U}$ mean flow velocity vector

V mass injection velocity

X rescaled viscous wave number, $X_r + iX_i$

Greek

δ viscous parameter, $[\nu/(a_0 R)]^{1/2}$

ε wave amplitude

γ ratio of specific heats

ν kinematic viscosity, μ/ρ

ρ density

ω unsteady vorticity magnitude

ω_0 dimensional frequency of oscillations, $2\pi f$

Ω mean vorticity magnitude

ζ boundary layer coordinate, $\zeta = z/\delta$

Subscripts

0	mean flow property
b	injection surface
m	mode number
t	partial derivative with respect to time

Superscripts

*	dimensional quantity
r , i	part of a complex variable
'	unsteady flow variable
–	steady flow variable

1. Introduction

1.1. Combustion Instability Overview

The occurrence of high amplitude pressure oscillations has long been a complication plaguing large scale combustors such as liquid rocket engines, solid rocket motors, thrust augmenters and gas turbines.[1-13] The complex interactions between the combustion processes and gas dynamics inside large scale combustors, including liquid rocket engines, have been a major source of uncertainty for design engineers. Many high energy density combustors impulsively display oscillations exhibiting violent fluctuations in pressure, velocities and temperature, instead of the steady or slowly changing combustion properties, at which most are designed to operate. This behavior has been referred to by many descriptors, including combustion instability (CI), oscillatory combustion, unsteady combustion, resonant burning, acoustic instabilities, and others.

While several investigators in the aero-propulsion industry have been active in modeling and diagnosing CI in the United States[2,4,6-9,14-21] and Europe,[22,23] the staggering complexity of issues confronting modelers often leads to unresolved questions. Research, both experimental and theoretical, into the occurrence of combustion instability has been performed in almost every technological application in which it has occurred, thus leading to a rational partition of studies. Combustion instability of liquid rocket engines, which will be the main focus but not limited applicability of this study, is one area of research.

Combustion instability is often experienced in liquid rocket engines. Variations in fuel and oxidizer flow rates, and oscillations in feedline pressures, caused by machinery like turbo-pumps and gas generators, can introduce oscillations into the combustion chamber. The oxidizer and fuel injectors also play a key role in triggering or damping instability. The multitude of variations on injector configurations (impinging, coaxial, shower head, etc.) can be advantageous in the control of droplet atomization, vaporization and combustion, and therefore useful in the muting of flow oscillations. In some respects the constant geometry of the combustion chamber and injectors decreases the complexity of the problem, but the variants described above can, at times, serve to confound the problem.

During the race to the moon in the 1960s, NASA experienced 500 Hz *buzzing* (high frequency oscillations) in the F-1 engine.[24] The structural vibrations involved were of such intensity level that the engines could not be operated for more than a few seconds before the possibility of catastrophic failure. The pressure traces from test runs showed oscillating pressure amplitudes greater than the mean chamber pressure. Engineers, not completely understanding the phenomenon, attached a series of baffles to the injector faceplate. The intention was for the baffles to break-up the transverse acoustic waves. About 1,900 test runs were needed to determine the proper size and arrangement of the baffles to the extent of reducing the oscillating pressure amplitudes to 65% of the mean chamber pressure. The problem was by no means fixed but rendered the engines operational for flight. A complete understanding of the physical mechanism that generates the reduction of flow oscillations through the application of injector baffles has not been

reached. This study provides a stepping stone towards greater knowledge of parallel wave incidence of transverse flow oscillations in a viscous fluid with the hope of obtaining greater understanding of the baffleing mechanism.

1.2. Nonlinear Combustion Instability

Combustion instability in liquid rocket engines is characterized by large amplitude pressure fluctuations, an elevated mean pressure, and frequencies that closely match linear chamber acoustics.[6,7] Owing to the close adherence to linear acoustic frequencies, analytical methodologies put forward to describe flow oscillations lean heavily on the assumption of continually sinusoidal disturbances.[21,25] Contrary to this assumption, however, a vast body of experimental evidence conveys a dissimilar picture, specifically one involving large amplitude oscillations with steep gradients in flow variables. For example, in the extensive experimental work of Clayton, Sotter and co-workers,[1,26-28] a heavily instrumented, laboratory scale, 20,000 lbf thrust engine was used to investigate high amplitude tangential oscillations. Their measurements exhibited sustained, steep-fronted pressure fluctuations with peak-to-peak amplitudes that were an order of magnitude larger than the chamber's operating pressure. The pressure transducers available at the time could not record data rapidly enough to determine if a true discontinuity was present, but the acquired wave forms displayed large amplitude spikes followed by long shallow, low pressure segments. Steep-fronted waves and large amplitude pressure oscillation are indicators that nonlinear fluid mechanics are at play within the engine.

Nonlinear effects in combustion instability are made manifest through two primary

mechanisms, wave steepening and acoustic streaming. The process at which a plane wave steepens has been well understood for much time. At the pressure peak the local speed of sound is elevated, thus increasing the local wave propagation rate. At the outset, the crest of the wave overtakes the depressed pressure portion. The curled-up wave continues to steepen until the solution becomes multi-valued when nonlinear forces act to reverse this trend. This occurrence is well delineated in the final chapter of most acoustics books; it is explained quite elegantly by Pierce.[29] The less discussed nonlinear mechanism, acoustic streaming, will be the focus of the present study. Acoustic streaming, sometimes referred to as secondary flows, is as a steady flow induced by oscillatory motion in a fluid. The underpinning physical mechanisms of acoustic streaming remain unclear. The present study demonstrates how streaming flows induced at a liquid engine's injector face can stimulate a steepened tangential wave form similar to that documented in the Clayton *et al*[1] experiments. In order to model this behavior, tangential and radial waves are superimposed onto a simple mean-flow model. Considerable effort is given to satisfy the no-slip condition at the engine's injector face.

1.3. Acoustic Streaming

Acoustic streaming is a well known, yet unexpected, result of an oscillating fluid's interaction with a solid boundary or another fluid. It has been determined that in the presence of an oscillating medium a steady second order flow will develop. Faraday[30] first observed this phenomenon in connection with vibrating plates. It was identified that air currents on the top of oscillating plates rise and descend at specific locations along the

surface. The locations correlated with areas of the plate's vibrational peaks and nodes. Later in 1866, Kundt's[31] dust tube experiments displayed the existence of a secondary vortical flow that was further elaborated by Schlichting.[32] In the Kundt experiment a standing sound wave was produced in a tube with a small amount of dust particles. The dust particles formed small mounds along the axis of the tube. This is explained by the existence of a secondary flow with a near wall velocity direction toward the nodes of the imposed standing wave. An analytical theory was first applied to the phenomenon by Rayleigh[33] with the theories being further developed by Westervelt,[34] Nyborg,[35] Schlichting[32,36] and others with the main focus being on axial standing waves in various mediums.

Leaning heavily on the approaches put forth by Schlichting, theoretical work performed by Maslen and Moore[11] investigated streaming flows in the context of rocket and jet propulsion. In their 1956 paper, the investigators studied the effects of secondary flows on tangential wave patterns. A circular cylinder with a zero mean flow was utilized to detail the interaction between tangential waves and the chamber's sidewall. Specifically, the secondary flow induced by viscous forces at the sidewall was delineated. Their analysis yielded a streaming profile that acted in the direction opposite to the wave spinning motion. As a result, the investigators determined that steep fronted, shock-like waves could not be produced due to sidewall scattering and viscous dissipation. Later, a study by Flandro[5] that incorporated a mean flow along with mass transpiration from the sidewall predicted a streaming flow in the same direction as the first-order wave. This result was found to be dependent on the magnitude of the injection Mach number. With

extensive work already done involving radial boundary layers,[37-42] it is only natural to investigate wave boundary layer interactions in the axial case as well. The axial acoustic boundary layer situated at the injector face plate will be delineated in this research.

1.4. Present Investigation

The motivation to investigate the axial, headwall boundary layer analog to the Flandro[5] study is prompted by experimental results suggesting that the location of the highest amplitudes and therefore most severe waves can be very close to the injector face.[1,26-28] The experimental work performed by Clayton, Sotter and co-workers,[1,26-28] at the Jet Propulsion Lab provides extensive results that help to guide this analysis. Tangential wave instability was investigated through multiple firings of a highly instrumented 20,000 lbf thrust engine utilizing nitric acid and aniline/furfuryl alcohol propellants and operating at a chamber pressure of 300psia. A schematic of the engine is seen in Fig. 1 with the locations of various pressure sensors being depicted in Figs.2 and 3. Figure 2 presents pressure traces at five distinct locations along the radius of the injector faceplate. The data indicates that the wave amplitude is minimal near the chamber center and increases along the radius reaching a peak amplitude of 2730 psi very near the chamber sidewall. Figure 2 also displays unique wave forms consisting of a large amplitude peak followed by a long shallow trough. This is not the wave form of a shock wave which would be expected from the normal wave steepening process discussed before. More interesting are the pressure traces presented in Fig. 3, where the axial dependence is displayed. Figure 3 shows a 4000 psi peak-to-trough pressure oscillation situated very near the chamber

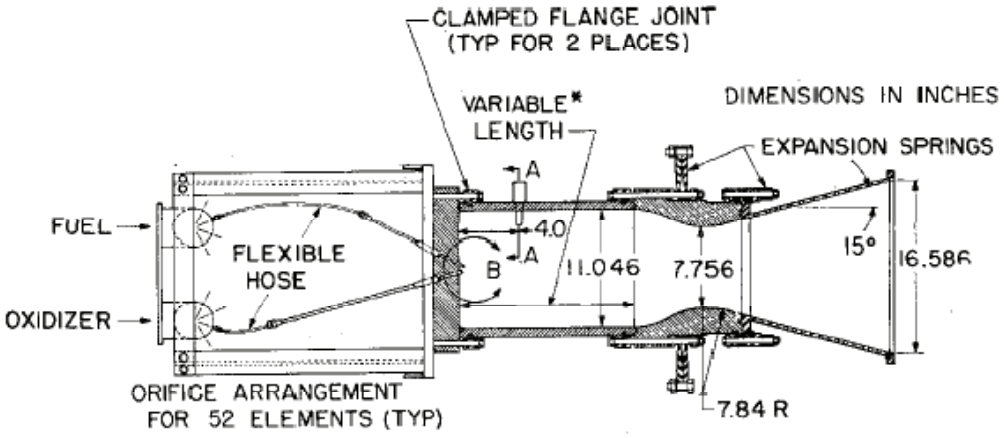


Figure 1 Reproduction of the experimental apparatus used by Clayton, Sotter, and Rogerro.[1]

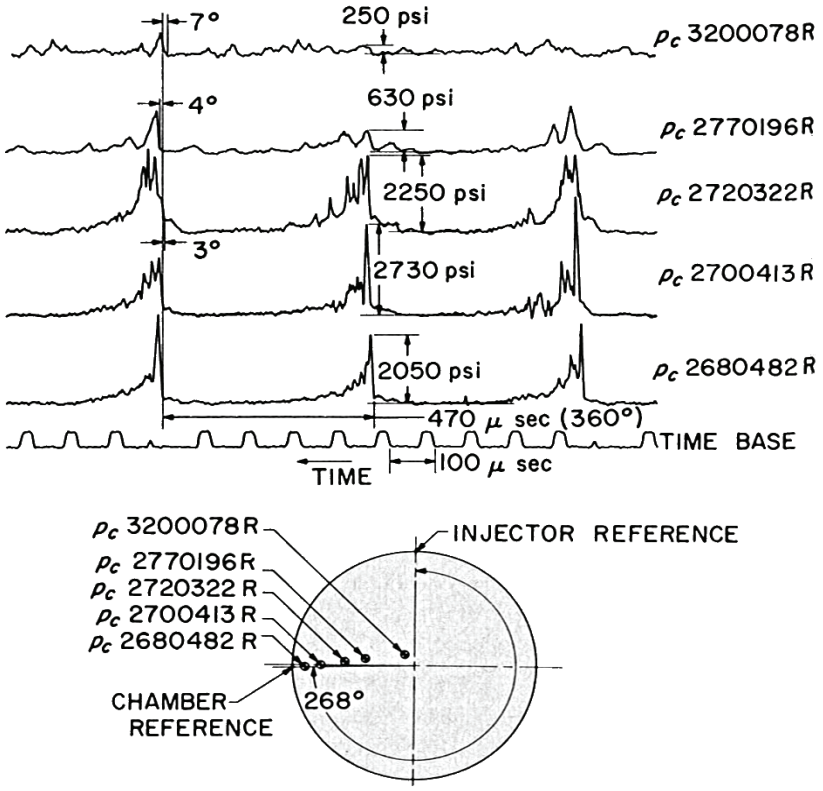


Figure 2 Radial dependent pressure trace reproduced from Clayton *et al.* [1]

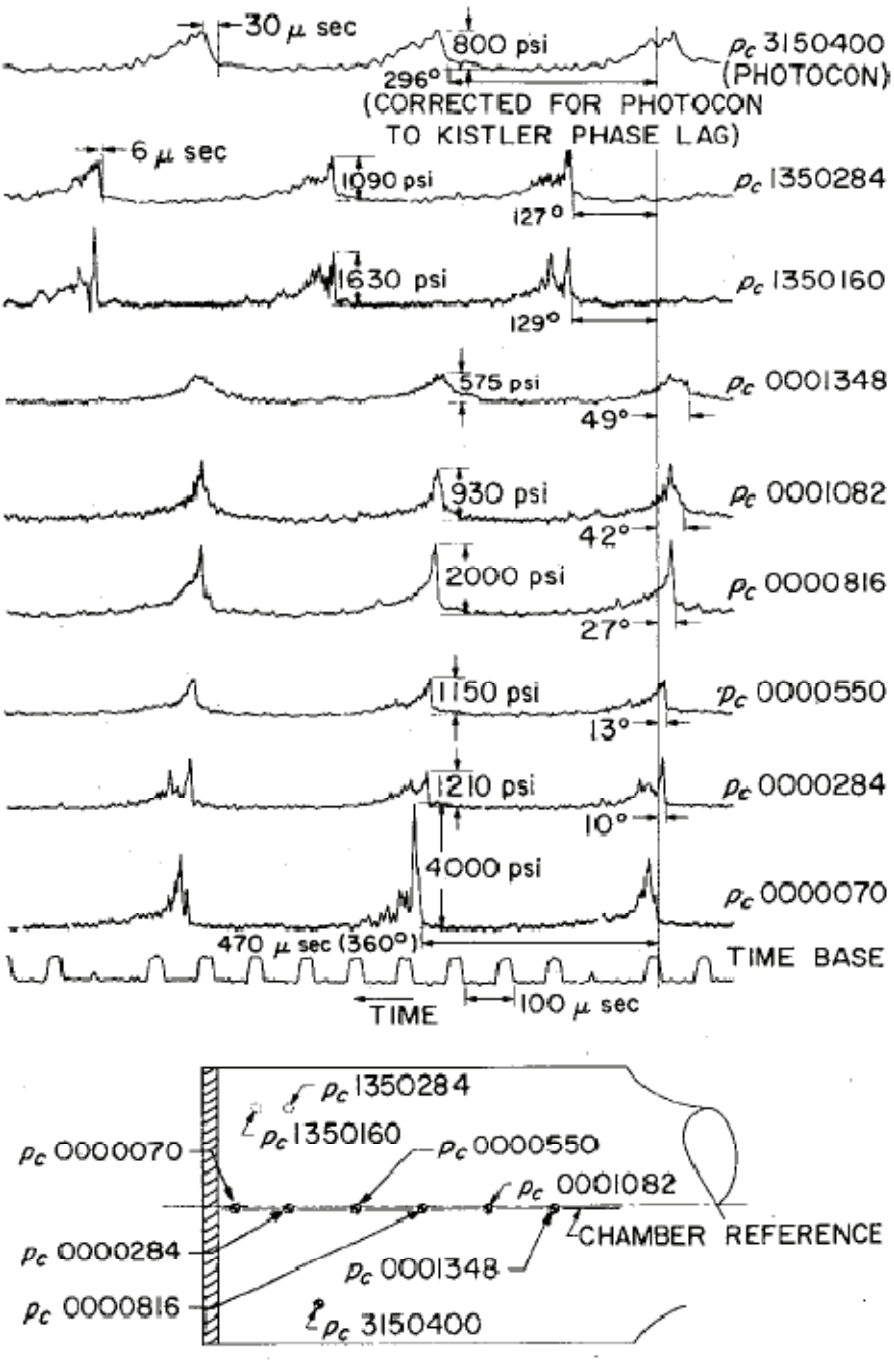


Figure 3. Axial pressure distribution data reproduced from Clayton, Sotter and Rogerro.[1]

headwall. The recorded pressure amplitudes decrease as the sensors move away from the injector face. This indicates that the mechanism creating the large amplitude wave form is rooted at the chamber head end. Since the combustion process in a liquid engine is extremely complex and continuous throughout the chamber, it is assumed that the combustion process itself is not the responsible mechanism. If the combustion process was the mechanism responsible for the amplitude growth then, owing to the fact that combustion is continuous throughout the chamber, one would expect to see a level or even increasing amplitude along the engine axis. A level or increasing trend is not experienced prompting the previously mentioned assumption. This assumption guides the focus of the present investigation to focus on the complex fluid dynamical interaction at the injector faceplate. This study will investigate the steady secondary flow induced by transverse traveling wave incidence with a liquid engine injector faceplate.

2. Mathematical Model

This chapter outlines the basic geometry, assumptions, and governing equations utilized as a basis for the analysis of transverse waves in a liquid rocket engine. The approach used in this study consists of the establishment of a potential flow to which a viscous boundary layer will be appended. Carrying the analysis to the second order allows for the unearthing of acoustic streaming terms that are developed within the viscous layer and sustained into the potential flow. It is these streaming terms that are the focus of this study and are shown to produce alterations in the potential flow wave structure. Such alterations can develop both large peak-to-trough amplitude oscillations with steep pressure gradients and a vortex flow structure that can alter the performance to the extent of damaging the engine.

2.1. Representative Geometry

A semi-infinite cylinder of radius R, displayed in Fig. 4, is utilized to study the streaming flows induced at a liquid engine's injector face. Anchored at the chamber's headwall is the appropriate cylindrical coordinate system with the $z-$coordinate located along the chamber's centerline. In the context of a liquid rocket chamber, it is recognized that the injection process at the headwall or injector faceplate can be extremely complex. However, despite the inherent complexity of the injection patterns, a streamtube motion is quickly established[43]. Bearing these factors in mind, a simple representation of the mean flowfield that consists of a uniform stream with constant velocity, V_b is adopted. It is worth noting that this model can be utilized to model a head-end burning rocket motor.

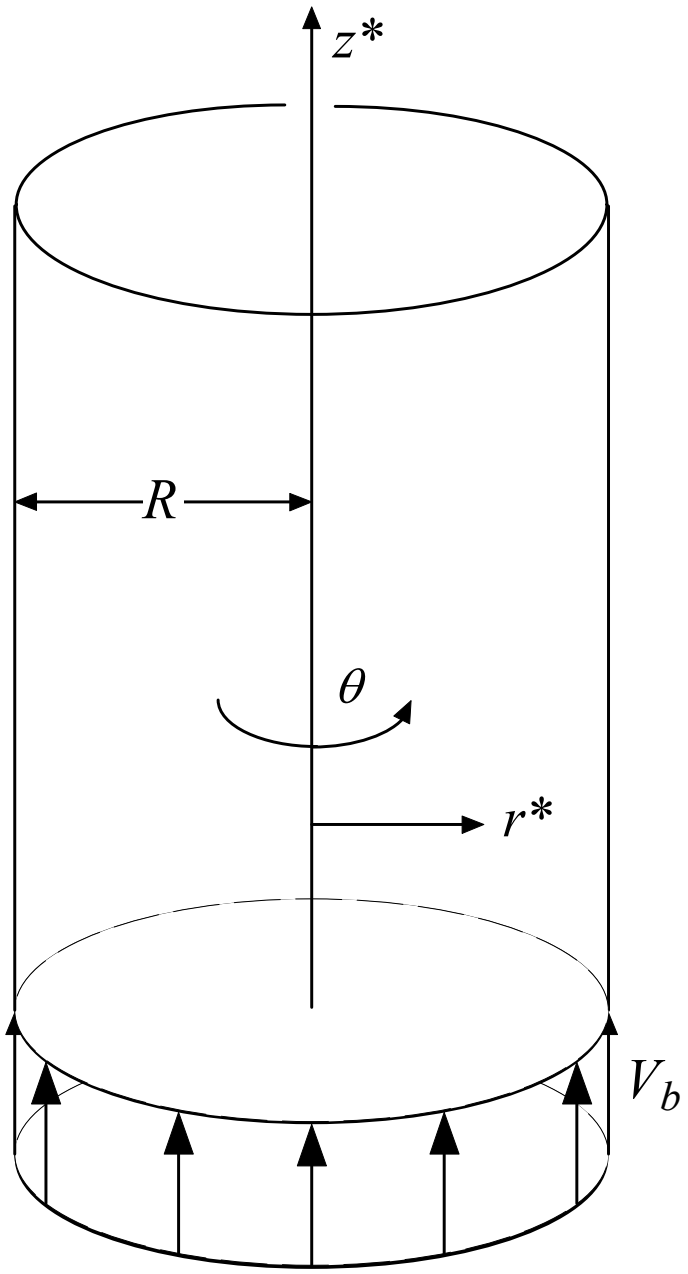


Figure 4. Chamber geometry and coordinate system used in analytical study.

2.2. Assumptions

The fundamental assumptions associated with the use of a perfect gas model are used in this analysis. Namely, it is assumed that the fluid is a continuum displaying Newtonian variations in viscosity. The steady constant velocity liquid injection is assumed to be quickly atomized allowing for the use of compressible flow equations. In the beginning of the analysis an inviscid compressible fluid is assumed with viscosity being introduced in a later section. No attempt is made in this study to model two-phase flow effects or the variation in viscosity accompanying temperature oscillations.

2.3. Equations of Motion

Using the Eulerian reference frame, the dimensionless governing equations for a viscous, compressible gas can be written in a differential vector form as,

Continuity:

$$\frac{\partial \rho}{\partial t} + \nabla \cdot \left(\rho \boldsymbol{u} \right) = 0 \tag{2.1}$$

Momentum:

$$\rho \left(\frac{\partial \boldsymbol{u}}{\partial t} + \frac{1}{2} \nabla \boldsymbol{u}^2 - \boldsymbol{u} \times \boldsymbol{\omega} \right) = -\frac{1}{\gamma} \nabla p - \delta^2 \nabla \times \left(\nabla \times \boldsymbol{u} \right) + \delta_d^2 \nabla \left(\nabla \cdot \boldsymbol{u} \right) + \boldsymbol{F} \tag{2.2}$$

Equation of State:

$$p = \rho T \tag{2.3}$$

The viscous and dilatational parameters that appear in Eq. (2.2) are defined as

$$\delta^2 = \frac{\nu}{a_0 R} \;;\quad \delta_d^2 = \left(\frac{\eta}{\mu} + \frac{4}{3}\right)\delta^2 \tag{2.4}$$

where ν is the kinematic viscosity, μ is the dynamic viscosity and η is the bulk viscosity coefficient. The above equations are written in non-dimensional form through normalizing the variables according to

$$\begin{cases} p = p^*/P_0 \\ \rho = \rho^*/\rho_0 \end{cases} \quad \begin{cases} \boldsymbol{u} = \boldsymbol{u}^*/a_0 \\ t = t^*/\left(R/a_0\right) \end{cases} \quad \begin{cases} r = r^*/R \\ z = z^*/R \end{cases} \quad \begin{cases} T = T^*/T_0 \\ \boldsymbol{\omega} = \boldsymbol{\omega}^*/\left(a_0/R\right) \end{cases} \tag{2.5}$$

The dimensional variables are denoted by an asterisk with the zero subscript referring to mean chamber properties in the absence of wave motion. The cylinder's radius is marked as R and the local speed of sound is a_0.

Starting with a simple perturbation approach the governing equations are first split into a set of steady and unsteady equations. Taking advantage of the initial smallness of the pressure oscillations, the unsteady equations are expanded in terms of amplitude of the unsteady pressure fluctuations, $\varepsilon = p'/P_0$.

$$\begin{aligned} a &= \bar{A} + a' \\ a' &= \varepsilon a^{(1)} + \varepsilon^2 a^{(2)} + \varepsilon^3 a^{(3)} + \ldots \end{aligned} \tag{2.6}$$

Expanding the unsteady governing equations and collecting in powers of ε gives, at the first order:

$$\left\{\begin{aligned}
&\frac{\partial \rho^{(1)}}{\partial t} = -\nabla \cdot \boldsymbol{u}^{(1)} - M_b \nabla \cdot \left[\rho^{(1)} \boldsymbol{U} \right] \\
&\frac{\partial \boldsymbol{u}^{(1)}}{\partial t} = -\frac{\nabla p^{(1)}}{\gamma} - M_b \left[\boldsymbol{u}^{(1)} \cdot \nabla \boldsymbol{U} + \boldsymbol{U} \cdot \nabla \boldsymbol{u}^{(1)} \right] + \boldsymbol{F}^{(1)} + \delta^2 \nabla^2 \boldsymbol{u}^{(1)} \\
&p^{(1)} = T^{(1)} + \rho^{(1)} \\
&\delta \equiv \sqrt{\frac{\nu}{a_0 R}}
\end{aligned}\right\} \tag{2.7}$$

and, at the second order:

$$\left\{\begin{aligned}
&\frac{\partial \rho^{(2)}}{\partial t} = -\nabla \cdot \boldsymbol{u}^{(2)} - \nabla \cdot \left[\rho^{(1)} \boldsymbol{u}^{(1)} \right] - M_b \nabla \cdot \left[\rho^{(2)} \boldsymbol{U} \right] \\
&\frac{\partial \boldsymbol{u}^{(2)}}{\partial t} = -\frac{\nabla p^{(2)}}{\gamma} - M_b \left[\boldsymbol{u}^{(2)} \cdot \nabla \boldsymbol{U} + \boldsymbol{U} \cdot \nabla \boldsymbol{u}^{(2)} + \rho^{(1)} \left(\boldsymbol{u}^{(1)} \cdot \nabla \boldsymbol{U} + \boldsymbol{U} \cdot \nabla \boldsymbol{u}^{(1)} \right) \right] \\
&\qquad\qquad - \rho^{(1)} \frac{\partial \boldsymbol{u}^{(1)}}{\partial t} - \boldsymbol{u}^{(1)} \cdot \nabla \boldsymbol{u}^{(1)} + \boldsymbol{F}^{(2)} + \delta^2 \nabla^2 \boldsymbol{u}^{(2)} \\
&p^{(2)} = T^{(2)} + T^{(1)} \rho^{(1)} + \rho^{(2)}
\end{aligned}\right\} \tag{2.8}$$

2.4. Boundary Conditions

The sidewalls of the combustion chamber are modeled as rigid; the flexing due to pressure fluctuations is negligible. Similarly the chamber headwall is assumed to be rigid. The use of a non-rigid injector plane could be utilized when modeling the coupling between feedline and chamber oscillations. Another advantage to the application of this boundary condition is that the results can easily lend themselves to the case of an endwall burning solid rocket motor. During the initial inviscid study the flow will be allowed to slip at the cylinder's surfaces with the normal components being set to zero. As the effects of viscosity are investigated the flow will be made to satisfy the no-slip condition at the chamber headend and allowed to slip on the sidewall.

2.5. Headwall Injection Flowfield

It may be instructive to note that Eqs. (2.7)–(2.8) represent the interaction equations that prescribe the unsteady wave motion in the simulated liquid rocket engine. Both expressions of conservation of mass and momentum are strongly influenced by the headwall injection Mach number M_b and the mean flowfield function $\boldsymbol{U}$. In the context of a liquid rocket chamber, it is understood that the injection and mixing processes are a multi-faceted and not easily modeled. Yet, the establishment of streamtube motion near the injector face is well accepted. Therefore, a simple uniform steam with constant velocity is used to model the chamber's mean flow. This basic approximation will be necessary to simplify the problem and, in the process, help to elucidate the underpinning physical mechanisms with minimal algebraic encumbrance. Further complexity can of course be pursued at a later time. It should be kept in mind, however, that the uniform flow assumption is accompanied by certain limitations; these will be brought to light later in the analysis. With the near injector faceplate as the principal region of interest, we assume steady injection. Recalling that the non-dimensional mean flow is expressed as $\bar{\boldsymbol{U}} = M_b \boldsymbol{U}$, we take

$$\boldsymbol{U} = (0)\boldsymbol{e}_r + (0)\boldsymbol{e}_\theta + (1)\boldsymbol{e}_z \tag{2.9}$$

This basic representation is illustrated in Fig. 1.

3. Inviscid Theory

Away from the headwall region, viscous effects are confined to a very thin layer along the lateral, non-injecting sidewall. At the outset, a potential inviscid field may be assumed in the downstream region that is sufficiently removed from the injectors. Such a potential flow representation plays the role of an outer solution with respect to the flow adjacent to the headwall. By discounting viscosity, one is left with a set of wave-like equations.

3.1. First Order Potential Solution

A combination of the first order momentum and continuity equations delivers an expression describing the time dependent wave equation to the first order in the wave amplitude, $\mathcal{O}(\varepsilon)$. In the process, body forces and those associated with two-phase flow interactions are dismissed. The isentropic flow assumption is made, whence the pressure and density are related via

$$\rho^{(1)} = \frac{p^{(1)}}{\gamma} \tag{3.1}$$

As usual, constructing the first order wave equation requires taking the time derivative of the continuity equation and subtracting from that the divergence of the momentum equation. One readily obtains a second order hyperbolic partial differential equation defining the fluid flow to the first order in the wave amplitude.

$$\nabla^{(2)} p^{(1)} - p_{tt}^{(1)} = \gamma \left\{ \begin{array}{l} \overline{\rho} \nabla \cdot \boldsymbol{u}_t^{(I)} - \dfrac{\partial}{\partial t} \left[\dfrac{M_b}{\gamma} \nabla \cdot \left(p^{(1)} \boldsymbol{U} \right) + \nabla \cdot \left(\overline{\rho} \boldsymbol{u}^{(I)} \right) \right] \\ + M_b \overline{\rho} \nabla^2 \left(\boldsymbol{U} \cdot \boldsymbol{u}^{(I)} \right) - M_b \overline{\rho} \nabla \cdot \left(\boldsymbol{U} \times \boldsymbol{\omega}^{(1)} + \boldsymbol{u}^{(I)} \times \boldsymbol{\Omega} \right) \end{array} \right\} \tag{3.2}$$

Inserting Eq. (2.9) into Eq. (3.2) gives,

$$\nabla^{(2)} p^{(1)} - p_{tt}^{(1)} = -\frac{\partial}{\partial t} \left[M_b \nabla \cdot \left(p^{(1)} \boldsymbol{U} \right) \right] + \gamma M_b \nabla^2 \left(\boldsymbol{U} \cdot \boldsymbol{u}^{(I)} \right) - \gamma M_b \nabla \cdot \left(\boldsymbol{U} \times \boldsymbol{\omega}^{(1)} \right) \tag{3.3}$$

To represent the oscillatory variables, Euler's notation is used, namely,

$$a' = a e^{-iKt} \tag{3.4}$$

where $K = \omega_0 R / a_0$ is the dimensionless frequency and ω_0 is the actual radian frequency. Equation (3.3) becomes,

$$\nabla^{(2)} p^{(1)} + K^2 p^{(1)} = iK \left(M_b \boldsymbol{U} \cdot \nabla p^{(1)} \right) + \gamma M_b \nabla^2 \left(\boldsymbol{U} \cdot \boldsymbol{u}^{(1)} \right) - \gamma M_b \nabla \cdot \left(\boldsymbol{U} \times \boldsymbol{\omega}^{(1)} \right) \tag{3.5}$$

The boundary conditions for this second order partial differential equation state that the unsteady velocity gradient must vanish at the chamber walls. The corresponding relation for the pressure gradient becomes,

$$\nabla p^{(1)} = \gamma i K \boldsymbol{u}^{(1)} + \gamma M_b \left[\boldsymbol{u}^{(1)} \cdot \nabla \boldsymbol{U} + \boldsymbol{U} \cdot \nabla \boldsymbol{u}^{(1)} \right] \tag{3.6}$$

Looking at Eq. (3.5) it is evident that the injection Mach number M_b may be used as a second perturbation parameter.

$$a' = \varepsilon\left(a^{(1,0)} + M_b a^{(1,1)} + M_b^2 a^{(1,2)} + \ldots\right) + \varepsilon^2\left(a^{(2,0)} + M_b a^{(2,1)} + M_b^2 a^{(2,2)} + \ldots\right) + \ldots \tag{3.7}$$

Expanding the wave equation and collecting terms yields,

$$\begin{aligned} &\nabla^{(2)} p^{(1,0)} + K^2 p^{(1,0)} = 0 \\ &\boldsymbol{n}\cdot\nabla p^{(1,0)}\Big|_{z=0} = 0; \quad \boldsymbol{n}\cdot\nabla p^{(1,0)}\Big|_{r=1} = 0 \end{aligned} \tag{3.8}$$

$$\begin{aligned} &\nabla^{(2)} p^{(1,1)} + K^2 p^{(1,1)} = iK\boldsymbol{U}\cdot\nabla p^{(1,0)} + \gamma\nabla^2\left(\boldsymbol{U}\cdot\boldsymbol{u}^{(1,0)}\right) - \gamma\nabla\cdot\left(\boldsymbol{U}\times\boldsymbol{w}^{(1,0)}\right) \\ &\boldsymbol{n}\cdot\nabla p^{(1,1)}\Big|_{z=0} = 0; \quad \boldsymbol{n}\cdot\nabla p^{(1,1)}\Big|_{r=1} = 0 \end{aligned} \tag{3.9}$$

$$\begin{aligned} &\nabla^{(2)} p^{(1,2)} + K^2 p^{(1,2)} = iK\boldsymbol{U}\cdot\nabla p^{(1,1)} + \gamma\nabla^2\left(\boldsymbol{U}\cdot\boldsymbol{u}^{(1,1)}\right) - \gamma\nabla\cdot\left(\boldsymbol{U}\times\boldsymbol{w}^{(1,1)}\right) \\ &\boldsymbol{n}\cdot\nabla p^{(1,2)}\Big|_{z=0} = 0; \quad \boldsymbol{n}\cdot\nabla p^{(1,2)}\Big|_{r=1} = 0 \end{aligned} \tag{3.10}$$

To solve Eq. (3.8), separation of variables may be used to derive the first-order pressure in the form of $p^{(1,0)} = F(r)G(\theta)H(z)$. At the outset, the wave equation collapses into

$$\frac{\mathrm{d}^2F}{\mathrm{d}r^2}\frac{1}{R} + \frac{1}{r}\frac{\mathrm{d}F}{\mathrm{d}r}\frac{1}{R} + \frac{1}{r^2}\frac{\mathrm{d}^2G}{\mathrm{d}\theta^2}\frac{1}{G} + K^2 = -\frac{\mathrm{d}^2H}{\mathrm{d}z^2}\frac{1}{H} = k_l^2 \tag{3.11}$$

A solution for $H(z)$ is readily found to be that of a longitudinal wave. In the present work, the longitudinal wave number k_l is set to zero in order to isolate the tangential and radial wave contributions. The left-hand-side of Eq. (3.11) is manipulated into

$$r^2\frac{\mathrm{d}^2F}{\mathrm{d}r^2}\frac{1}{F} + r\frac{\mathrm{d}F}{\mathrm{d}r}\frac{1}{F} + r^2K^2 = -\frac{\mathrm{d}^2G}{\mathrm{d}\theta^2}\frac{1}{G} = m^2 \tag{3.12}$$

On one hand, knowing that the $\theta-$dependence cannot be multi-valued, $G(\theta)$ becomes

$$G = A_\theta e^{i m\theta} \tag{3.13}$$

On the other hand, the radial dependence reduces to the standard Bessel equation

$$\frac{\mathrm{d}^2 F}{\mathrm{d}r^2} + \frac{1}{r}\frac{\mathrm{d}F}{\mathrm{d}r} + F\left(k_{mn} - \frac{m^2}{r^2}\right) = 0 \tag{3.14}$$

The solution to this well known equation is

$$F = A_r J_m\left(k_{mn} r\right) + B_r Y\left(k_{mn} r\right) \tag{3.15}$$

The byproduct of tangential and radial contributions is hence

$$p^{(1,0)} = A J_m\left(k_{mn} r\right) e^{i(m\theta)} + B Y\left(k_{mn} r\right) e^{i(m\theta)} \tag{3.16}$$

Equation (3.16) must exhibit a finite pressure at the centerline (i.e., $B = 0$) and a vanishing pressure gradient at the impermeable sidewall, $J'_m\left(k_{mn}\right) = 0$. Using unit normalization for $p^{(1,0)}$, the first order in ε and zeroth order in M_b approximation for the pressure becomes

$$p^{(1,0)} = \mathrm{Re}\left[e^{i(m\theta - Kt)} J_m\left(k_{mn} r\right)\right] = \cos\left(m\theta - Kt\right) J_m\left(k_{mn} r\right);\ \ m = 0,1,2,..;\ \ n = 0,1,2,.. \tag{3.17}$$

where k_{mn} is determined by the roots of the first derivative of the Bessel function of order m, $J'_m\left(k_{mn}\right) = 0$. For example, one finds $k_{01} \simeq 3.83170597 \quad k_{10} \simeq 1.84118378,$

$k_{11} \simeq 5.33144277, \quad k_{02} \simeq 7.01558667, \quad k_{20} \simeq 3.05423693, \text{etc}$. Being chiefly concerned with the effect of tangential wave motion at the headwall, the first spinning mode of interest is k_{10}. Note that Eq. (3.17) captures both tangential and radial oscillation modes. Using Eq. (2.7) and (3.7) produces a set of equations representing the first-order potential velocity

$$\begin{aligned} &\frac{\partial \boldsymbol{u}^{(1,0)}}{\partial t} = -\frac{\nabla p^{(1,0)}}{\gamma} \\ &\boldsymbol{n}\cdot\boldsymbol{u}^{(1,0)}\Big|_{z=0} = 0; \quad \boldsymbol{n}\cdot\boldsymbol{u}^{(1,0)}\Big|_{r=1} = 0 \end{aligned} \tag{3.18}$$

$$\begin{aligned} &\frac{\partial \boldsymbol{u}^{(1,1)}}{\partial t} = -\frac{\nabla p^{(1,1)}}{\gamma} - \left[\boldsymbol{u}^{(1,0)}\cdot\nabla\boldsymbol{U} + \boldsymbol{U}\cdot\nabla\boldsymbol{u}^{(1,0)}\right] \\ &\boldsymbol{n}\cdot\boldsymbol{u}^{(1,1)}\Big|_{z=0} = 0; \quad \boldsymbol{n}\cdot\boldsymbol{u}^{(1,1)}\Big|_{r=1} = 0 \end{aligned} \tag{3.19}$$

and

$$\begin{aligned} &\frac{\partial \boldsymbol{u}^{(1,2)}}{\partial t} = -\frac{\nabla p^{(1,2)}}{\gamma} - \left[\boldsymbol{u}^{(1,1)}\cdot\nabla\boldsymbol{U} + \boldsymbol{U}\cdot\nabla\boldsymbol{u}^{(1,1)}\right] \\ &\boldsymbol{n}\cdot\boldsymbol{u}^{(1,2)}\Big|_{z=0} = 0; \quad \boldsymbol{n}\cdot\boldsymbol{u}^{(1,2)}\Big|_{r=1} = 0 \end{aligned} \tag{3.20}$$

using Eqs. (3.17)-(3.18) gives,

$$\boldsymbol{u}^{(1,0)} = \mathrm{Re}\begin{bmatrix} -i\frac{1}{\gamma K}e^{i(m\theta - Kt)}J_m'\left(k_{mn}r\right)\boldsymbol{e}_r \\ +\frac{1}{\gamma K}\left(\frac{m}{r}\right)e^{i(m\theta - Kt)}J_m\left(k_{mn}r\right)\boldsymbol{e}_\theta \\ +0\boldsymbol{e}_z \end{bmatrix} \tag{3.21}$$

which can be written in terms of trigonometric values as,

$$\boldsymbol{u}^{(1,0)} = \begin{bmatrix} \frac{1}{\gamma K}\sin\left(m\theta - Kt\right) J_m'\left(k_{mn} r\right)\boldsymbol{e_r} \\ +\frac{1}{\gamma K}\left(\frac{m}{r}\right)\cos\left(m\theta - Kt\right) J_m\left(k_{mn} r\right)\boldsymbol{e}_\theta \\ +0\boldsymbol{e}_z \end{bmatrix} \tag{3.22}$$

Carrying the solution to higher orders in the injection Mach number requires focusing on Eq. (3.9) and utilizing the zeroth order flow profile. Noting that the zeroth order (in the Mach number) velocity is irrotational and does not possess a $z-$coordinate component, some simplification to the right-hand-side of Eq. (3.9) can be made, namely

$$\begin{aligned} &\nabla^{(2)} p^{(1,1)} + K^2 p^{(1,1)} = iK \cancel{\boldsymbol{U}\cdot\nabla p^{(1,0)}} + \gamma\nabla^2\cancel{\left(\boldsymbol{U}\cdot\boldsymbol{u}^{(1,0)}\right)} - \gamma\nabla\cdot\left(\boldsymbol{U}\times\cancel{\boldsymbol{\omega}^{(1,0)}}\right) \\ &\boldsymbol{n}\cdot\nabla p^{(1,1)}\Big|_{z=0} = 0; \quad \boldsymbol{n}\cdot\nabla p^{(1,1)}\Big|_{r=1} = 0 \end{aligned} \tag{3.23}$$

It is apparent that the above equation representing the $\mathcal{O}(1,1)$ is similar in form to Eq. (3.8) making the solution easily attainable.

$$p^{(1,1)} = \mathrm{Re}\left[e^{i(m\theta - Kt)} J_m\left(k_{mn} r\right)\right] = \cos\left(m\theta - Kt\right) J_m\left(k_{mn} r\right); \quad m = 0,1,2,..; \quad n = 0,1,2,.. \tag{3.24}$$

The equation governing the first order velocity profile is easily derived and simplified noting that the mean flow is constant and that the zeroth order velocity is free of a component in the *z* direction.

$$\frac{\partial \boldsymbol{u}^{(1,1)}}{\partial t} = -\frac{\nabla p^{(1,1)}}{\gamma} - M_b\left[\boldsymbol{u}^{(1,0)}\cdot\cancel{\nabla\boldsymbol{U}} + \cancel{\boldsymbol{U}\cdot\nabla\boldsymbol{u}^{(1,0)}}\right] \tag{3.25}$$

leaving,

$$iK\boldsymbol{u}^{(1,1)} = \frac{\nabla p^{(1,1)}}{\gamma} \tag{3.26}$$

and so,

$$\boldsymbol{u}^{(1,1)} = \mathrm{Re}\begin{bmatrix} -i\frac{1}{\gamma K}e^{i(m\theta - Kt)}J'_m\left(k_{mn}r\right)\boldsymbol{e_r} \\ +\frac{1}{\gamma K}\left(\frac{m}{r}\right)e^{i(m\theta - Kt)}J_m\left(k_{mn}r\right)\boldsymbol{e}_\theta \\ +0\boldsymbol{e}_z \end{bmatrix} \tag{3.27}$$

It may be easily deduced that high order corrections are will follow the same pattern. This is a direct result of the assumptions made about the mean flow profile and focusing on only radial and tangential wave motion. By carrying the solution to higher orders in the injection Mach number, the same recursive formulation is obtained at every order. By summing all terms, one deduces

$$\begin{cases} \boldsymbol{u}^{(1)} = \left(\sum_{j=0}^{\infty} M_b^j\right)\boldsymbol{u}^{(1,0)} = \dfrac{1}{1-M_b}\boldsymbol{u}^{(1,0)} \\ p^{(1)} = \left(\sum_{j=0}^{\infty} M_b^j\right)p^{(1,0)} = \dfrac{1}{1-M_b}p^{(1,0)} = \dfrac{J_m\left(k_{mn}r\right)}{1-M_b}\cos\left(m\theta - Kt\right) \end{cases} \tag{3.28}$$

Note that the infinite series are reducible by use of the identity

$$\sum_{j=0}^{\infty} x^j = \frac{1}{1-x} \tag{3.29}$$

By summing over an infinite series in the Mach number, the solution is captured exactly in M_b, specifically with a truncation error equal to

$$\lim_{j\to\infty} M_b^j = 0. \tag{3.30}$$

Therefore, for the remainder of the analysis, the highly accurate solution will be marked through the use of $\boldsymbol{u}^{(1)}$ and $p^{(1)}$.

3.2. Second Order Potential Solution

In order to extend the analysis to second order we must start with a second order wave equation. Utilizing Eq. (2.8) in the same manner as before a higher order corollary to Eq. (3.3) is obtained. The isentropic assumption is still used at this level,

$$\rho^{(2)} = \frac{p^{(2)}}{\gamma} - \frac{\gamma-1}{2\gamma^2}\left[p^{(1)}\right]^2 \tag{3.31}$$

The combination of continuity and momentum leads to the second order wave equation,

$$\begin{aligned}\nabla^2 p^{(2)} - p_{tt}^{(2)} = {} & \frac{1-\gamma}{2\gamma}\left\{\left[p^{(1)}\right]^2\right\}_{tt} + \nabla\cdot p^{(1)}\boldsymbol{u}^{(1)} - \gamma\nabla\cdot\left[\boldsymbol{u}^{(1)}\cdot\nabla\boldsymbol{u}^{(1)}\right] + M_b\left[\nabla\cdot p^{(2)}\boldsymbol{U}\right]_t \\ & + M_b\left(\frac{1-\gamma}{\gamma}\nabla\cdot\left[p^{(1)^2}\boldsymbol{U}\right]_t - \gamma\nabla\cdot\left\{\boldsymbol{u}^{(2)}\cdot\nabla\boldsymbol{U} + \boldsymbol{U}\cdot\nabla\boldsymbol{u}^{(2)} + \frac{p^{(1)}}{\gamma}\left[\boldsymbol{u}^{(1)}\cdot\nabla\boldsymbol{U} + \boldsymbol{U}\cdot\nabla\boldsymbol{u}^{(1)}\right]\right\}\right)\end{aligned} \tag{3.32}$$

Simplifications can be made using the assumed mean flowfield,

$$\begin{aligned}\nabla^2 p^{(2)} - p_{tt}^{(2)} = {} & \frac{1-\gamma}{2\gamma}\left\{\left[p^{(1)}\right]^2\right\}_{tt} + \nabla\cdot p_t^{(1)}\boldsymbol{u}^{(1)} - \gamma\frac{\nabla^2}{2}\left[\boldsymbol{u}^{(1)}\cdot\boldsymbol{u}^{(1)}\right] \\ & + M_b\left[\nabla\cdot p^{(2)}\boldsymbol{U}\right]_t - M_b\gamma\nabla\cdot\left\{\nabla\left[\boldsymbol{U}\cdot\boldsymbol{u}^{(2)}\right] - \boldsymbol{U}\times\boldsymbol{\omega}^{(2)}\right\}\end{aligned} \tag{3.33}$$

Parallel expansion in the Mach number can be performed using

$$p^{(2)} = p^{(2,0)} + M_b p^{(2,1)} + M_b^2 p^{(2,2)} + \ldots \tag{3.34}$$

This enables the extraction, at leading order in the Mach number and second order in the wave amplitude,

$$\begin{aligned} &\nabla^2 p^{(2,0)} - p_{tt}{}^{(2,0)} = \frac{1-\gamma}{2\gamma}\left\{\left[\, p^{(1,0)} \,\right]^2\right\}_{tt} + \nabla \cdot p_t^{(1,0)} \boldsymbol{u}^{(1,0)} - \gamma \frac{\nabla^2}{2}\left[\, \boldsymbol{u}^{(1,0)} \cdot \boldsymbol{u}^{(1,0)} \,\right] \\ &\boldsymbol{n} \cdot \nabla p^{(2,0)}\Big|_{z=0} = 0; \quad \boldsymbol{n} \cdot \nabla p^{(2,0)}\Big|_{r=1} = 0 \end{aligned} \tag{3.35}$$

$$\begin{aligned} &\nabla^2 p^{(2,1)} - p_{tt}{}^{(2,1)} = \frac{1-\gamma}{\gamma}\left[\, p^{(1,0)} p^{(1,1)} \,\right]_{tt} + \nabla \cdot \left[\, p_t^{(1,1)} \boldsymbol{u}^{(1,0)} + p_t^{(1,0)} \boldsymbol{u}^{(1,1)} \,\right] \\ &\qquad - \gamma \nabla^2 \left[\, \boldsymbol{u}^{(1,0)} \cdot \boldsymbol{u}^{(1,1)} \,\right] + \left[\, \nabla \cdot p^{(2,0)} U \,\right]_t - \gamma \nabla \cdot \left\{ \nabla \left[\, \boldsymbol{U} \cdot \boldsymbol{u}^{(2,0)} \,\right] - \boldsymbol{U} \times \boldsymbol{\omega}^{(2,0)} \right\} \\ &\boldsymbol{n} \cdot \nabla p^{(2,1)}\Big|_{z=0} = 0; \quad \boldsymbol{n} \cdot \nabla p^{(2,1)}\Big|_{r=1} = 0 \end{aligned} \tag{3.36}$$

and,

$$\begin{aligned} \nabla^2 p^{(2,2)} - p_{tt}{}^{(2,2)} &= \frac{1-\gamma}{2\gamma}\left\{ 2 p^{(1,0)} p^{(1,2)} + \left[\, p^{(1,1)} \,\right]^2 \right\}_{tt} \\ &\quad + \nabla \cdot \left[\, p_t^{(1,1)} \boldsymbol{u}^{(1,1)} + p_t^{(1,2)} \boldsymbol{u}^{(1,0)} + p_t^{(1,0)} \boldsymbol{u}^{(1,2)} \,\right] + \left[\, \nabla \cdot p^{(2,1)} U \,\right]_t \\ &\quad - \gamma \frac{\nabla^2}{2}\left[\, 2\boldsymbol{u}^{(1,0)} \cdot \boldsymbol{u}^{(1,2)} + \boldsymbol{u}^{(1,1)} \cdot \boldsymbol{u}^{(1,1)} \,\right] - \gamma \nabla \cdot \left\{ \nabla \left[\, \boldsymbol{U} \cdot \boldsymbol{u}^{(2,1)} \,\right] - \boldsymbol{U} \times \boldsymbol{\omega}^{(2,1)} \right\} \\ \boldsymbol{n} \cdot \nabla p^{(2,2)}\Big|_{z=0} &= 0; \quad \boldsymbol{n} \cdot \nabla p^{(2,2)}\Big|_{r=1} = 0 \end{aligned} \tag{3.37}$$

The first order flowfield is used to evaluate the right-hand-side of Eq. (3.35). This produces

$$\nabla^2 p^{(2,0)} - p_{tt}{}^{(2,0)} = F(r) + B(r)\cos 2(m\theta - Kt) \tag{3.38}$$

where

$$F(r)=\frac{1}{2\gamma K^2}\left\{\begin{array}{l}\left(\frac{3m^2}{r^3}+\frac{K^2}{r}\right)J_m(k_{mn}r)J'_m(k_{mn}r)+\left(K^2-\frac{m^2}{r^2}\right)J'^2_m(k_{mn}r)\\+\left(K^2-\frac{m^2}{r^2}\right)J_m(k_{mn}r)J''_m(k_{mn}r)-\frac{1}{r}J'_m(k_{mn}r)J''_m(k_{mn}r)\\-J''^2_m(k_{mn}r)-J'_m(k_{mn}r)J'''_m(k_{mn}r)-\frac{2m^2}{r^4}J^2_m(k_{mn}r)\end{array}\right\} \tag{3.39}$$

and

$$B(r)=\frac{1}{2\gamma K^2}\left\{\begin{array}{l}\left[2K^4(\gamma-1)-\frac{2(m^2-m^4)}{r^4}+\frac{2K^2m^2}{r^2}\right]J^2_m(k_{mn}r)+J'_m(k_{mn}r)J'''_m(k_{mn}r)\\+\left(\frac{3m^2}{r^3}-\frac{K^2}{r}\right)J_m(k_{mn}r)J'_m(k_{mn}r)-\left(K^2+\frac{3m^2}{r^2}\right)J'^2_m(k_{mn}r)\\-\left(K^2+\frac{m^2}{r^2}\right)J_m(k_{mn}r)J''_m(k_{mn}r)+\frac{J'_m(k_{mn}r)J''_m(k_{mn}r)}{r}+J''^2_m(k_{mn}r)\end{array}\right\} \tag{3.40}$$

From the right–hand–side of Eq. (3.38) it is apparent that the second order pressure will be made up of steady and unsteady parts. These separate parts will be identified as the steady and oscillating parts,

$$p^{(2,0)}=p^{(2,0)}_{st}+p^{(2,0)}_{os} \tag{3.41}$$

The particular solution to Eq. (3.38) is,

$$p^{(2,0)}_p=H(r)+G(r)\cos 2(m\theta-Kt) \tag{3.42}$$

$$H(r)=-\tfrac{1}{4\gamma K^2}\left\{\left[\left(\tfrac{m}{r}\right)^2-K^2\right]J_m(k_{mn}r)^2+J'_m(k_{mn}r)^2\right\} \tag{3.43}$$

$$G(r)=\tfrac{1}{2\gamma K^2}\left\{-\left[\tfrac{1}{2}\left(\tfrac{m}{r}\right)^2+\tfrac{3}{2}K^2\right]J_m\left(k_{mn}r\right)^2+\tfrac{1}{2}J'_m\left(k_{mn}r\right)^2+2K^4\left(\gamma-1\right)f\left(r\right)\right\}$$
$$s/t \;\mapsto\; f''+\tfrac{1}{r}f'+4\left(K^2-\tfrac{m^2}{r^2}\right)f=J_m\left(k_{mn}r\right)^2 \tag{3.44}$$

with the homogenous solution being of the form of the first order solution,

$$p_H^{(2,0)}=\cos\left(m\theta-Kt\right)J_m\left(k_{mn}r\right) \tag{3.45}$$

Then, since

$$J''_m\left(k_{mn}r\right)+\frac{J'_m\left(k_{mn}r\right)}{r}+\left[K^2-\left(\frac{m}{r}\right)^2\right]J_m=0 \tag{3.46}$$

one has

$$-\left[K^2-\left(\frac{m}{r}\right)^2\right]J_m^2\left(k_{mn}r\right)=-\left[J_m\left(k_{mn}r\right)J''_m\left(k_{mn}r\right)+\tfrac{1}{r}J_m\left(k_{mn}r\right)J'_m\left(k_{mn}r\right)\right] \tag{3.47}$$

and so Eq. (3.43) can be written as;

$$H(r)=-\tfrac{1}{4\gamma K^2}\left\{J_m\left(k_{mn}r\right)J''_m\left(k_{mn}r\right)+\tfrac{1}{r}J_m\left(k_{mn}r\right)J'_m\left(k_{mn}r\right)+J'_m\left(k_{mn}r\right)^2\right\} \tag{3.48}$$

one collects

$$p^{(2,0)}=\tfrac{1}{4\gamma K^2}\left\{-\left[\left(\tfrac{m}{r}\right)^2+K^2\right]J_m\left(k_{mn}r\right)^2+J'_m\left(k_{mn}r\right)^2+4K^4\left(\gamma-1\right)f\left(r\right)\right\}\cos 2\left(m\theta-Kt\right)$$
$$-\tfrac{1}{4\gamma K^2}\left\{J_m\left(k_{mn}r\right)J''_m\left(k_{mn}r\right)+\tfrac{1}{r}J_m\left(k_{mn}r\right)J'_m\left(k_{mn}r\right)+J'_m\left(k_{mn}r\right)^2\right\}+\cos\left(m\theta-Kt\right)J_m\left(k_{mn}r\right) \tag{3.49}$$

With the focus of this study resting with the steady "streaming" terms, only the time-independent part of the second order solution is retained; giving,

$$p_{st}^{(2,0)} = -\frac{1}{4\gamma K^2}\left\{ J_m\left(k_{mn}r\right) J_m''\left(k_{mn}r\right) + \frac{1}{r} J_m\left(k_{mn}r\right) J_m'\left(k_{mn}r\right) + J_m'\left(k_{mn}r\right)^2 \right\} \tag{3.50}$$

Now that a second order pressure distribution has been established it is prudent to evaluate the second order velocity profile. Equations (2.8) and (3.1) give an expression for the momentum equation at second order,

$$\frac{\partial \boldsymbol{u}^{(2)}}{\partial t} = -\frac{\nabla p^{(2)}}{\gamma} - \frac{p^{(1)}}{\gamma}\frac{\partial \boldsymbol{u}^{(1)}}{\partial t} - \boldsymbol{u}^{(1)} \cdot \nabla \boldsymbol{u}^{(1)} - M_b \left[\begin{array}{l} \boldsymbol{u}^{(2)} \cdot \nabla \boldsymbol{U} + \boldsymbol{U} \cdot \nabla \boldsymbol{u}^{(2)} \\ + \dfrac{p^{(1)}}{\gamma}\left(\boldsymbol{u}^{(1)} \cdot \nabla \boldsymbol{U} + \boldsymbol{U} \cdot \nabla \boldsymbol{u}^{(1)} \right) \end{array} \right] \tag{3.51}$$

It is natural to expand the second order momentum equation in terms of the injection Mach number, as was done by Eq. (3.7). Before this is done a closer examination of Eq. (3.51) reveals some advantageous simplifications. The projection of the assumed mean flow onto the first–order unsteady velocity is zero. It is also known that both the mean and unsteady vorticity are zero, making the second term of the order of the injection mach number on the right–hand–side of Eq. (3.51) vanish. At the outset, one has

$$\frac{\partial \boldsymbol{u}^{(2)}}{\partial t} = -\frac{\nabla p^{(2)}}{\gamma} - \frac{p^{(1)}}{\gamma}\frac{\partial \boldsymbol{u}^{(1)}}{\partial t} - \boldsymbol{u}^{(1)} \cdot \nabla \boldsymbol{u}^{(1)} - M_b \left[\begin{array}{l} \boldsymbol{u}^{(2)} \cdot \cancel{\nabla \boldsymbol{U}} + \boldsymbol{U} \cdot \nabla \boldsymbol{u}^{(2)} \\ + \dfrac{p^{(1)}}{\gamma}\left(\boldsymbol{u}^{(1)} \cdot \cancel{\nabla \boldsymbol{U}} + \cancel{\boldsymbol{U} \cdot \nabla \boldsymbol{u}^{(1)}} \right) \end{array} \right] \tag{3.52}$$

Expanding Eq. (3.52) and collecting terms delivers a group of equations governing the second order potential velocity field and its boundary conditions.

$$\begin{aligned}
&\boldsymbol{u}_t^{(2,0)} = -\frac{\nabla p^{(2,0)}}{\gamma} - \frac{p^{(1,0)}}{\gamma}\frac{\partial \boldsymbol{u}^{(1,0)}}{\partial t} - \boldsymbol{u}^{(1,0)} \cdot \nabla \boldsymbol{u}^{(1,0)} \\
&\boldsymbol{n} \cdot \boldsymbol{u}^{(2,0)}\Big|_{r=1} = 0; \qquad \boldsymbol{n} \cdot \boldsymbol{u}^{(2,0)}\Big|_{z=0} = 0
\end{aligned} \tag{3.53}$$

$$\begin{aligned}
\frac{\partial \boldsymbol{u}^{(2,1)}}{\partial t} = &-\frac{\nabla p^{(2,1)}}{\gamma} - \frac{p^{(1,1)}}{\gamma}\frac{\partial \boldsymbol{u}^{(1,0)}}{\partial t} - \frac{p^{(1,0)}}{\gamma}\frac{\partial \boldsymbol{u}^{(1,1)}}{\partial t} - \boldsymbol{u}^{(1,1)} \cdot \nabla \boldsymbol{u}^{(1,0)} \\
&- \boldsymbol{u}^{(1,0)} \cdot \nabla \boldsymbol{u}^{(1,1)} - \left[\boldsymbol{u}^{(2,0)} \cdot \nabla \boldsymbol{U} + \boldsymbol{U} \cdot \nabla \boldsymbol{u}^{(2,0)} \right] \\
&\boldsymbol{n} \cdot \boldsymbol{u}^{(2,1)}\Big|_{r=1} = 0; \qquad \boldsymbol{n} \cdot \boldsymbol{u}^{(2,1)}\Big|_{z=0} = 0
\end{aligned} \tag{3.54}$$

and

$$\begin{aligned}
\frac{\partial \boldsymbol{u}^{(2,2)}}{\partial t} = &-\frac{\nabla p^{(2,2)}}{\gamma} - \frac{p^{(1,0)}}{\gamma}\frac{\partial \boldsymbol{u}^{(1,2)}}{\partial t} - \frac{p^{(1,1)}}{\gamma}\frac{\partial \boldsymbol{u}^{(1,1)}}{\partial t} - \frac{p^{(1,2)}}{\gamma}\frac{\partial \boldsymbol{u}^{(1,0)}}{\partial t} \\
&- \boldsymbol{u}^{(1,0)} \cdot \nabla \boldsymbol{u}^{(1,2)} - \boldsymbol{u}^{(1,1)} \cdot \nabla \boldsymbol{u}^{(1,1)} - \boldsymbol{u}^{(1,2)} \cdot \nabla \boldsymbol{u}^{(1,0)} - \boldsymbol{u}^{(2,1)} \cdot \nabla \boldsymbol{U} + \boldsymbol{U} \cdot \nabla \boldsymbol{u}^{(2,1)} \\
&+ \frac{p^{(1,0)}}{\gamma}\left(\boldsymbol{u}^{(1,1)} \cdot \nabla \boldsymbol{U} + \boldsymbol{U} \cdot \nabla \boldsymbol{u}^{(1,1)} \right) + \frac{p^{(1,1)}}{\gamma}\left(\boldsymbol{u}^{(1,0)} \cdot \nabla \boldsymbol{U} + \boldsymbol{U} \cdot \nabla \boldsymbol{u}^{(1,0)} \right) \\
&\boldsymbol{n} \cdot \boldsymbol{u}^{(2,2)}\Big|_{r=1} = 0; \qquad \boldsymbol{n} \cdot \boldsymbol{u}^{(2,2)}\Big|_{z=0} = 0
\end{aligned} \tag{3.55}$$

Utilizing the first order flowfield and second order pressure solution gives a right–hand–side to Eq. (3.53) that can be solved through normal techniques. The radial velocity being,

$$\begin{aligned}
&\left[u_r^{(2,0)} \right]_t = \tfrac{1}{4K^2\gamma^2}\Big\{ \left[8K^2 J_m\left(k_{mn}\right) J'_m\left(k_{mn}r\right) + 4K^2\left(1-\gamma\right)K^2 f'\left(r\right) \right] \cos 2\left(m\theta - Kt\right) \\
&-4K^2 \cos\left(m\theta - Kt\right) J'_m\left(k_{mn}r\right) + \frac{J_m\left(k_{mn}\right)}{r}\begin{bmatrix} 2\tfrac{m^2}{r^2} J_m\left(k_{mn}r\right) - \left(\tfrac{1}{r} + 2\tfrac{m^2}{r} - 2rK^2\right) J'_m\left(k_{mn}r\right) \\ + J_m^{-1}\left(k_{mn}\right) J'^{\,2}_m\left(k_{mn}r\right) + J''_m\left(k_{mn}r\right) + J'''_m\left(k_{mn}r\right) \end{bmatrix} \Big\}
\end{aligned} \tag{3.56}$$

From the derivation of the first order pressure solution we recall that,

$$J_m''\left(k_{mn}\right)+\tfrac{1}{r}J_m'\left(k_{mn}\right)+\left(K^2-\tfrac{m^2}{r^2}\right)J_m\left(k_{mn}\right)=0 \tag{3.57}$$

With this in mind it is noted that the last grouping of terms on the right–hand–side of Eq. (3.56) is equivalent to zero, hence

$$\begin{aligned}\frac{d}{dr}J_m\left(k_{mn}r\right)\left[J_m''\left(k_{mn}\right)+\tfrac{1}{r}J_m'\left(k_{mn}\right)+\left(K^2-\tfrac{m^2}{r^2}\right)J_m\left(k_{mn}\right)\right]=\\ \left[\begin{array}{l}2\tfrac{m^2}{r^3}J_m^2\left(k_{mn}r\right)-\left(\tfrac{1}{r^2}+2\tfrac{m^2}{r^2}-2K^2\right)J_m\left(k_{mn}\right)J_m'\left(k_{mn}r\right)\\ +\tfrac{1}{r}\left(J_m'^{\,2}\left(k_{mn}r\right)+J_m\left(k_{mn}\right)J_m''\left(k_{mn}r\right)+J_m\left(k_{mn}\right)J_m'''\left(k_{mn}r\right)\right)\end{array}\right]\end{aligned} \tag{3.58}$$

giving,

$$\begin{aligned}u_r^{(2,0)}=&-\tfrac{1}{2\gamma^2K}\left[2J_m\left(k_{mn}\right)J_m'\left(k_{mn}r\right)+\left(1-\gamma\right)K^2f'\left(r\right)\right]\sin 2\left(m\theta-Kt\right)\\ &+\tfrac{1}{\gamma K}\sin\left(m\theta-Kt\right)J_m'\left(k_{mn}r\right)\end{aligned} \tag{3.59}$$

Turning focus to the θ-direction, the same process is applied providing an azimuthal component of the form,

$$u_\theta^{(2,0)}=\tfrac{1}{\gamma K}\left(\tfrac{m}{r}\right)\left\{J_m\left(k_{mn}r\right)\cos\left(m\theta-Kt\right)-\tfrac{1}{\gamma}\left[J_m^2\left(k_{mn}r\right)+K^2\left(1-\gamma\right)f\left(r\right)\right]\cos 2\left(m\theta-Kt\right)\right\} \tag{3.60}$$

It is prudent to note that the constants of integration have been left out of the above formulation. Given an initial condition, the constants could easily be replaced, but are deemed inconsequential since they will only include a short transient addition to the oscillatory solution. Equations (3.59) and (3.60) represent a second order flowfield that is devoid of steady velocity terms, this is similar to results given by Maslen and Moore.[11] The lack of a time independent flowfield is not a surprise since it is well understood that

streaming flows originate in the viscous boundary layer. But, these results do demonstrate a departure from the approach used in classic streaming analysis.[32,34-36] In previous studies on secondary flows induced by oscillatory motion the authors do not extend the potential solution to the second order, this limitation makes it necessary to impose additional assumptions or to neglect the second order pressure gradient during the derivation of the viscous flow model. It was shown by Flandro[5] that these type of assumptions can lead to steady terms in the second order potential flow that may be deemed erroneous.

It is now possible to use these finding to derive the right–hand–side of the wave equation to the second order in epsilon and first order in M_b from Eq. (3.36):

$$\nabla^2 p^{(2,1)} - p_{tt}^{(2,1)} = 2F(r) + 2B(r)\cos 2(m\theta - Kt) \tag{3.61}$$

where $F(r)$ and $B(r)$ are defined in Eqs. (3.39) and (3.40). The solution to this second order wave equation is found through an application of separation of variables and undetermined coefficients. After some algebra, one gets

$$\begin{aligned} p^{(2,1)} = \tfrac{-1}{2\gamma K^2}\Bigg(&\Big\{\Big[\left(\tfrac{m}{r}\right)^2 + K^2\Big] J_m(k_{mn}r)^2 - J'_m(k_{mn}r)^2 - 4K^4(\gamma-1) f(r)\Big\}\cos\big[2(m\theta - Kt)\big] \\ &-\Big\{J_m(k_{mn}r) J''_m(k_{mn}r) + \tfrac{1}{r} J_m(k_{mn}r) J'_m(k_{mn}r) + J'_m(k_{mn}r)^2\Big\}\Bigg) + \cos(m\theta - Kt) J_m(k_{mn}r) \end{aligned} \tag{3.62}$$

with the important steady part being,

$$p_{st}^{(2,1)} = -\tfrac{1}{2\gamma K^2}\Big\{J_m(k_{mn}r) J''_m(k_{mn}r) + \tfrac{1}{r} J_m(k_{mn}r) J'_m(k_{mn}r) + J'_m(k_{mn}r)^2\Big\} \tag{3.63}$$

The terms necessary to establish the right-hand-side of Eq.(3.54) are now available.

$$\left[u_r^{(2,1)}\right]_t = \tfrac{2}{\gamma^2}\left[2J_m\left(k_{mn}\right)J_m'\left(k_{mn}r\right)+\left(1-\gamma\right)K^2 f'\left(r\right)\right]\cos 2\left(m\theta-Kt\right)$$
$$-\tfrac{1}{\gamma}J_m'\left(k_{mn}r\right)\cos\left(m\theta-Kt\right)+\tfrac{1}{2K^2\gamma^2}\left[\begin{array}{l}2\tfrac{m^2}{r^3}J_m^2\left(k_{mn}r\right)-\left(\tfrac{1}{r^2}+2\tfrac{m^2}{r^2}-2K^2\right)J_m\left(k_{mn}\right)J_m'\left(k_{mn}r\right)\\+\tfrac{1}{r}\left(J_m'^{\,2}\left(k_{mn}r\right)+J_m\left(k_{mn}\right)J_m''\left(k_{mn}r\right)+J_m\left(k_{mn}\right)J_m'''\left(k_{mn}r\right)\right)\end{array}\right] \tag{3.64}$$

Given that the azimuthal component is

$$\left[u_\theta^{(2,1)}\right]_t = \tfrac{1}{\gamma}\left(\tfrac{m}{r}\right)\left\{-J_m\left(k_{mn}r\right)\sin\left(m\theta-Kt\right)+\tfrac{4}{\gamma}\left[J_m^2\left(k_{mn}r\right)+K^2\left(1-\gamma\right)f\left(r\right)\right]\sin 2\left(m\theta-Kt\right)\right\} \tag{3.65}$$

one may integrate (3.65) to obtain,

$$\begin{aligned}u_r^{(2,1)} = &-\tfrac{1}{\gamma^2 K}\left[2J_m\left(k_{mn}\right)J_m'\left(k_{mn}r\right)+\left(1-\gamma\right)K^2 f'\left(r\right)\right]\sin 2\left(m\theta-Kt\right)\\&+\tfrac{1}{\gamma K}\sin\left(m\theta-Kt\right)J_m'\left(k_{mn}r\right)\end{aligned} \tag{3.66}$$

and,

$$u_\theta^{(2,1)} = \tfrac{2}{\gamma K}\left(\tfrac{m}{r}\right)\left\{J_m\left(k_{mn}r\right)\cos\left(m\theta-Kt\right)-\tfrac{1}{\gamma}\left[J_m^2\left(k_{mn}r\right)+K^2\left(1-\gamma\right)f\left(r\right)\right]\cos 2\left(m\theta-Kt\right)\right\} \tag{3.67}$$

Next attention is turned to the wave equation to the second order in epsilon and the second order in the injection Mach number. Equation (3.37) becomes

$$\nabla^2 p^{(2,2)} - p_{tt}^{(2,2)} = 3F\left(r\right)+3B\left(r\right)\cos 2\left(m\theta-Kt\right) \tag{3.68}$$

The solution to Eq. (3.68) is easily found to be

$$p^{(2,2)} = \frac{-3}{2\gamma K^2}\left\{\left[\left(\frac{m}{r}\right)^2 + K^2\right]J_m\left(k_{mn}r\right)^2 - J'_m\left(k_{mn}r\right)^2 - 4K^4\left(\gamma-1\right)f\left(r\right)\right\}\cos 2\left(m\theta - Kt\right)$$
$$-\frac{3}{2\gamma K^2}\left\{J_m\left(k_{mn}r\right)J''_m\left(k_{mn}r\right) + \frac{1}{r}J_m\left(k_{mn}r\right)J'_m\left(k_{mn}r\right) + J'_m\left(k_{mn}r\right)^2\right\} + \cos\left(m\theta - Kt\right)J_m\left(k_{mn}r\right)$$

(3.69)

with the steady part being

$$p_{st}^{(2,2)} = -\frac{3}{2\gamma K^2}\left\{J_m\left(k_{mn}r\right)J''_m\left(k_{mn}r\right) + \frac{1}{r}J_m\left(k_{mn}r\right)J'_m\left(k_{mn}r\right) + J'_m\left(k_{mn}r\right)^2\right\} \tag{3.70}$$

As in the previous section, the wave equation is further expanded in terms of the injection Mach number. The approximation to the set of second-order equations displays a pattern that is of familiar type. The expression for the second order unsteady pressure can be written in a general form with respect to the $p^{(2,0)}$ term:

$$p^{(2)} = \sum_{n=0}^{\infty} M_b^n\left[\left(n+1\right)p_p^{(2,0)} + p^{(1,0)}\right] = \frac{p^{(2,0)} + \left(1-M_b\right)\cos\left(m\theta - Kt\right)J_m\left(k_{mn}r\right)}{\left(1-M_b\right)^2} \tag{3.71}$$

With the proper flow variables in hand it's now possible to extend the unsteady velocity to a higher order. Equation (3.55) becomes

$$\left[u_r^{(2,2)}\right]_t = \frac{3}{\gamma^2}\left[2J_m\left(k_{mn}r\right)J'_m\left(k_{mn}r\right) + \left(1-\gamma\right)K^2 f'\left(r\right)\right]\cos 2\left(m\theta - Kt\right)$$
$$-\frac{J'_m\left(k_{mn}r\right)}{\gamma}\cos\left(m\theta - Kt\right) + \frac{3J_m\left(k_{mn}r\right)}{4K^2\gamma^2 r}\left[\begin{array}{l}\frac{2m^2}{r^2}J_m^2\left(k_{mn}r\right) - 2\left(\frac{1}{2r} + \frac{m^2}{r} - rK^2\right)J'_m\left(k_{mn}r\right)\\ +J_m^{-1}\left(k_{mn}r\right)J'^{\,2}_m\left(k_{mn}r\right) + J''_m\left(k_{mn}r\right) + J'''_m\left(k_{mn}r\right)\end{array}\right] \tag{3.72}$$

with the azimuthal direction giving,

$$\left[u_\theta^{(2,1)}\right]_t = \tfrac{1}{\gamma}\left(\tfrac{m}{r}\right)\left\{-J_m\left(k_{mn}r\right)\sin\left(m\theta - Kt\right) + \tfrac{6}{\gamma}\left[J_m^2\left(k_{mn}r\right) + K^2\left(1-\gamma\right)f\left(r\right)\right]\sin 2\left(m\theta - Kt\right)\right\} \quad (3.73)$$

Integration leads to expressions for the second order velocity profile in both ε and the injection Mach number, $\mathcal{O}(2,2)$, as follows

$$\begin{aligned} u_r^{(2,2)} = &-\tfrac{3}{2\gamma^2 K}\left[2J_m\left(k_{mn}\right)J_m'\left(k_{mn}r\right) + \left(1-\gamma\right)K^2 f'\left(r\right)\right]\sin 2\left(m\theta - Kt\right) \\ &+ \tfrac{1}{\gamma K}\sin\left(m\theta - Kt\right)J_m'\left(k_{mn}r\right) \end{aligned} \quad (3.74)$$

and

$$u_\theta^{(2,2)} = \tfrac{3}{\gamma K}\left(\tfrac{m}{r}\right)\left\{J_m\left(k_{mn}r\right)\cos\left(m\theta - Kt\right) - \tfrac{1}{\gamma}\left[J_m^2\left(k_{mn}r\right) + K^2\left(1-\gamma\right)f\left(r\right)\right]\cos 2\left(m\theta - Kt\right)\right\} \quad (3.75)$$

The second-order momentum equation may be expanded along similar lines as the second order pressure. One gets

$$\boldsymbol{u}^{(2)} = \sum_{j=0}^{\infty} M_b^j\left[\left(n+1\right)\boldsymbol{u}_p^{(2,0)} + \boldsymbol{u}^{(1,0)}\right] = \frac{\left(1-M_b\right)\boldsymbol{u}^{(1,0)} + \boldsymbol{u}^{(2,0)}}{\left(1-M_b\right)^2} \quad (3.76)$$

where

$$\boldsymbol{u}_p^{(2,0)} = \begin{cases} -\dfrac{1}{2\gamma^2 K}\left[2J_m\left(k_{mn}\right)J_m'\left(k_{mn}r\right) + \left(1-\gamma\right)K^2 f'\left(r\right)\right]\sin\left[2\left(m\theta - Kt\right)\right]\boldsymbol{e}_r \\ -\dfrac{1}{\gamma^2 K}\left(\dfrac{m}{r}\right)\left[J_m^2\left(k_{mn}r\right) + K^2\left(1-\gamma\right)f\left(r\right)\right]\cos\left[2\left(m\theta - Kt\right)\right]\boldsymbol{e}_\theta \\ +\left(0\right)\boldsymbol{e}_z \end{cases} \quad (3.77)$$

Recalling Schlichting's[32] description of secondary flow (p. 430), namely, that "a potential flow which is periodic with respect to time induces a steady, secondary ('streaming') mo-

tion as a result of viscous forces." It is realized that a viscous model must be pursued in order to suitably capture the second-order interactions, as attempted in similar context by Maslen and Moore.[11]

4. Viscous Theory

Attention is now turned to the region directly above the headwall, specifically to the viscous boundary layer that must develop as a result of transverse shear parallel to the injector faceplate. This boundary layer is necessary to bring the transverse components of the velocity, both tangential and radial, to vanish at the surface. Friction at the headwall permits the attainment of a more realistic representation of the fluid motion. The ensuing flowfield must, on the one hand, satisfy the no slip condition at the headwall and, on the other hand, merge with the outer solution in the farfield. Assuming that all viscous effects are contained within a small region near the headwall, the present study ignores the sidewall boundary layer.

4.1. First Order Boundary Layer

In the attempt to unravel the acoustic streaming motion induced by viscous effects at the injector faceplate, the boundary layer equations at the headwall must be established. Following standard perturbation practices, a coordinate transformation is introduced such that the z-coordinate is rescaled over the viscous thickness δ. The corresponding inner, slow variable becomes

$$\zeta = \frac{z}{\delta} \tag{4.1}$$

Starting with the first-order momentum equation,

$$\boldsymbol{u}_t^{(1)} = -M_b \nabla\left(\boldsymbol{U}\cdot\boldsymbol{u}^{(1)}\right) + M_b\left(\boldsymbol{U}\times\boldsymbol{\omega}^{(1)} + \boldsymbol{u}^{(1)}\times\boldsymbol{\Omega}^0\right) - \tfrac{1}{\gamma}\nabla p^{(1)} - \delta^2\nabla\times\boldsymbol{\omega}^{(1)} + \delta_d^2\nabla\left(\nabla\cdot\boldsymbol{u}^{(1)}\right) \tag{4.2}$$

an expansion in terms of ζ leads to a set of three linear second-order partial differential equations (PDEs). Expanding terms of the right-hand-side of Eq. (4.2) gives,

$$\delta_d^2 \nabla\left(\nabla\cdot\boldsymbol{u}^{(1)}\right)=\left\{\begin{array}{l}\delta_d^2\left[\dfrac{\partial^2 \boldsymbol{u}_r^{(1)}}{\partial r^2}+\dfrac{1}{r}\dfrac{\partial \boldsymbol{u}_r^{(1)}}{\partial r}-\dfrac{\boldsymbol{u}_r^{(1)}}{r^2}-\dfrac{1}{r^2}\dfrac{\partial \boldsymbol{u}_\theta^{(1)}}{\partial \theta}+\dfrac{1}{r}\dfrac{\partial^2 \boldsymbol{u}_\theta^{(1)}}{\partial r\,\partial\theta}+\dfrac{1}{\delta}\dfrac{\partial^2 \boldsymbol{u}_z^{(1)}}{\partial r\,\partial\zeta}\right]\boldsymbol{e}_r \\ +\delta_d^2\left[\dfrac{1}{r}\dfrac{\partial^2 \boldsymbol{u}_r^{(1)}}{\partial\theta\,\partial r}+\dfrac{1}{r^2}\dfrac{\partial \boldsymbol{u}_r^{(1)}}{\partial\theta}+\dfrac{1}{r^2}\dfrac{\partial^2 \boldsymbol{u}_\theta^{(1)}}{\partial\theta^2}+\dfrac{1}{r\delta}\dfrac{\partial^2 \boldsymbol{u}_z^{(1)}}{\partial\theta\,\partial\zeta}\right]\boldsymbol{e}_\theta \\ +\delta_d^2\left[\dfrac{1}{\delta}\dfrac{\partial^2 \boldsymbol{u}_r^{(1)}}{\partial\zeta\,\partial r}+\dfrac{1}{r\delta}\dfrac{\partial \boldsymbol{u}_r^{(1)}}{\partial\zeta}+\dfrac{1}{r\delta}\dfrac{\partial^2 \boldsymbol{u}_\theta^{(1)}}{\partial\zeta\,\partial\theta}+\dfrac{1}{\delta^2}\dfrac{\partial^2 \boldsymbol{u}_z^{(1)}}{\partial\zeta^2}\right]\boldsymbol{e}_z\end{array}\right\} \tag{4.3}$$

$$-\delta^2\nabla\times\boldsymbol{\omega}^{(1)}=\left\{\begin{array}{l}-\delta^2\left[\dfrac{1}{r}\left(\dfrac{\partial^2 \boldsymbol{u}_\theta^{(1)}}{\partial\theta\,\partial r}+\dfrac{1}{r}\dfrac{\partial \boldsymbol{u}_\theta^{(1)}}{\partial\theta}-\dfrac{1}{r}\dfrac{\partial^2 \boldsymbol{u}_r^{(1)}}{\partial\theta^2}\right)-\dfrac{1}{\delta}\left(\dfrac{1}{\delta}\dfrac{\partial^2 \boldsymbol{u}_r^{(1)}}{\partial\zeta^2}-\dfrac{\partial^2 \boldsymbol{u}_z^{(1)}}{\partial\zeta\,\partial r}\right)\right]\boldsymbol{e}_r \\ -\delta^2\left[\dfrac{1}{\delta}\left(\dfrac{1}{r}\dfrac{\partial^2 \boldsymbol{u}_z^{(1)}}{\partial\zeta\,\partial\theta}-\dfrac{1}{\delta}\dfrac{\partial^2 \boldsymbol{u}_\theta^{(1)}}{\partial\zeta^2}\right)-\left(\dfrac{\partial^2 \boldsymbol{u}_\theta^{(1)}}{\partial r^2}-\dfrac{\boldsymbol{u}_\theta^{(1)}}{r^2}+\dfrac{1}{r}\dfrac{\partial \boldsymbol{u}_\theta^{(1)}}{\partial r}-\dfrac{1}{r}\dfrac{\partial^2 \boldsymbol{u}_r^{(1)}}{\partial r\,\partial\theta}\right)\right]\boldsymbol{e}_\theta \\ -\dfrac{\delta^2}{r}\left[\left(\dfrac{1}{\delta}\dfrac{\partial \boldsymbol{u}_r^{(1)}}{\partial\zeta}+\dfrac{r}{\delta}\dfrac{\partial^2 \boldsymbol{u}_r^{(1)}}{\partial r\,\partial\zeta}-\dfrac{\partial \boldsymbol{u}_z^{(1)}}{\partial r}-\dfrac{\partial^2 \boldsymbol{u}_z^{(1)}}{\partial r^2}\right)-\left(\dfrac{1}{r}\dfrac{\partial^2 \boldsymbol{u}_z^{(1)}}{\partial\theta^2}-\dfrac{1}{\delta}\dfrac{\partial^2 \boldsymbol{u}_\theta^{(1)}}{\partial\theta\,\partial\zeta}\right)\right]\boldsymbol{e}_z\end{array}\right\} \tag{4.4}$$

and

$$M_b\boldsymbol{U}\times\boldsymbol{\omega}^{(1)}=-M_b\left(\frac{1}{\delta}\frac{\partial \boldsymbol{u}_r^{(1)}}{\partial\zeta}-\frac{\partial \boldsymbol{u}_z^{(1)}}{\partial r}\right)\boldsymbol{e}_r+M_b\left(\frac{1}{r}\frac{\partial \boldsymbol{u}_z^{(1)}}{\partial\theta}-\frac{1}{\delta}\frac{\partial \boldsymbol{u}_\theta^{(1)}}{\partial\zeta}\right)\boldsymbol{e}_\theta \tag{4.5}$$

$$-M_b\nabla\left(\boldsymbol{U}\cdot\boldsymbol{u}^{(1)}\right)=-M_b\frac{\partial u_z^{(1)}}{\partial r}\boldsymbol{e}_r-\frac{M_b}{r}\frac{\partial u_z^{(1)}}{\partial\theta}\boldsymbol{e}_\theta-\frac{M_b}{\delta}\frac{\partial u_z^{(1)}}{\partial\zeta}\boldsymbol{e}_z \tag{4.6}$$

$$-\tfrac{1}{\gamma}\nabla p^{(1)}=-\frac{1}{\gamma}\frac{\partial p^{(1)}}{\partial r}\boldsymbol{e}_r-\frac{1}{\gamma r}\frac{\partial p^{(1)}}{\partial\theta}\boldsymbol{e}_\theta-\frac{1}{\gamma\delta}\frac{\partial p^{(1)}}{\partial z}\boldsymbol{e}_z \tag{4.7}$$

making a group of PDEs out of Eq. (4.2),

$$
\begin{cases}
\left[u_r^{(1)}\right]_t = \frac{-M_b}{\delta}\frac{\partial u_r^{(1)}}{\partial \zeta} - \frac{1}{\gamma}\frac{\partial p^{(1)}}{\partial r} - \delta^2 \left[\begin{array}{l} \frac{1}{r}\left(\frac{\partial^2 u_\theta^{(1)}}{\partial\theta\,\partial r} + \frac{1}{r}\frac{\partial u_\theta^{(1)}}{\partial\theta} - \frac{1}{r}\frac{\partial^2 u_r^{(1)}}{\partial\theta^2}\right) \\ -\frac{1}{\delta}\left(\frac{1}{\delta}\frac{\partial^2 u_r^{(1)}}{\partial\zeta^2} - \frac{\partial^2 u_z^{(1)}}{\partial\zeta\,\partial r}\right) \end{array}\right] + \delta_d^2 \left[\begin{array}{l} \frac{\partial^2 u_r^{(1)}}{\partial r^2} + \frac{1}{r}\frac{\partial u_r^{(1)}}{\partial r} - \frac{u_r^{(1)}}{r^2} - \frac{1}{r^2}\frac{\partial u_\theta^{(1)}}{\partial\theta} \\ +\frac{1}{r}\frac{\partial^2 u_\theta^{(1)}}{\partial r\,\partial\theta} + \frac{1}{\delta}\frac{\partial^2 u_z^{(1)}}{\partial r\,\partial\zeta} \end{array}\right] \\
\left[u_\theta^{(1)}\right]_t = \frac{-M_b}{\delta}\frac{\partial u_\theta^{(1)}}{\partial \zeta} - \frac{1}{\gamma r}\frac{\partial p^{(1)}}{\partial\theta} - \delta^2 \left[\begin{array}{l} \frac{1}{\delta}\left(\frac{1}{r}\frac{\partial^2 u_z^{(1)}}{\partial\zeta\,\partial\theta} - \frac{1}{\delta}\frac{\partial^2 u_\theta^{(1)}}{\partial\zeta^2}\right) \\ -\left(\frac{\partial^2 u_\theta^{(1)}}{\partial r^2} - \frac{u_\theta^{(1)}}{r^2} + \frac{1}{r}\frac{\partial u_\theta^{(1)}}{\partial r} - \frac{1}{r}\frac{\partial^2 u_r^{(1)}}{\partial r\,\partial\theta}\right) \end{array}\right] + \delta_d^2 \left[\begin{array}{l} \frac{1}{r}\frac{\partial^2 u_r^{(1)}}{\partial\theta\,\partial r} + \frac{1}{r^2}\frac{\partial u_r^{(1)}}{\partial\theta} + \\ \frac{1}{r^2}\frac{\partial^2 u_\theta^{(1)}}{\partial\theta^2} + \frac{1}{r\delta}\frac{\partial^2 u_z^{(1)}}{\partial\theta\,\partial\zeta} \end{array}\right] \\
\left[u_z^{(1)}\right]_t = \frac{-M_b}{\delta}\frac{\partial u_z^{(1)}}{\partial \zeta} - \frac{1}{\gamma\delta}\frac{\partial p^{(1)}}{\partial z} - \frac{\delta^2}{r} \left[\begin{array}{l} \left(\frac{1}{\delta}\frac{\partial u_r^{(1)}}{\partial\zeta} + \frac{r}{\delta}\frac{\partial^2 u_r^{(1)}}{\partial r\,\partial\zeta} - \frac{\partial u_z^{(1)}}{\partial r} - \frac{\partial^2 u_z^{(1)}}{\partial r^2}\right) \\ -\left(\frac{1}{r}\frac{\partial^2 u_z^{(1)}}{\partial\theta^2} - \frac{1}{\delta}\frac{\partial^2 u_\theta^{(1)}}{\partial\theta\,\partial\zeta}\right) \end{array}\right] + \delta_d^2 \left[\begin{array}{l} \frac{1}{\delta}\frac{\partial^2 u_r^{(1)}}{\partial\zeta\,\partial r} + \frac{1}{r\delta}\frac{\partial u_r^{(1)}}{\partial\zeta} \\ +\frac{1}{r\delta}\frac{\partial^2 u_\theta^{(1)}}{\partial\zeta\,\partial\theta} + \frac{1}{\delta^2}\frac{\partial^2 u_z^{(1)}}{\partial\zeta^2} \end{array}\right]
\end{cases}
\tag{4.8}
$$

As is normally done in these types of expansions, terms of the zeroth order in δ are retained. Therefore for the region near the wall Eq. (4.8) becomes

$$
\begin{cases}
-iKu_r^{(1)} = -\dfrac{M_b}{\delta}\dfrac{\partial u_r^{(1)}}{\partial\zeta} - \dfrac{1}{\gamma}\dfrac{\partial p^{(1)}}{\partial r} + \dfrac{\partial^2 u_r^{(1)}}{\partial\zeta^2} \\
-iKu_\theta^{(1)} = -\dfrac{M_b}{\delta}\dfrac{\partial u_\theta^{(1)}}{\partial\zeta} - \dfrac{1}{\gamma r}\dfrac{\partial p^{(1)}}{\partial\theta} + \dfrac{\partial^2 u_\theta^{(1)}}{\partial\zeta^2} \\
-iKu_z^{(1)} = -\dfrac{M_b}{\delta}\dfrac{\partial u_z^{(1)}}{\partial\zeta} - \dfrac{1}{\gamma\delta}\dfrac{\partial p^{(1)}}{\partial z} + \dfrac{\delta_d^2}{\delta^2}\dfrac{\partial^2 u_z^{(1)}}{\partial\zeta^2}
\end{cases}
\tag{4.9}
$$

Focusing on the azimuthal direction:

$$
\frac{\partial^2 u_\theta^{(1)}}{\partial\zeta^2} - \frac{M_b}{\delta}\frac{\partial u_\theta^{(1)}}{\partial\zeta} + iKu_\theta^{(1)} = \frac{1}{\gamma r}\frac{\partial p^{(1)}}{\partial\theta}
\tag{4.10}
$$

Owing to the fact that M_b/δ is not small, all terms on the left-hand-side of Eq. (4.10) are of order unity. Using the outer pressure from the potential flowfield to represent $p^{(1)}$,

one collects

$$\frac{\partial^2 u_\theta^{(1)}}{\partial \zeta^2} - \frac{M_b}{\delta}\frac{\partial u_\theta^{(1)}}{\partial \zeta} + iKu_\theta^{(1)} = \frac{i}{\gamma}\frac{1}{\left(1-M_b\right)}\left(\frac{m}{r}\right)J_m\left(k_{mn}r\right)e^{i\left(m\theta - Kt\right)} \tag{4.11}$$

The particular integral for Eq. (4.11) may be readily evaluated such that a compact solution is deduced. One gets

$$\left[u_\theta^{(1)}\right]_p = \frac{1}{\gamma K}\frac{1}{\left(1-M_b\right)}\left(\frac{m}{r}\right)J_m\left(k_{mn}r\right)e^{i\left(m\theta - Kt\right)} \tag{4.12}$$

In turn, the homogenous solution takes the form

$$\left[u_\theta^{(1)}\right]_h = A_\theta\left(r,\theta,t\right)e^{X_1\zeta} + B_\theta\left(r,\theta,t\right)e^{X_2\zeta} \tag{4.13}$$

with

$$\left(X_1, X_2\right) = \frac{M_b}{2\delta}\left(1 \pm \sqrt{1-4iK\delta^2 M_b^{-2}}\right) = \frac{V_b}{2}\sqrt{\frac{R}{a_0\nu}}\left(1 \pm \sqrt{1-4iK\delta^2 M_b^{-2}}\right) \tag{4.14}$$

or

$$X_1 = \frac{M_b}{2\delta}\left(1 + \sqrt{\frac{1+\sqrt{1+16K^2\delta^4 M_b^{-4}}}{2}} - i\sqrt{\frac{-1+\sqrt{1+16K^2\delta^4 M_b^{-4}}}{2}}\right) \tag{4.15}$$

$$X_2 = \frac{M_b}{2\delta}\left(1 - \sqrt{\frac{1+\sqrt{1+16K^2\delta^4 M_b^{-4}}}{2}} + i\sqrt{\frac{-1+\sqrt{1+16K^2\delta^4 M_b^{-4}}}{2}}\right) \tag{4.16}$$

It can be easily demonstrated that $X_1 > 0$ and $X_2 < 0$. The total solution for the first-order boundary layer approximation becomes,

$$u_\theta^{(1)} = A_\theta\left(r,\theta,t\right)e^{X_1\zeta} + B_\theta\left(r,\theta,t\right)e^{X_2\zeta} + \frac{1}{\gamma K}\frac{1}{\left(1-M_b\right)}\left(\frac{m}{r}\right)J_m\left(k_{mn}r\right)e^{i(m\theta-Kt)} \tag{4.17}$$

Knowing that the velocity cannot increase unboundedly as $\zeta \to \infty,$ one must set $A_\theta\left(r,\theta,t\right) = 0$. This leaves the second constant in Eq. (4.17) to satisfy the no slip condition at the chamber headwall. Subsequently, one puts

$$u_\theta^{(1)}\left(r,\theta,0,t\right) = B_\theta\left(r,\theta,t\right) + \frac{1}{\gamma K}\frac{1}{\left(1-M_b\right)}\left(\frac{m}{r}\right)J_m\left(k_{mn}r\right)e^{i(m\theta-Kt)} = 0 \tag{4.18}$$

whence

$$B_\theta\left(r,\theta,t\right) = -\frac{1}{\gamma K}\frac{1}{\left(1-M_b\right)}\left(\frac{m}{r}\right)J_m\left(k_{mn}r\right)e^{i(m\theta-Kt)} \tag{4.19}$$

and so

$$u_\theta^{(1)}(r,\theta,\zeta,t) = \frac{1}{\gamma K}\frac{1}{\left(1-M_b\right)}\left(\frac{m}{r}\right)J_m\left(k_{mn}r\right)e^{i(m\theta-Kt)}\left(1-e^{X_2\zeta}\right) \tag{4.20}$$

It may be useful to remark that $u_\theta^{(1)}(1,\theta,\zeta,t) \neq 0$. The radial velocity fluctuation does not observe the velocity adherence condition at the sidewall. As stated earlier, this outcome is due to the deliberate dismissal of the sidewall boundary layer. Effectively the analysis is limited to the wave/headwall interaction where the pertinent boundary conditions are

satisfied. In the radial direction, Eq. (4.9) yields

$$\frac{\partial^2 u_r^{(1)}}{\partial \zeta^2} - \frac{M_b}{\delta}\frac{\partial u_r^{(1)}}{\partial \zeta} + iKu_r^{(1)} = \frac{1}{\gamma}\frac{\partial p^{(1)}}{\partial r} \tag{4.21}$$

Substituting the pressure from the outer potential flow solution, we get

$$\frac{\partial^2 u_r^{(1)}}{\partial \zeta^2} - \frac{M_b}{\delta}\frac{\partial u_r^{(1)}}{\partial \zeta} + iKu_r^{(1)} = \frac{1}{\gamma}\frac{J'_m\left(k_{mn}r\right)}{\left(1-M_b\right)}e^{i(m\theta - Kt)} \tag{4.22}$$

The particular integral delivers

$$\left[u_r^{(1)}\right]_p = -\frac{i}{\gamma K}\frac{1}{\left(1-M_b\right)}J'_m\left(k_{mn}r\right)e^{i(m\theta - Kt)} \tag{4.23}$$

with the homogenous solution being of the form

$$\left[u_r^{(1)}\right]_h = A_r\left(r,\theta,t\right)e^{X_1\zeta} + B_r\left(r,\theta,t\right)e^{X_2\zeta} \tag{4.24}$$

Here one must set $A_r\left(r,\theta,t\right) = 0$ to prevent unboundedness in the downstream direction.

The complete solution for the first-order radial velocity approximation is therefore

$$u_r^{(1)} = B_r\left(r,\theta,t\right)e^{X_2\zeta} - \frac{i}{\gamma K}\frac{1}{\left(1-M_b\right)}J'_m\left(k_{mn}r\right)e^{i(m\theta - Kt)} \tag{4.25}$$

The no slip condition at the headwall permits extracting the final unknown

$$u_r^{(1)}\left(r,\theta,0,t\right) = B_r\left(r,\theta,t\right) - \frac{i}{\gamma K}\frac{1}{\left(1-M_b\right)}J'_m\left(k_{mn}r\right)e^{i(m\theta - Kt)} = 0 \tag{4.26}$$

or

$$B_r\left(r,\theta,t\right)=\frac{i}{\gamma K}\frac{1}{\left(1-M_b\right)}J'_m\left(k_{mn}r\right)e^{i\left(m\theta-Kt\right)} \tag{4.27}$$

Backward substitution yields, at length

$$u_r^{(1)}(r,\theta,\zeta,t)=\frac{i}{\gamma K}\frac{1}{\left(1-M_b\right)}J'_m\left(k_{mn}r\right)e^{i\left(m\theta-Kt\right)}\left(e^{X_2\zeta}-1\right) \tag{4.28}$$

The continuity equation can be used to extract the z component of velocity to the first order. Inserting $\gamma\rho^{(1)} = p^{(1)}$ into the first-order continuity expression into Eq. (2.7), one obtains

$$\frac{\partial p^{(1)}}{\partial t}=-\gamma\nabla\cdot\boldsymbol{u}^{(1)}-\gamma M_b\nabla\cdot\left[\frac{p^{(1)}}{\gamma}\boldsymbol{U}\right]=-\gamma\nabla\cdot\boldsymbol{u}^{(1)}-\cancel{M_b\boldsymbol{U}\cdot\nabla p^{(1)}}=-\gamma\nabla\cdot\boldsymbol{u}^{(1)} \tag{4.29}$$

which may be expanded in terms of the boundary layer coordinates into,

$$-iKp^{(1)}=-\gamma\left(\frac{\partial u_r}{\partial r}+\frac{u_r}{r}+\frac{1}{r}\frac{\partial u_\theta}{\partial\theta}+\frac{1}{\delta}\frac{\partial u_z}{\partial\zeta}\right) \tag{4.30}$$

Substituting Eqs (3.17), (4.20) and (4.28) into Eq. (4.30), on sets

$$\frac{\gamma}{\delta}\frac{\partial u_z}{\partial\zeta}=-\tfrac{1}{K}\begin{pmatrix} ie^{i\left(m\theta-Kt\right)}J''_m\left(k_{mn}r\right)\left[e^{X_2\zeta}-1\right]+\dfrac{i}{r}e^{i\left(m\theta-Kt\right)}J'_m\left(k_{mn}r\right)\left[e^{X_2\zeta}-1\right] \\ +i\left(\frac{m}{r}\right)^2J_m\left(k_{mn}r\right)e^{i\left(m\theta-Kt\right)}\left[1-e^{X_2\zeta}\right]-iK^2\left[e^{i\left(m\theta-Kt\right)}J_m\left(k_{mn}r\right)\right]\end{pmatrix} \tag{4.31}$$

then, noting that,

$$J_m''\left(k_{mn}r\right)+\tfrac{1}{r}J_m'\left(k_{mn}r\right)-\left(\tfrac{m}{r}\right)^2 J_m\left(k_{mn}r\right)+K^2 J_m\left(k_{mn}r\right)=0 \tag{4.32}$$

Equation (4.31) simplifies into

$$\frac{\partial u_z^{(1)}}{\partial \zeta}=-\frac{\delta}{K\gamma}\begin{pmatrix} ie^{i(m\theta-Kt)}J_m''\left(k_{mn}r\right)e^{X_2\zeta}+\dfrac{i}{r}e^{i(m\theta-Kt)}J_m'\left(k_{mn}r\right)e^{X_2\zeta} \\ -i\left(\tfrac{m}{r}\right)^2 J_m\left(k_{mn}r\right)e^{i(m\theta-Kt)}e^{X_2\zeta} \end{pmatrix} \tag{4.33}$$

Integration leads to

$$u_z^{(1)}=\tfrac{\delta K}{\gamma}\left(\tfrac{i}{X_2}\right)J_m\left(k_{mn}r\right)e^{i(m\theta-Kt)}e^{X_2\zeta}+A_z\left(r,\theta,t\right) \tag{4.34}$$

Unsteady injection, being a result of feedline pressure oscillations and various other upstream influences, is not molded in this study. Therefore, it is assumed that the z component of velocity must go to zero at the head end. The influence of unsteady injection and feedline pressure coupling on a combustion system's overall stability is quite significant and deserves investigation in future analysis. The assumed zero headwall axial velocity delivers

$$u_z^{(1)}\left(r,\theta,0,t\right)=\tfrac{\delta K}{\gamma}\left(\tfrac{i}{X_2}\right)J_m\left(k_{mn}r\right)e^{i(m\theta-Kt)}+A_z\left(r,\theta,t\right)=0 \tag{4.35}$$

whence

$$A_z\left(r,\theta,t\right)=-\frac{\delta K}{\gamma}\left(\frac{i}{X_2}\right)J_m\left(k_{mn}r\right)e^{i(m\theta-Kt)} \tag{4.36}$$

This yields

$$u_z^{(1)} = \tfrac{\delta K}{\gamma}\left(\tfrac{i}{X_2}\right) J_m\left(k_{mn} r\right) e^{i(m\theta - Kt)}\left[e^{X_2 \zeta} - 1\right] \tag{4.37}$$

The real parts of the solution can be summarized as,

$$\boldsymbol{u}^{(1)} = \frac{J_m\left(k_{mn} r\right)}{\gamma K\left(1 - M_b\right)} \left\{ \begin{aligned} &\frac{J_m'\left(k_{mn} r\right)}{J_m\left(k_{mn} r\right)} \left[\underbrace{\overbrace{\sin\left(m\theta - Kt\right)}^{\text{irrotational part}}}_{\text{inviscid outer field}} \; \underbrace{-\overbrace{\sin\left(m\theta + X_i\,\zeta - Kt\right)}^{\text{rotational part}} \underbrace{e^{X_r \zeta}}_{\text{decay}}}_{\text{wave propagation}} \right] \boldsymbol{e}_r \\ &+ \left(\frac{m}{r}\right)\left[\cos\left(m\theta - Kt\right) - \cos\left(m\theta + X_i\,\zeta - Kt\right) e^{X_r \zeta}\right] \boldsymbol{e}_\theta \\ &+ \frac{\delta K^2}{X_r^2 + X_i^2} \left\{ \begin{aligned} &X_r\left[\sin\left(m\theta - Kt\right) - e^{X_r \zeta} \sin\left(m\theta + X_i\,\zeta - Kt\right)\right] \\ &-X_i\left[\cos\left(m\theta - Kt\right) - e^{X_r \zeta} \cos\left(m\theta + X_i\,\zeta - Kt\right)\right] \end{aligned} \right\} \boldsymbol{e}_z \end{aligned} \right. \tag{4.38}$$

where $X_2 = X = X_r + iX_i$ may be synthesized from

$$\left\{ \begin{aligned} X_r &= \frac{M_b}{2\delta}\left(1 - \sqrt{\frac{1 + \sqrt{1 + 16K^2\delta^4 M_b^{-4}}}{2}}\right) \approx \frac{M_b}{2\delta}\left(1 - \sqrt{1 + 4K^2\delta^4 M_b^{-4}}\right) \approx -\frac{\delta^3 K^2}{M_b^3} = -\frac{\delta}{S_p} \\ X_i &= \frac{M_b}{2\delta}\sqrt{\frac{\sqrt{1 + 16K^2\delta^4 M_b^{-4}} - 1}{2}} \approx \frac{M_b}{2\delta}\sqrt{\frac{8K^2\delta^4 M_b^{-4}}{2}} \approx \frac{\delta K}{M_b} = \delta S \end{aligned} \right. \tag{4.39}$$

It may be useful to remark that the tangential component of the velocity does not vanish at the sidewall. Its behavior in the vicinity of $r = 1$ deteriorates to the extent of overshooting the expected value in the absence of fluid friction at the sidewall. The domain of analysis is therefore limited to a large diameter chamber with the exclusion of the sidewall. Such a model may be deemed acceptable considering that the principal objective here lies in the treatment of the mean flow interactions with the wave motion directly above the headwall.

It is well known that the acoustic streaming, being the chief focus here, is a secondary flow. In order to obtain the steady secondary flows a higher order solution is needed. To that and the viscous solution is extended to the second order in the wave amplitude, ε.

4.2. Second Order Boundary Layer

In what follows, it is shown that extending the boundary layer analysis to the second order in the wave parameter gives rise to a steady flow component that has its origin in the interaction between viscosity and inertia. To this end, the second-order momentum equation, defined in Eq. (2.8), is recast using the stretched inner coordinate ζ. Rewriting the second order momentum equation in Eq. (2.8) gives

$$\begin{aligned}\frac{\partial \boldsymbol{u}^{(2)}}{\partial t} = &-\frac{\nabla p^{(2)}}{\gamma} - \rho^{(1)}\frac{\partial \boldsymbol{u}^{(1)}}{\partial t} - \tfrac{1}{2}\nabla\left(\boldsymbol{u}^{(1)}\cdot\boldsymbol{u}^{(1)}\right) + \boldsymbol{u}^{(1)}\times\boldsymbol{\omega}^{(1)} + \delta_d^2\nabla\left[\nabla\cdot\boldsymbol{u}^{(2)}\right] - \delta^2\nabla\times\boldsymbol{\omega}^{(2)} \\ &- M_b\left\{\nabla\left(\boldsymbol{U}\cdot\boldsymbol{u}^{(2)}\right) - \boldsymbol{u}^{(2)}\times\boldsymbol{\Omega}^0 - \boldsymbol{U}\times\boldsymbol{\omega}^{(2)} - \tfrac{1}{\gamma}p^{(1)}\left[\nabla\left(\boldsymbol{U}\cdot\boldsymbol{u}^{(1)}\right) - \boldsymbol{u}^{(1)}\times\boldsymbol{\Omega}^0 - \boldsymbol{U}\times\boldsymbol{\omega}^{(1)}\right]\right\}\end{aligned} \tag{4.40}$$

Using a suitable boundary layer coordinate transformation, terms on the right-hand-side of Eq. (4.40) become,

$$\delta_d^2\nabla\left[\nabla\cdot\boldsymbol{u}^{(2)}\right] = \delta_d^2\left\{\begin{aligned}&\left[\frac{\partial^2 u_r^{(2)}}{\partial r^2} + \frac{1}{r}\frac{\partial u_r^{(2)}}{\partial r} - \frac{u_r^{(2)}}{r^2} - \frac{1}{r^2}\frac{\partial u_\theta^{(2)}}{\partial\theta} + \frac{1}{r}\frac{\partial^2 u_\theta^{(2)}}{\partial r\partial\theta} + \frac{1}{\delta}\frac{\partial^2 u_z^{(2)}}{\partial r\partial\zeta}\right]\boldsymbol{e}_r \\ &+\left[\frac{1}{r}\frac{\partial^2 u_r^{(2)}}{\partial\theta\partial r} + \frac{1}{r^2}\frac{\partial u_r^{(2)}}{\partial\theta} + \frac{1}{r^2}\frac{\partial^2 u_\theta^{(2)}}{\partial\theta^2} + \frac{1}{r\delta}\frac{\partial^2 u_z^{(2)}}{\partial\theta\partial\zeta}\right]\boldsymbol{e}_\theta \\ &+\left[\frac{1}{\delta}\frac{\partial^2 u_r^{(2)}}{\partial\zeta\partial r} + \frac{1}{r\delta}\frac{\partial u_r^{(2)}}{\partial\zeta} + \frac{1}{r\delta}\frac{\partial^2 u_\theta^{(2)}}{\partial\zeta\partial\theta} + \frac{1}{\delta^2}\frac{\partial^2 u_z^{(2)}}{\partial\zeta^2}\right]\boldsymbol{e}_z\end{aligned}\right\} \tag{4.41}$$

$$-\delta^2\nabla\times\boldsymbol{u}^{(2)}=\delta^2\left\{\begin{array}{l}\left[-\frac{1}{r}\left(\frac{\partial^2 u_\theta^{(2)}}{\partial\theta\partial r}+\frac{1}{r}\frac{\partial u_\theta^{(2)}}{\partial\theta}-\frac{1}{r}\frac{\partial^2 u_r^{(2)}}{\partial\theta^2}\right)-\frac{1}{\delta}\left(\frac{1}{\delta}\frac{\partial^2 u_r^{(2)}}{\partial\zeta^2}-\frac{\partial^2 u_z^{(2)}}{\partial\zeta\partial r}\right)\right]\boldsymbol{e}_r\\ -\left[\frac{1}{\delta}\left(\frac{1}{r}\frac{\partial^2 u_z^{(2)}}{\partial\zeta\partial\theta}-\frac{1}{\delta}\frac{\partial^2 u_\theta^{(2)}}{\partial\zeta^2}\right)+\left(-\frac{\partial^2 u_\theta^{(2)}}{\partial r^2}-\frac{1}{r}\frac{\partial u_\theta^{(2)}}{\partial r}+\frac{u_\theta^{(2)}}{r^2}+\frac{1}{r}\frac{\partial^2 u_r^{(2)}}{\partial r\partial\theta}\right)\right]\boldsymbol{e}_\theta\\ -\frac{1}{r}\left[\left(\frac{1}{\delta}\frac{\partial u_r^{(2)}}{\partial\zeta}+\frac{r}{\delta}\frac{\partial^2 u_r^{(2)}}{\partial r\partial\zeta}-\frac{\partial u_z^{(2)}}{\partial r}-\frac{\partial^2 u_z^{(2)}}{\partial r^2}\right)-\left(\frac{1}{r}\frac{\partial^2 u_z^{(2)}}{\partial\theta^2}-\frac{1}{\delta}\frac{\partial^2 u_\theta^{(2)}}{\partial\theta\partial\zeta}\right)\right]\boldsymbol{e}_z\end{array}\right\} \quad (4.42)$$

$$-\tfrac{1}{2}\nabla\left(\boldsymbol{u}^{(1)}\cdot\boldsymbol{u}^{(1)}\right)=\left\{\begin{array}{l}-\left[u_r^{(1)}\frac{\partial u_r^{(1)}}{\partial r}+u_\theta^{(1)}\frac{\partial u_\theta^{(1)}}{\partial r}+u_z^{(1)}\frac{\partial u_z^{(1)}}{\partial r}\right]\boldsymbol{e}_r\\ -\frac{1}{r}\left[u_r^{(1)}\frac{\partial u_r^{(1)}}{\partial\theta}+u_\theta^{(1)}\frac{\partial u_\theta^{(1)}}{\partial\theta}+u_z^{(1)}\frac{\partial u_z^{(1)}}{\partial\theta}\right]\boldsymbol{e}_\theta\\ -\frac{1}{\delta}\left[u_r^{(1)}\frac{\partial u_r^{(1)}}{\partial\zeta}+u_\theta^{(1)}\frac{\partial u_\theta^{(1)}}{\partial\zeta}+u_z^{(1)}\frac{\partial u_z^{(1)}}{\partial\zeta}\right]\boldsymbol{e}_z\end{array}\right\} \quad (4.43)$$

$$\boldsymbol{u}^{(1)}\times\boldsymbol{u}^{(1)}=\left\{\begin{array}{l}\left[u_\theta^{(1)}\left(\frac{\partial u_\theta^{(1)}}{\partial r}+\frac{u_\theta^{(1)}}{r}-\frac{1}{r}\frac{\partial u_r^{(1)}}{\partial\theta}\right)-u_z^{(1)}\left(\frac{1}{\delta}\frac{\partial u_r^{(1)}}{\partial\zeta}-\frac{\partial u_z^{(1)}}{\partial r}\right)\right]\boldsymbol{e}_r\\ +\left[u_z^{(1)}\left(\frac{1}{r}\frac{\partial u_z^{(1)}}{\partial\theta}-\frac{1}{\delta}\frac{\partial u_\theta^{(1)}}{\partial\zeta}\right)-u_r^{(1)}\left(\frac{\partial u_\theta^{(1)}}{\partial r}+\frac{u_\theta^{(1)}}{r}-\frac{1}{r}\frac{\partial u_r^{(1)}}{\partial\theta}\right)\right]\boldsymbol{e}_\theta\\ +\left[u_r^{(1)}\left(\frac{1}{\delta}\frac{\partial u_r^{(1)}}{\partial\zeta}-\frac{\partial u_z^{(1)}}{\partial r}\right)-u_\theta^{(1)}\left(\frac{1}{r}\frac{\partial u_z^{(1)}}{\partial\theta}-\frac{1}{\delta}\frac{\partial u_\theta^{(1)}}{\partial\zeta}\right)\right]\boldsymbol{e}_z\end{array}\right\} \quad (4.44)$$

and

$$\frac{-M_b}{\gamma}p^{(1)}\nabla\left(\boldsymbol{U}\cdot\boldsymbol{u}^{(1)}\right)=\frac{-M_b}{\gamma}\left(p^{(1)}\frac{\partial u_z^{(1)}}{\partial r}\boldsymbol{e}_r+\frac{p^{(1)}}{r}\frac{\partial u_z^{(1)}}{\partial\theta}\boldsymbol{e}_\theta+\frac{p^{(1)}}{\delta}\frac{\partial u_z^{(1)}}{\partial\zeta}\boldsymbol{e}_z\right) \quad (4.45)$$

$$\frac{M_b}{\gamma}p^{(1)}\left(\boldsymbol{U}\times\boldsymbol{u}^{(1)}\right)=\frac{-M_b}{\gamma}p^{(1)}\left(\frac{1}{\delta}\frac{\partial u_r^{(1)}}{\partial\zeta}-\frac{\partial u_z^{(1)}}{\partial r}\right)\boldsymbol{e}_r+\frac{M_b}{\gamma}p^{(1)}\left(\frac{1}{r}\frac{\partial u_z^{(1)}}{\partial\theta}-\frac{1}{\delta}\frac{\partial u_\theta^{(1)}}{\partial\zeta}\right)\boldsymbol{e}_\theta+(0)_{\boldsymbol{e}_z} \quad (4.46)$$

$$-M_b\nabla\left(\boldsymbol{U}\cdot\boldsymbol{u}^{(2)}\right)=-M_b\left(\frac{\partial u_z^{(2)}}{\partial r}\boldsymbol{e_r}+\frac{1}{r}\frac{\partial u_z^{(2)}}{\partial\theta}\boldsymbol{e}_\theta+\frac{1}{\delta}\frac{\partial u_z^{(2)}}{\partial\zeta}\boldsymbol{e}_z\right) \tag{4.47}$$

$$M_b\left[\boldsymbol{U}\times\boldsymbol{u}^{(2)}\right]=-M_b\left(\frac{1}{\delta}\frac{\partial u_r^{(2)}}{\partial\zeta}-\frac{\partial u_z^{(2)}}{\partial r}\right)\boldsymbol{e}_r+M_b\left(\frac{1}{r}\frac{\partial u_z^{(2)}}{\partial\theta}-\frac{1}{\delta}\frac{\partial u_\theta^{(2)}}{\partial\zeta}\right)\boldsymbol{e}_\theta+(0)\boldsymbol{e}_z \tag{4.48}$$

Equation (4.40) can now be written in component form as

$$\begin{aligned}\frac{\partial u_r^{(2)}}{\partial t}=&-\frac{M_b}{\delta}\frac{\partial u_r^{(2)}}{\partial\zeta}-\frac{p^{(1)}}{\gamma}\left[\frac{M_b}{\delta}\frac{\partial u_r^{(1)}}{\partial\zeta}+\frac{\partial u_r^{(1)}}{\partial t}\right]-\left\{\frac{u_z^{(1)}}{\delta}\frac{\partial u_r^{(1)}}{\partial\zeta}+u_r^{(1)}\frac{\partial u_r^{(1)}}{\partial r}+\frac{u_\theta^{(1)}}{r}\left[\frac{\partial u_r^{(1)}}{\partial\theta}-u_\theta^{(1)}\right]\right\}\\&-\frac{1}{\gamma}\frac{\partial p^{(2)}}{\partial r}-\delta^2\left\{\frac{1}{r}\left[\frac{\partial^2u_\theta^{(2)}}{\partial\theta\,\partial r}+\frac{1}{r}\frac{\partial u_\theta^{(2)}}{\partial\theta}-\frac{1}{r}\frac{\partial^2u_r^{(2)}}{\partial\theta^2}\right]-\frac{1}{\delta}\left[\frac{1}{\delta}\frac{\partial^2u_r^{(2)}}{\partial\zeta^2}-\frac{\partial^2u_z^{(2)}}{\partial\zeta\,\partial r}\right]\right\}\\&+\delta_d^2\left[\frac{\partial^2u_r^{(2)}}{\partial r^2}+\frac{1}{r}\frac{\partial u_r^{(2)}}{\partial r}-\frac{u_r^{(2)}}{r^2}-\frac{1}{r^2}\frac{\partial u_\theta^{(2)}}{\partial\theta}+\frac{1}{r}\frac{\partial^2u_\theta^{(2)}}{\partial r\,\partial\theta}+\frac{1}{\delta}\frac{\partial^2u_z^{(2)}}{\partial r\,\partial\zeta}\right]\end{aligned} \tag{4.49}$$

$$\begin{aligned}\frac{\partial u_\theta^{(2)}}{\partial t}=&\frac{-M_b}{\delta}\frac{\partial u_\theta^{(2)}}{\partial\zeta}-\frac{1}{\gamma r}\frac{\partial p^{(2)}}{\partial\theta}+\delta_d^2\left[\frac{1}{r}\frac{\partial^2u_r^{(2)}}{\partial\theta\,\partial r}+\frac{1}{r^2}\frac{\partial u_r^{(2)}}{\partial\theta}+\frac{1}{r^2}\frac{\partial^2u_\theta^{(2)}}{\partial\theta^2}+\frac{1}{r\delta}\frac{\partial^2u_z^{(2)}}{\partial\theta\,\partial\zeta}\right]\\&-\delta^2\left\{\frac{1}{\delta}\left[\frac{1}{r}\frac{\partial^2u_z^{(2)}}{\partial\zeta\,\partial\theta}-\frac{1}{\delta}\frac{\partial^2u_\theta^{(2)}}{\partial\zeta^2}\right]-\left[\frac{\partial^2u_\theta^{(2)}}{\partial r^2}-\frac{u_\theta^{(2)}}{r^2}+\frac{1}{r}\frac{\partial u_\theta^{(2)}}{\partial r}-\frac{1}{r}\frac{\partial^2u_r^{(2)}}{\partial r\,\partial\theta}\right]\right\}\\&-\frac{p^{(1)}}{\gamma}\left[\frac{M_b}{\delta}\frac{\partial u_\theta^{(1)}}{\partial\zeta}+\frac{\partial u_\theta^{(1)}}{\partial t}\right]-\left[\frac{u_z^{(1)}}{\delta}\frac{\partial u_\theta^{(1)}}{\partial\zeta}+\frac{u_\theta^{(1)}}{r}\frac{\partial u_\theta^{(1)}}{\partial\theta}+u_r^{(1)}\left(\frac{u_\theta^{(1)}}{r}+\frac{\partial u_\theta^{(1)}}{\partial r}\right)\right]\end{aligned} \tag{4.50}$$

$$\begin{aligned}\frac{\partial u_z^{(2)}}{\partial t}=&\frac{-M_b}{\delta}\frac{\partial u_z^{(2)}}{\partial\zeta}-\frac{1}{\gamma\delta}\frac{\partial p^{(2)}}{\partial\zeta}+\delta_d^2\left[\frac{1}{\delta}\frac{\partial^2u_r^{(2)}}{\partial\zeta\,\partial r}+\frac{1}{r\delta}\frac{\partial u_r^{(2)}}{\partial\zeta}+\frac{1}{r\,\delta}\frac{\partial^2u_\theta^{(2)}}{\partial\zeta\,\partial\theta}+\frac{1}{\delta^2}\frac{\partial^2u_z^{(2)}}{\partial\zeta^2}\right]\\&-\frac{\delta^2}{r}\left\{\left[\frac{1}{\delta}\frac{\partial u_r^{(2)}}{\partial\zeta}+\frac{r}{\delta}\frac{\partial^2u_r^{(2)}}{\partial r\,\partial\zeta}-\frac{\partial u_z^{(2)}}{\partial r}-\frac{\partial^2u_z^{(2)}}{\partial r^2}\right]-\left[\frac{1}{r}\frac{\partial^2u_z^{(2)}}{\partial\theta^2}-\frac{1}{\delta}\frac{\partial^2u_\theta^{(2)}}{\partial\theta\,\partial\zeta}\right]\right\}\\&-\frac{p^{(1)}}{\gamma}\left[\frac{M_b}{\delta}\frac{\partial u_z^{(1)}}{\partial\zeta}+\frac{\partial u_z^{(1)}}{\partial t}\right]-\left[\frac{u_z^{(1)}}{\delta}\frac{\partial u_z^{(1)}}{\partial\zeta}+u_r^{(1)}\frac{\partial u_z^{(1)}}{\partial r}+\frac{u_\theta^{(1)}}{r}\frac{\partial u_z^{(1)}}{\partial\theta}\right]\end{aligned} \tag{4.51}$$

Retaining only terms of the zeroth order in δ in the region near the wall, Eqs. (4.49)-(4.51) yield

$$\frac{\partial^2 u_r^{(2)}}{\partial \zeta^2} - \frac{M_b}{\delta}\frac{\partial u_r^{(2)}}{\partial \zeta} - \frac{\partial u_r^{(2)}}{\partial t} = \frac{1}{\gamma}\frac{\partial p^{(2)}}{\partial r} + \frac{p^{(1)}}{\gamma}\left[\frac{M_b}{\delta}\frac{\partial u_r^{(1)}}{\partial \zeta} + \frac{\partial u_r^{(1)}}{\partial t}\right] + \left[\frac{u_z^{(1)}}{\delta}\frac{\partial u_r^{(1)}}{\partial \zeta} + u_r^{(1)}\frac{\partial u_r^{(1)}}{\partial r} + \frac{u_\theta^{(1)}}{r}\left(\frac{\partial u_r^{(1)}}{\partial \theta} - u_\theta^{(1)}\right)\right] \tag{4.52}$$

$$\frac{\partial^2 u_\theta^{(2)}}{\partial \zeta^2} - \frac{M_b}{\delta}\frac{\partial u_\theta^{(2)}}{\partial \zeta} - \frac{\partial u_\theta^{(2)}}{\partial t} = \frac{1}{\gamma r}\frac{\partial p^{(2)}}{\partial \theta} + \frac{p^{(1)}}{\gamma}\left[\frac{M_b}{\delta}\frac{\partial u_\theta^{(1)}}{\partial \zeta} + \frac{\partial u_\theta^{(1)}}{\partial t}\right] + \left[\frac{u_z^{(1)}}{\delta}\frac{\partial u_\theta^{(1)}}{\partial \zeta} + \frac{u_\theta^{(1)}}{r}\frac{\partial u_\theta^{(1)}}{\partial \theta} + u_r^{(1)}\left(\frac{u_\theta^{(1)}}{r} + \frac{\partial u_\theta^{(1)}}{\partial r}\right)\right] \tag{4.53}$$

and,

$$\frac{\delta_d^2}{\delta^2}\frac{\partial^2 u_z^{(2)}}{\partial \zeta^2} - \frac{M_b}{\delta}\frac{\partial u_z^{(2)}}{\partial \zeta} - \frac{\partial u_z^{(2)}}{\partial t} = \frac{1}{\gamma\delta}\frac{\partial p^{(2)}}{\partial \zeta} + \frac{p^{(1)}}{\gamma}\left[\frac{M_b}{\delta}\frac{\partial u_z^{(1)}}{\partial \zeta} + \frac{\partial u_z^{(1)}}{\partial t}\right] + \left[\frac{u_z^{(1)}}{\delta}\frac{\partial u_z^{(1)}}{\partial \zeta} + \frac{u_\theta^{(1)}}{r}\frac{\partial u_z^{(1)}}{\partial \theta} + u_r^{(1)}\frac{\partial u_z^{(1)}}{\partial r}\right] \tag{4.54}$$

where terms involving the ratio M_b/δ will prove to be crucial. Solving the second-order equations requires greater algebraic detail. To illustrate the process, the solution in the radial direction is outlined. After substituting the first-order solution on the right-hand-side of Eq. (4.52), one recovers, for the steady part,

$$\frac{1}{\gamma}\frac{\partial p^{(2)}}{\partial r} = \frac{1}{2K^2\gamma^2\left(1-M_b\right)^2}\left[\frac{m^2}{r^3}J_m^2 + \left(K^2 - \frac{m^2}{r^2}\right)J_m J_m' - J_m' J_m''\right] \tag{4.55}$$

$$\frac{1}{\gamma}\frac{M_b}{\delta}p^{(1)}\frac{\partial u_r^{(1)}}{\partial\zeta}=\frac{-1}{2\gamma^2K\left(1-M_b\right)^2}\frac{M_b}{\delta}J_mJ'_me^{X_r\zeta}\left\{X_r\sin\left(X_i\zeta\right)+X_i\cos\left(X_i\zeta\right)\right\} \quad (4.56)$$

and

$$\frac{p^{(1)}}{\gamma}\frac{\partial u_r^{(1)}}{\partial t}=\frac{1}{2\gamma^2\left(1-M_b\right)^2}J_mJ'_m\left[e^{X_r\zeta}\cos\left(X_i\zeta\right)-1\right] \quad (4.57)$$

$$-u_\theta^{(1)}\frac{u_\theta^{(1)}}{r}=-\frac{1}{2\left(1-M_b\right)^2}\left(\frac{1}{\gamma K}\right)^2\frac{m^2}{r^3}J_m^2\left[1+e^{2X_r\zeta}-2e^{X_r\zeta}\cos\left(X_i\zeta\right)\right] \quad (4.58)$$

owing to

$$\frac{u_\theta^{(1)}}{r}\frac{\partial u_r^{(1)}}{\partial\theta}=\frac{1}{2\left(1-M_b\right)^2}\left(\frac{1}{\gamma K}\right)^2\frac{m^2}{r^2}J_mJ'_m\left[1+e^{2X_r\zeta}-2e^{X_r\zeta}\cos\left(X_i\zeta\right)\right] \quad (4.59)$$

$$\frac{u_z^{(1)}}{\delta}\frac{\partial u_r^{(1)}}{\partial\zeta}=\frac{J_mJ'_me^{X_r\zeta}\sin\left(X_i\zeta\right)}{2\gamma^2\left(1-M_b\right)^2\left(X_i^2+X_r^2\right)}\left[\left(X_r^2-X_i^2\right)\frac{e^{X_r\zeta}}{\sin\left(X_i\zeta\right)}+\left(X_i^2-X_r^2\right)\frac{\cos\left(X_i\zeta\right)}{\sin\left(X_i\zeta\right)}+2X_iX_r\right] \quad (4.60)$$

$$u_r^{(1)}\frac{\partial u_r^{(1)}}{\partial r}=\frac{1}{2K^2\gamma^2\left(1-M_b\right)^2}J'_mJ''_m\left[1+e^{2X_r\zeta}-2e^{X_r\zeta}\cos\left(X_i\zeta\right)\right] \quad (4.61)$$

Equation (4.52) can now be rewritten as

$$\frac{\partial^2u_r^{(2)}}{\partial\zeta^2}-\frac{M_b}{\delta}\frac{\partial u_r^{(2)}}{\partial\zeta}=RHS \quad (4.62)$$

with

$$RHS = \frac{1}{2K^2\gamma^2}\left\{\begin{array}{l}\left[\left(\frac{m^2}{r^2}+K^2-\frac{K^2X_r^2}{X_i^2+X_r^2}\right)J_mJ'_m-\frac{m^2}{r^3}J_m^2+J'_mJ''_m\right]e^{2X_r\zeta}\\+\left[\frac{2m^2}{r^3}J_m^2-\left(\frac{2m^2}{r^2}+\frac{M_bK}{\delta}X_i-2K^2X_i^2\right)J_mJ'_m-2J'_mJ''_m\right]e^{X_r\zeta}\cos\left(X_i\zeta\right)\\+K\left(\frac{2KX_iX_r}{X_i^2+X_r^2}-\frac{M_bX_r}{\delta}\right)J_mJ'_me^{X_r\zeta}\sin\left(X_i\zeta\right)\end{array}\right\} \quad (4.63)$$

Since the focus of this study is on the steady flow the term involving the partial derivative with respect to time has been removed. Solution to the above equation is gained through normal means, giving

$$u_r^{(2)} = \frac{1}{2K^2\gamma^2\left(1-M_b\right)^2}\left\{\begin{array}{l}\frac{\left[e^{2X_r\zeta}-1\right]}{2X_r\left(2X_r-\frac{M_b}{\delta}\right)}\left[\left(\frac{m^2}{r^2}+K^2\frac{X_r^2-X_i^2}{X_r^2+X_i^2}\right)J_mJ'_m-\frac{m^2}{r^3}J_m^2+J'_mJ''_m\right]\\+\Lambda_{r,1}\left[e^{X_r\zeta}\sin\left(X_i\zeta\right)\right]+\Lambda_{r,2}\left[e^{X_r\zeta}\cos\left(X_i\zeta\right)-1\right]\end{array}\right\} \quad (4.64)$$

with

$$\Lambda_{r,1} = \frac{1}{\beta_r}\left\{\begin{array}{l}\left[X_i\left(2\delta X_r-M_b\right)\right]\frac{2m^2}{r^3}J_m^2+\left[2\delta X_i\left(M_b-2\delta X_r\right)\right]\left(\frac{m^2}{r^2}J_mJ'_m+J'_mJ''_m\right)\\+K\left(M_b-\delta X_r\right)\left[M_b\left(X_i^2+X_r^2\right)-K\right]J_mJ'_m\end{array}\right\} \quad (4.65)$$

$$\Lambda_{r,2} = \frac{1}{\beta_r}\left\{\begin{array}{l}2\delta\left[\delta X_i^2+X_r\left(M_b-\delta X_r\right)\right]\left[J'_mJ''_m-\frac{m^2}{r^3}J_m^2\right]\\+\left[2\frac{m^2}{r^2}\delta^2\left(X_i^2-X_r^2+\frac{M_b}{\delta}X_r\right)+KM_b\delta X_i\left(X_i^2+X_r^2\right)\right]J_mJ'_m\end{array}\right\} \quad (4.66)$$

and

$$\beta_r = \left(X_r^2 + X_i^2\right)\left[\delta^2 X_i^2 + \left(M_b - \delta X_r\right)^2\right] \tag{4.67}$$

Note that the limitations of the analysis discussed during the derivation of the first order boundary layer solution appear in the second order solution as well. Specifically it is observed that the radial velocity does not go to zero at the chamber sidewall. This is a direct result of the square of the azimuthal velocity on the right-hand-side of Eq. (4.58) and further clarified in Eq. (4.52). In like manner the solution for the tangential direction may be extracted from Eq. (4.52) with the terms on the right-hand-side becoming

$$\frac{M_b}{\gamma\delta}\, p^{(1)}\, \frac{\partial u_\theta^{(1)}}{\partial \zeta} - = \frac{M_b}{2K\gamma^2\delta\left(1-M_b\right)^2}\frac{m}{r} J_m^2 e^{X_r\zeta}\left\{X_i \sin\left(X_i\zeta\right) - X_r\cos\left(X_i\zeta\right)\right\} \tag{4.68}$$

$$\frac{p^{(1)}}{\gamma}\frac{\partial u_\theta^{(1)}}{\partial t} = \frac{-1}{2\gamma^2\left(1-M_b\right)^2}\frac{m}{r} J_m^2 e^{X_r\zeta}\sin\left(X_i\zeta\right) \tag{4.69}$$

and

$$u_r^{(1)}\frac{u_\theta^{(1)}}{r} = 0; \quad u_r^{(1)}\frac{\partial u_\theta^{(1)}}{\partial r} = 0; \quad \frac{1}{\gamma r}\frac{\partial p^{(2)}}{\partial \theta} = 0; \quad \frac{u_\theta^{(1)}}{r}\frac{\partial u_\theta^{(1)}}{\partial \theta} = 0 \tag{4.70}$$

$$\frac{u_z^{(1)}}{\delta}\frac{\partial u_\theta^{(1)}}{\partial \zeta} = \frac{J_m^2 e^{X_r\zeta}}{2\gamma^2\left(1-M_b\right)^2}\left(\frac{m}{r}\right)\frac{\left(X_i^2 - X_r^2\right)}{X_i^2 + X_r^2}\left\{\sin\left(X_i\zeta\right) + \frac{2X_iX_r}{\left(X_i^2 - X_r^2\right)}\left[e^{X_r\zeta} - \cos\left(X_i\zeta\right)\right]\right\} \tag{4.71}$$

Equation (4.52) can now be rewritten as,

$$\frac{\partial^2 \boldsymbol{u}_\theta^{(2)}}{\partial \zeta^2} - \frac{M_b}{\delta}\frac{\partial \boldsymbol{u}_\theta^{(2)}}{\partial \zeta} = RHS(\theta) \tag{4.72}$$

with

$$RHS(\theta)=\frac{J_m^2 e^{2X_r\zeta}}{\gamma^2\left(1-M_b\right)^2}\frac{m}{r}\left\{\left(\frac{M_b}{2K\delta}-\frac{X_i}{X_i^2+X_r^2}\right)e^{-X_r\zeta}\left[X_i\sin\left(X_i\zeta\right)-X_r\cos\left(X_i\zeta\right)\right]-\frac{X_iX_r}{X_i^2+X_r^2}\right\}$$

(4.73)

Solution to the above equation is gained through normal means, giving

$$\begin{aligned}u_\theta^{(2)}=&\frac{m}{r}\frac{J_m^2\left[\left(X_i^2+X_r^2\right)M_b-2K\delta X_i\right]}{2K^2\gamma^2\beta_\theta\left(1-M_b\right)^2}\begin{Bmatrix}\left(M_b-\delta X_r\right)\left[e^{X_r\zeta}\cos\left(X_i\zeta\right)-1\right]\\-X_ie^{X_r\zeta}\sin\left(X_i\zeta\right)\end{Bmatrix}\\&+\frac{J_m^2\delta X_i}{2\gamma^2\left(1-M_b\right)^2\left(X_i^2+X_r^2\right)\left(2\delta X_r-M_b\right)}\frac{m}{r}\left(e^{2X_r\zeta}-1\right)\end{aligned}$$

(4.74)

with

$$\beta_\theta=\left(X_r{}^2+X_i{}^2\right)\left[\delta^2X_i^2+\left(M_b-\delta X_r\right)^2\right]$$

(4.75)

The axial component of velocity is best found through the use of the second order continuity equation (2.8).

$$\frac{\partial\rho^{(2)}}{\partial t}=-\nabla\cdot\boldsymbol{u}^{(2)}-\nabla\cdot\left[\rho^{(1)}\boldsymbol{u}^{(1)}\right]-M_b\nabla\cdot\left[\rho^{(2)}\boldsymbol{U}\right]$$

(4.76)

Using Eq. (3.31) this becomes,

$$\tfrac{1}{\gamma}p_t^{(2)}-\tfrac{\gamma-1}{2\gamma^2}\left[p^{(1)}\right]_t^2=-\nabla\cdot\boldsymbol{u}^{(2)}-\tfrac{1}{\gamma}\nabla\cdot\left[p^{(1)}\boldsymbol{u}^{(1)}\right]-M_b\nabla\cdot\left[\tfrac{1}{\gamma}p^{(2)}\boldsymbol{U}-\tfrac{\gamma-1}{2\gamma^2}\left[p^{(1)}\right]^2\boldsymbol{U}\right]$$

(4.77)

The above equation can be further simplified owing to the fact that the first and second order pressure solutions are not functions of z and that the mean flow in invariant. The simplified form of Eq. (4.77) is

$$\tfrac{1}{\gamma} p_t^{(2)} - \tfrac{\gamma-1}{2\gamma^2}\left[p^{(1)} \right]_t^2 = -\nabla \cdot \boldsymbol{u}^{(2)} - \tfrac{1}{\gamma} \nabla \cdot \left[p^{(1)} \boldsymbol{u}^{(1)} \right] \tag{4.78}$$

In terms of the boundary layer coordinate the above equation becomes,

$$\frac{\partial u_z^{(2)}}{\partial \zeta} = -\delta \left\{ \frac{\partial u_r^{(2)}}{\partial r} + \frac{u_r^{(2)}}{r} + \frac{1}{r} \frac{\partial u_\theta^{(2)}}{\partial \theta} + \frac{1}{\gamma} p_t^{(2)} - \frac{\gamma-1}{2\gamma^2}\left[p^{(1)} \right]_t^2 - \frac{1}{\gamma} \nabla \cdot \left[p^{(1)} \boldsymbol{u}^{(1)} \right] \right\} \tag{4.79}$$

The terms on the right-hand-side become,

$$\frac{1}{\gamma} p_t^{(2)} = 0; \;\; \frac{\gamma-1}{2\gamma^2}\left[p^{(1)} \right]_t^2 = 0; \;\; \frac{1}{r} \frac{\partial u_\theta^{(2)}}{\partial \theta} = 0 \tag{4.80}$$

$$-\frac{1}{\gamma} \nabla \cdot \left[p^{(1)} \boldsymbol{u}^{(1)} \right] = \frac{e^{X_r \zeta} \sin\left(X_i \zeta \right)}{2K\gamma^2 \left(1 - M_b \right)^2} \left(\delta K^2 J_m^2 + \frac{1}{r} J_m J_m' + J_m'^2 + J_m' J_m'' \right) \tag{4.81}$$

giving,

$$u_z^{(2)} = \int \delta \left\{ \frac{-\partial u_r^{(2)}}{\partial r} - \frac{u_r^{(2)}}{r} - \frac{e^{X_r \zeta} \sin\left(X_i \zeta \right)}{2K\gamma^2 \left(1 - M_b \right)^2} \left(\delta K^2 J_m^2 + \frac{1}{r} J_m J_m' + J_m'^2 + J_m' J_m'' \right) \right\} d\zeta \tag{4.82}$$

Integration leads to a formulation for the second-order axial fluctuations induced by transverse wave incidence with a liquid engine injector faceplate. At this point simplifications to the Bessel Function representation are made to conserve space.

$$u_z^{(2)} = \frac{-\frac{\delta}{r2K^2\gamma^2\left(1-M_b\right)^2}}{\left(X_r^{\,2}+X_i^{\,2}\right)}\left\{\begin{array}{l} \dfrac{\left(X_r^{\,2}+X_i^{\,2}\right)}{4X_r^{\,2}\left(2X_r-\frac{M_b}{\delta}\right)}\left[\begin{array}{l} \dfrac{2m^2}{r^3}J_m^2+r\left(\dfrac{m^2}{r^2}+K^2\dfrac{X_r^2-X_i^2}{X_r^2+X_i^2}\right)\left(J_m'^{\,2}+J_mJ_m''\right) \\ \left(K^2\dfrac{X_r^2-X_i^2}{X_r^2+X_i^2}-\dfrac{3m^2}{r^2}\right)J_mJ_m'+rJ_m''^{\,2}+rJ_m'J'''+J_m'J_m'' \end{array}\right]\left(e^{2X_r\zeta}-1\right) \\ +\left[\begin{array}{l} rX_r\left(\dfrac{\mathrm{d}\Lambda_{r,1}}{dr}+K^3\delta J_m^2+KJ_m'^2+KJ_m'J_m''\right) \\ +X_2^ir\left(\dfrac{\mathrm{d}\Lambda_{r,2}}{dr}+\dfrac{\Lambda_{r,2}}{r}\right)+X_r\left(\Lambda_{r,1}+KJ_mJ_m'\right) \end{array}\right]e^{X_r\zeta}\sin\left(X_i\zeta\right) \\ +\left[\begin{array}{l} X_r r\left(\dfrac{\mathrm{d}\Lambda_{r,2}}{dr}+\dfrac{\Lambda_{r,2}}{r}\right)-X_i\left(KJ_mJ_m'+\Lambda_{r,1}\right) \\ -X_i r\left(+K^3\delta J_m^2+KJ_m'^2+KJ_m'J_m''+\dfrac{\mathrm{d}\Lambda_{r,1}}{dr}\right) \end{array}\right]\left[e^{X_2^r\zeta}\cos\left(X_2^i\zeta\right)-1\right] \end{array}\right\} \tag{4.83}$$

In the above, the abbreviated function J_m stands for $J_m\left(k_{mn}r\right)$; its primes denote derivatives with respect to the radial coordinate. Having resolved the steady flowfield deep within the headwall boundary layer through Eqs. (4.64), (4.74) and (4.83), attention is now turned to the viscous flow's influence outside of the boundary layer. This effect is commonly referred to as "acoustic streaming." Unlike the first order viscous solution, which diminishes to the first order potential solution at the edge of the acoustic boundary layer, the effects of the second-order viscous flow are experienced throughout the entire chamber.

4.3. Streaming Analysis

It should be recalled that streaming flows are normally associated with a second-order steady rotational flow that is independent of viscous damping terms. To extract these

terms from the second-order flow solution, the limit is taken as the boundary layer coordinate approaches infinity. One obtains

$$\lim_{\zeta\to\infty} u_r^{(2)} = \frac{-\left[\left(\frac{m^2}{r^2}+K^2\frac{X_r^2-X_i^2}{X_r^2+X_i^2}\right)J_m J_m' - \frac{m^2}{r^3}J_m^2 + J_m' J_m''\right]}{4X_r\left(2X_r - M_b/\delta\right)\gamma^2K^2\left(1-M_b\right)^2} - \frac{\Lambda_{r,2}}{2K^2\gamma^2\left(1-M_b\right)^2} = \bar{u}_r^{(2)} \tag{4.84}$$

$$\lim_{\zeta\to\infty} u_\theta^{(2)} = \frac{-J_m^2}{2\gamma^2\left(1-M_b\right)^2}\frac{m}{r}\left\{\frac{\left(M_b-\delta X_r\right)}{2K^2\beta_\theta}\left[\left(X_i^2+X_r^2\right)M_b - 2K\delta X_i\right] - \frac{\delta X_i}{\left(X_i^2+X_r^2\right)}\right\} = \bar{u}_\theta^{(2)} \tag{4.85}$$

Reflected in Eqs. (4.84)and (4.85) is a second-order steady flow that is deprived of viscous damping terms. Streaming flow investigators often refer to solutions similar to these limiting expressions as second-order "potential" solutions, although they are not totally independent of viscosity.

Of interest is the comparison of the present investigation with other streaming solutions in similar geometries. A study performed by Yang and Flandro[44] allows for such comparison with little effort. Yang and Flandro considered the secondary flows generated in the geometry of a solid rocket motor with an inert head wall. The focus of the analysis lie in the representation of transverse wave interactions on a flat plate and the secondary flows induced within the boundary layer. To that extend the study does not satisfy the no through condition at the rocket sidewall. Taking the limit of Eqs. (4.84) and (4.85) as the injection parameter, $M_b/\delta \to 0$, leads to expressions that can be evaluated against those of Yang and Flandro; giving,

$$\lim_{M_b/\delta\to 0}\overline{u}_r^{(2)} = \frac{-1}{2K^2\gamma^2}\left[\frac{-J_m^2}{2K}\frac{m^2}{r^3} + \left(\frac{m}{r}\right)^2 J_m J_m' + J_m' J_m''\right] = \breve{u}_r^{(2)} \tag{4.86}$$

$$\lim_{M_b/\delta\to 0}\overline{u}_\theta^{(2)} = \frac{1}{4K\gamma^2}\left(\frac{m}{r}\right)J_m^2 = \breve{u}_\theta^{(2)} \tag{4.87}$$

Finally, to summarize the result obtained heretofore, Fig. 5 is used to delineate the main regions of interest and their pertinent solutions. For example, within the boundary layer region, the viscous treatment is most relevant. Applicable solutions include Eq. (4.38) for the first-order traveling wave solution and Eqs. (4.64)–(4.75) for the steady, second-order transverse velocities. In the outer region, the complete potential flow solution is depicted as the sum of the inviscid, irrotational, time-dependent field, given by Eqs. (3.28) and (3.76), and the viscous, rotational, steady streaming field given by Eqs. (4.84) and (4.85).

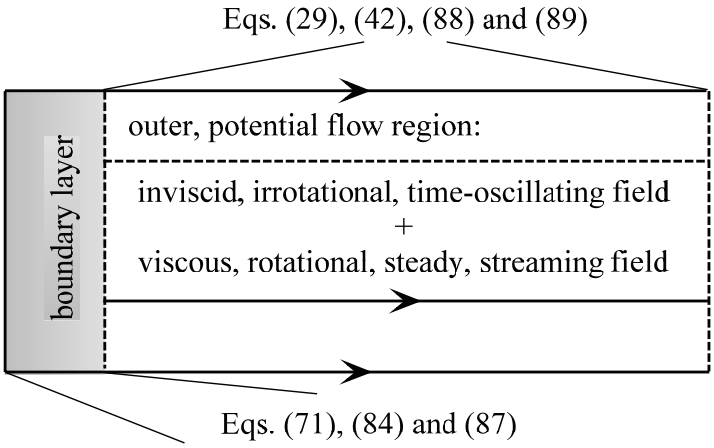
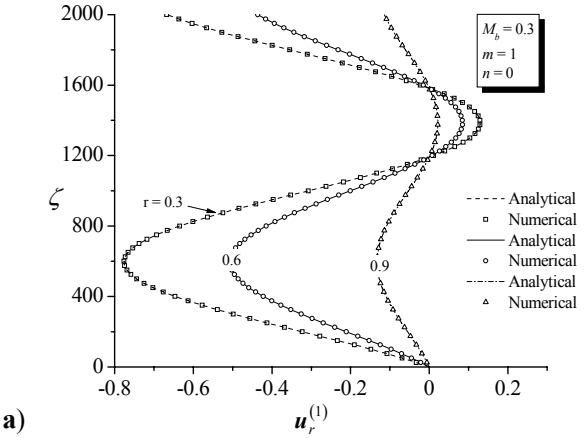


Figure 5. The main regions of interest are delineated along with their pertinent equations.

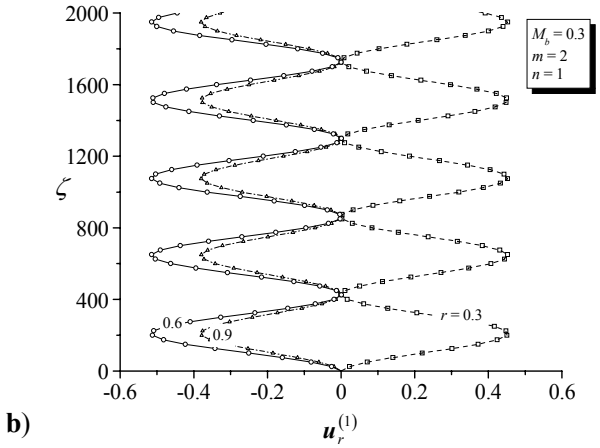
5. Results and Discussion

5.1. First Order Viscous Solution

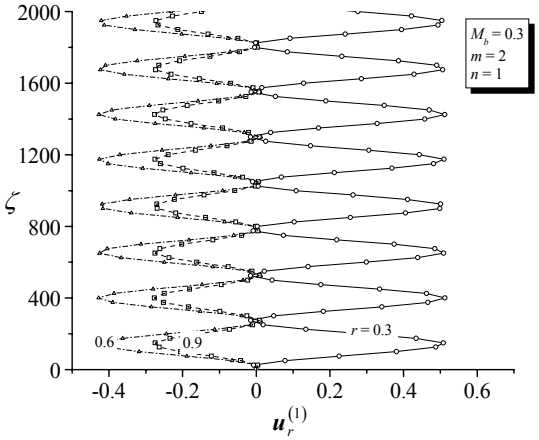
Before scrutinizing the resultant flow solutions for the first order viscous problem it is prudent to verify the analysis via a numerical prediction. To that end the boundary layer equations (Eq. (4.9)) are resolved using a numerical integrator and plotted along with their analytical counterpart. The nearly exact agreement of the radial and tangential velocities is demonstrated in Fig. 6 and 7 respectively. Figures 6 and 7 display the first-order boundary layer at $r = 0.3, 0.6, 0.9$, $\theta = \pi/3$, $M_b = 0.3$ and $\delta = 0.000647$ with the lines denoting the analytical solution and the symbols representing the numerical approximation. To illustrate the solution that was obtained, Fig. 8 is used to display the first-order boundary layer approximation for the traveling wave at $r = 0.4$, $\theta = \pi/3$, and $\delta = 0.000647$. The wave evolutions in the streamwise direction are shown at three headwall injection Mach numbers and the first spinning mode number $k_{10} \simeq 1.84118378$. The axial velocity fluctuation is not shown due to its small relative magnitude. It is apparent that the viscous stresses have a more pronounced effect as the injection Mach number is decreased. Conversely, when the injection Mach number is increased, the boundary layer is more effectively blown off the surface (see Cole and Aroesty[45] and Majdalani[37,40]). Furthermore, the propagation wavelength measured by the peak-to-peak distance decreases as the Mach number is lowered. In this case, the decay of the wave is also seen to be more rapid. Physically, this behavior may be attributed to the in-creased



a)

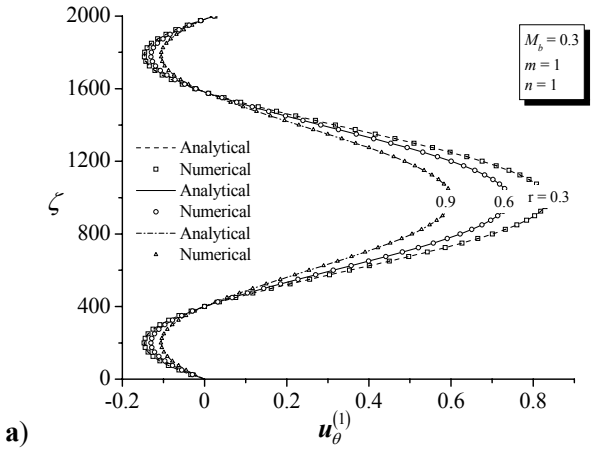


b)

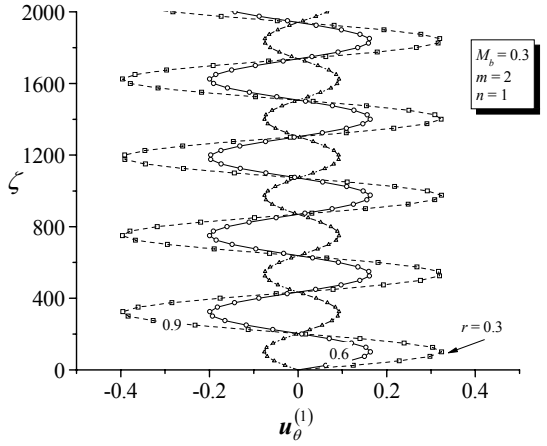


c)

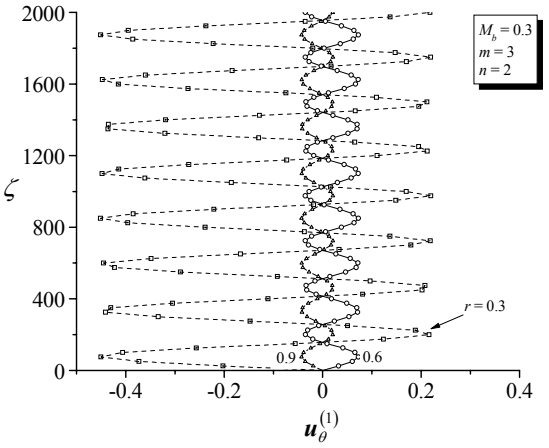
Figure 6. Comparison of the radial velocity approximation with numerical solution



a)

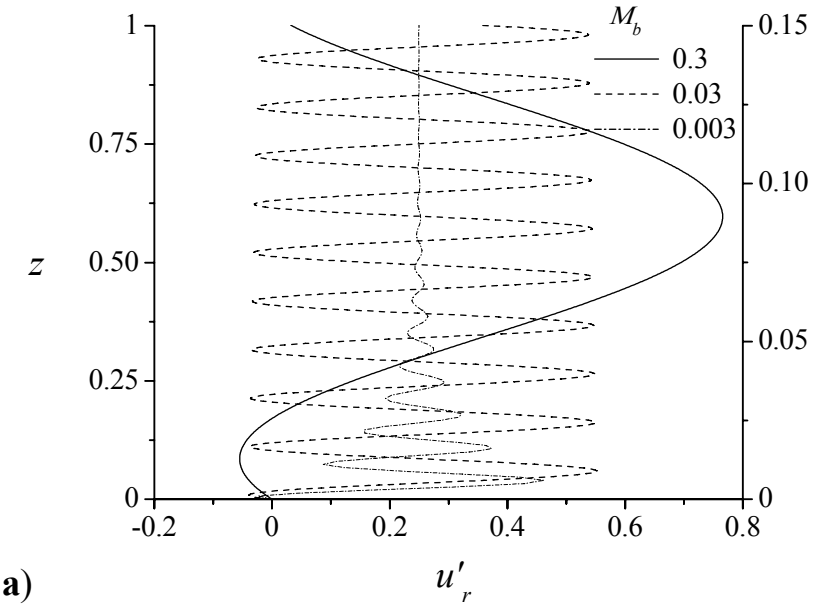


b)



c)

Figure 7. Numerical verification of first-order tangential velocity approximation



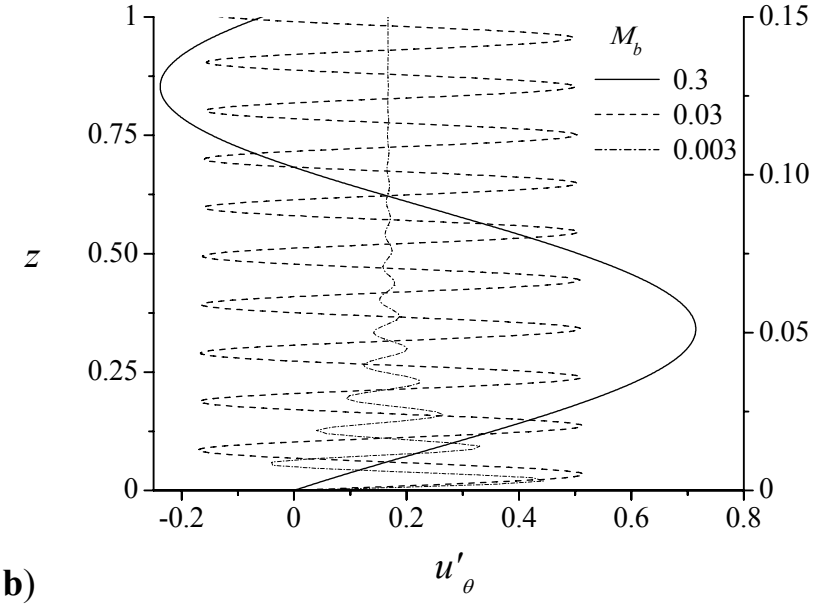


Figure 8. First-order approximations for a) radial and b) tangential velocities. The scale on the left-hand-side is for injection Mach numbers of 0.3 and 0.03. The scale on the right-hand-side is for M_b = 0.003.

dimensionless frequency, or Strouhal number, $S = K / M_b$. As the dimensionless frequency is increased (or the Mach number is decreased), the transverse fluctuations undergo a larger number of reversals per unit time. In the presence of viscosity, the higher frequency at which oscillations occur enhances the effects of fluid friction. Mathematically, the same behavior may be extrapolated from the dependence of the exponential decay terms on M_b. As one may infer from Eq. (4.39), increasing the Mach number leads to a smaller X_r and consequently, to a slower viscous damping in the axial direction. In actuality, the net damping is dominated by

$$\exp\left(X_r\zeta\right) \approx \exp\left(-\frac{\delta^2 K^2}{M_b^3} z\right) = \exp\left(-\frac{z}{S_p}\right) \tag{5.1}$$

where the effective penetration number S_p emerges in the form

$$S_p = \frac{M_b^3}{\delta^2 K^2} = \frac{V_b^3}{a_0^3}\frac{a_0 R}{\nu}\frac{a_0^2}{\omega_0^2 R^2} = \frac{V_b^3}{\nu\omega_0^2 R} \tag{5.2}$$

This parameter originated in the work by Majdalani,[37] and later appeared in studies by Flandro,[16] in the context of an oscillating longitudinal wave over an injecting surface in a porous cylinder. It was further explored in porous cylinders[38-41] and channels[46-49] with various injection patterns. An extremely detailed study of the penetration number can be found in the PhD dissertation of Majdalani[37] where multiple solutions to the acoustic boundary layer in a solid rocket motor are investigated. In the present study, a similar dimensionless group is found to control the depth of penetration of the headwall boun-

dary layer. This can be clearly seen by letting $\varphi = m\theta - Kt$ and recasting Eq. (4.38) into

$$\boldsymbol{u}^{(1)} = \frac{J_m(k_{mn}r)}{\gamma K(1-M_b)}\left(\frac{J'_m(k_{mn}r)}{J_m(k_{mn}r)}\left[\sin\varphi - \sin(\varphi+Sz)e^{-z/S_p}\right]\boldsymbol{e}_r + \frac{m}{r}\left[\cos\varphi - \cos(\varphi+Sz)e^{-z/S_p}\right]\boldsymbol{e}_\theta \right.$$
$$\left. + \frac{K^2}{S^2+S_p^2}\left\{S\cos\varphi - S_p\sin\varphi + \left[S_p\sin(\varphi+Sz) - S\cos(\varphi+Sz)\right]e^{-z/S_p}\right\}\boldsymbol{e}_z\right) \tag{5.3}$$

Note that as S_p is increased, a larger depth of penetration is realized. Conversely, for small penetration numbers, the exponential damping constant in Eq. (5.1) will be relatively large, leading to rapid spatial damping of the wave envelope and a shorter penetration depth. Physically, the penetration number unraveled here renders visible the balance between two co-existing forces: unsteady inertia and the viscous diffusion of the tangential (or radial) velocity in the axial direction. This dimensionless parameter reflects the ratio of

$$\frac{\text{unsteady inertial force}}{\text{viscous force}} \approx \frac{\dfrac{\partial u_\theta^*}{\partial t^*}}{\nu\dfrac{\partial^2 u_\theta^*}{\partial z^{*2}}} \approx \frac{\dfrac{\overline{u}_\theta^*}{\overline{t}^*}}{\nu\dfrac{\overline{u}_\theta^*}{\overline{z}^{*2}}} = \frac{\overline{z}^{*2}}{\nu\overline{t}^*} \approx \frac{(V_b/\omega_0)^2}{\nu(R/V_b)} = \frac{V_b^3}{\nu\omega_0^2 R} = S_p \tag{5.4}$$

In the above, we use $\overline{z}^* \approx V_b/\omega_0$ to represent the lengthscale of a wave of frequency ω_0 being convected at an axial speed that is proportional to V_b. We also take $\overline{t}^* \approx R/V_b$ to denote the timescale of a particle crossing the radius of the chamber at a characteristic speed equal to V_b. It is clear that the penetration number not only accounts for the influ-

ence of inertia and viscosity, but also embodies the effects of mean flow convection in the axial direction. The analogy with the former work on longitudinal waves is significant. While Majdalani and Flandro[41] considered an oscillating axial flow with steady radial mass flux at the porous sidewall, the present study addresses the motion of an oscillating transverse flow with steady axial flux at the headwall. By comparing these two problems, the blowing velocity V_b that appears in Eq. (5.2) will refer to either the transverse or axial mean flow values at the porous wall. The frequency of oscillation for a given mode shape will also be distinctly different, namely

$$\omega_0 = \begin{cases} \dfrac{k_{mn} a_0}{R} & \text{transverse wave} \\ m\dfrac{\pi a_0}{L} & \text{axial wave} \end{cases} \tag{5.5}$$

Aside from the blowing velocity and dimensional frequency, the remaining parameters in Eq. (5.2) are the same in both models. At the outset, a full characterization of the headwall boundary layer may be systematically carried out using the steps delineated before.[40]

5.1.1. Wave Characteristics

The establishment of the first-order boundary layer wave properties is useful in the elucidation of certain key parameters such as the penetration number, S_p and the Strouhal number, S. Determination of these key parameters' influence on the boundary layer thickness and therefore the rotational flow's area of influence give insight into patterns that will emerge in the rest of the study. The boundary layer thickness is commonly de-

fined as the point at which the rotational flow has decayed by 99%. Any area beyond the boundary layer thickness is therefore dominated by an irrotational acoustic profile. From Eq. (4.38) the rotational wave can be defined as

$$\boldsymbol{u}^{(1)}\left(\text{rotational}\right)=\frac{J_m\left(k_{mn}r\right)}{\gamma K\left(1-M_b\right)}\left\{\begin{aligned}&\frac{J_m'\left(k_{mn}r\right)}{J_m\left(k_{mn}r\right)}\left[\underbrace{-\sin\left(m\theta+X_i\,\zeta-Kt\right)}_{\text{wave propagation}}\underbrace{e^{X_r\zeta}}_{\text{decay}}\right]\boldsymbol{e}_r\\&+\left(\frac{m}{r}\right)\left[-\cos\left(m\theta+X_i\,\zeta-Kt\right)e^{X_r\zeta}\right]\boldsymbol{e}_\theta\\&+\frac{\delta K^2}{X_r^2+X_i^2}\left\{\begin{aligned}&X_r\left[-e^{X_r\zeta}\sin\left(m\theta+X_i\,\zeta-Kt\right)\right]\\&-X_i\left[-e^{X_r\zeta}\cos\left(m\theta+X_i\,\zeta-Kt\right)\right]\end{aligned}\right\}\boldsymbol{e}_z\end{aligned}\right. \tag{5.6}$$

Because the wave amplitude depends solely on $X_r\zeta$ a solution for the depth of penetration (boundary layer thickness) z_p can be easily defined as

$$z_p=\frac{\delta}{X_r}\ln\left(0.01\right) \tag{5.7}$$

As is demonstrated in Eq. (4.39) more physical insight is achieved through an asymptotic expression taking advantage of the smallness of parameters under the radical one gets,

$$z_p=\frac{\delta}{X_r}\ln\left(0.01\right)\approx -S_p\ln\left(0.01\right) \tag{5.8}$$

Figure 9 displays the depth of penetration for a wide range of kinetic Reynolds number, $\text{Re}_k=k_{mn}/\delta^2$, and Strouhal numbers. It is shown in Fig 9 how the depth of penetration rapidly decreases with an increase in S, demonstrating the amplified effect of

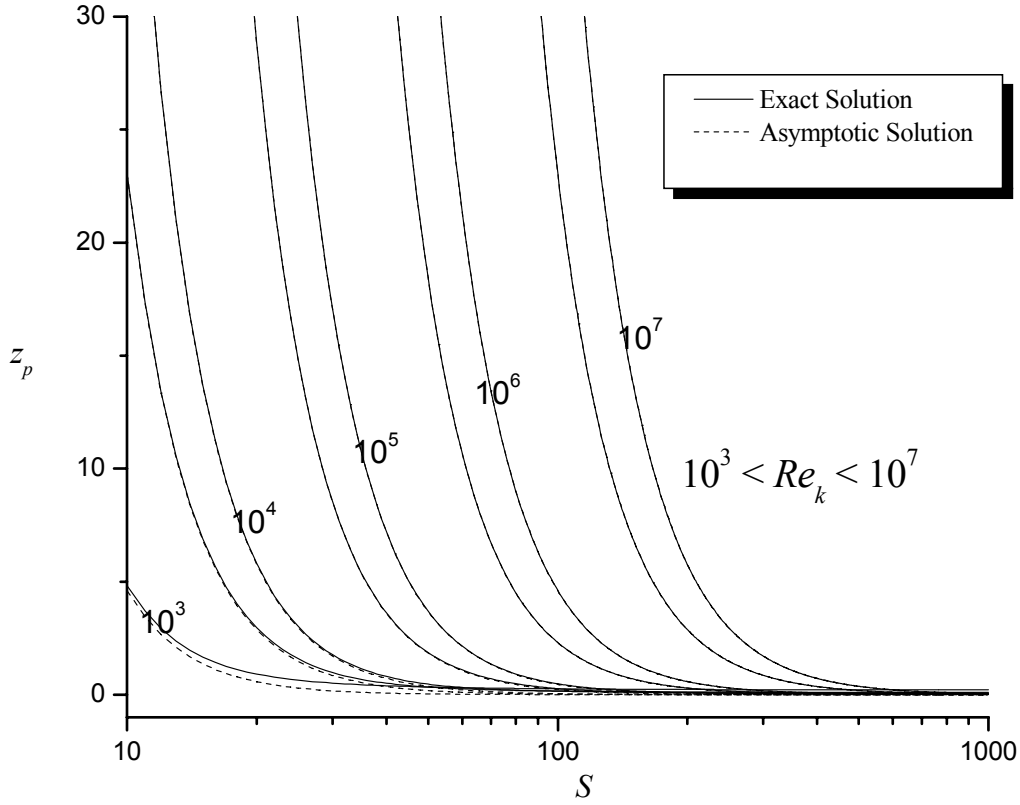


Figure 9. The depth of penetration, z_p, versus the Strouhal number,S, for increasing kinetic Reynolds number.

viscosity associated with a shorter wavelength. With a larger dimensionless frequency the flow experiences more reversals in a shorter distance as discussed in the previous section. Figure 9 also acts to display the amount of "blow off" that the head wall boundary layer experiences with an increased kinetic Reynolds number. As the headwall injection parameter, and therefore the Re_k, are increased the acoustic boundary layer is further removed from the head end, reducing its effect on the flow and increasing the boundary layer thickness. This result is different from those obtained by Majdalani[40] in the case of a solid rocket motor where the acoustic boundary layer thickness reaches an asymptotic maximum once the centerline is approached. In a solid rocket motor the mean flow field is mostly in the z-direction while the acoustic boundary layer appears in the radial direction.

Studies performed by Majdalani[38-41] demonstrated the importance of the penetration number in effectively displaying the acoustic boundary layer thickness. To effectively remove the influence of Re_k, one can express z_p as function of S_p. As shown in Fig. 10, the effect of the penetration number on the boundary layer thickness is clearly displayed and reflects the inverse proportionality of the damping exponential, X_r, and S_b. Figure 10 also demonstrates the range of applicability of the present investigation. With the main focus being in the realm of liquid injection engines the average injection Mach number lies in the range of $10^{-2} \le M_b \le 10^{-1}$. According to Eq. (5.2), in order to orient the penetration number into a range that is physically acceptable the dimensionless

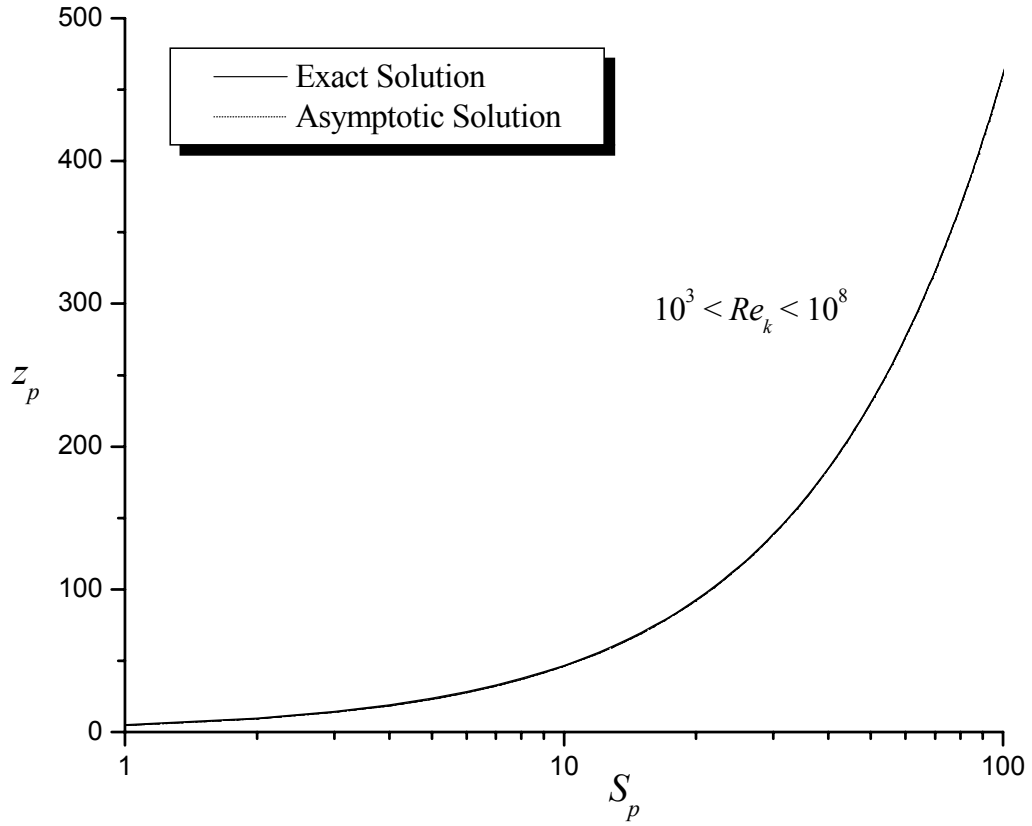


Figure 10. The depth of penetration, z_p, versus the penetration number, S_p, for increasing kinetic Reynolds number.

viscous parameter, δ, must balance the injection Mach number for various frequencies. Increasing viscosity in an area of highly chaotic flow is a technique to model turbulent effects without the use of complex CFD models.

5.1.2. Effect of Turbulence

Flandro, Cai and Yang[50] performed an extensive study of the effect of turbulent flow on the acoustic boundary layer in solid rocket motors. Their paper described an approximate technique for accounting for a turbulent mean flow through the coupling of realistic numerical simulations and detailed analytical approximations. A numerical simulation of the fully developed turbulent mean flow in a solid rocket chamber was performed and turbulent flow properties were extracted. The use of the turbulent flow properties, particularly the turbulent eddy viscosity, within the analytical model of the acoustic boundary layer in a solid rocket motor resulted in a significant reduction of the boundary layer thickness. The vortical waves that encompassed nearly the entire chamber in the laminar case were diminished to a thin sheet. The approximate method matched well with full unsteady numerical solution.

The study's results thoroughly demonstrate the influence of a turbulent mean flow on unsteady flows and rocket stability. Figure 11 displays the numerical values of the eddy viscosity for various locations along the motor length for the case of a typical tactical rocket. It is apparent that as the flow becomes more turbulent the eddy viscosity increases due to the increased flow interactions. The influence of increased eddy viscosity and turbulent mean flow on the vortical waves in the Shuttle Reusable Solid Rocket Motor is

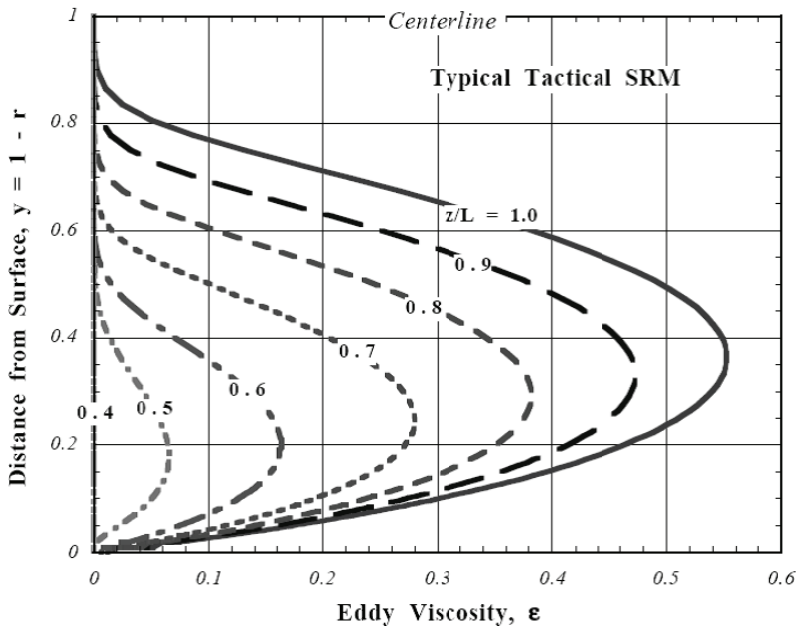


Figure 11. Eddy viscosity distribution in typical tactical rocket.[50]

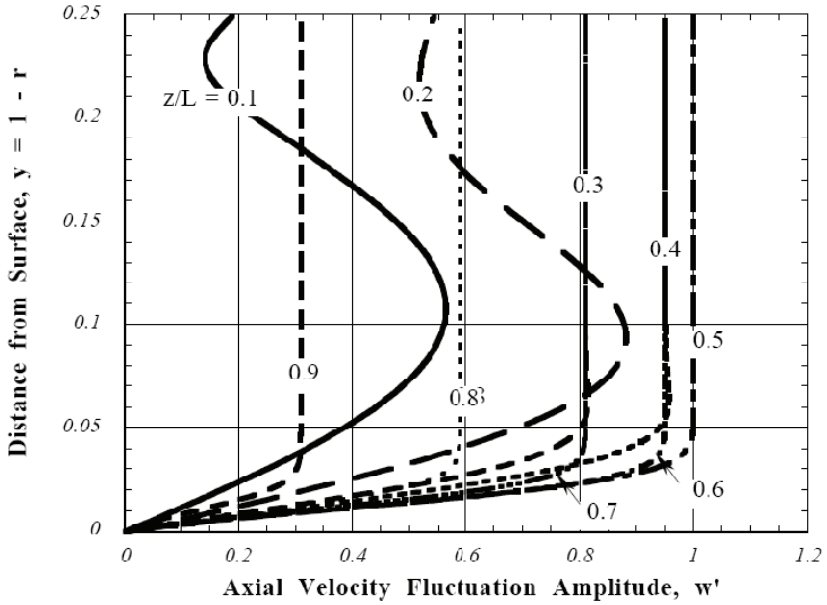


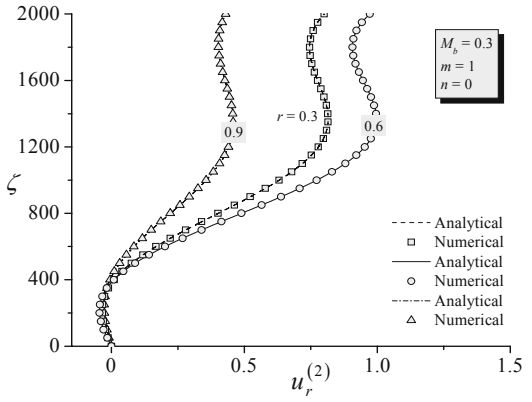
Figure 12 Effect of turbulence on axial wave amplitude (Shuttle SRM).[50]

displayed in Fig. 12. As the flow moves along the chamber length turbulence is naturally increased and the depth of penetration of the vortical waves is subsequently decreased.

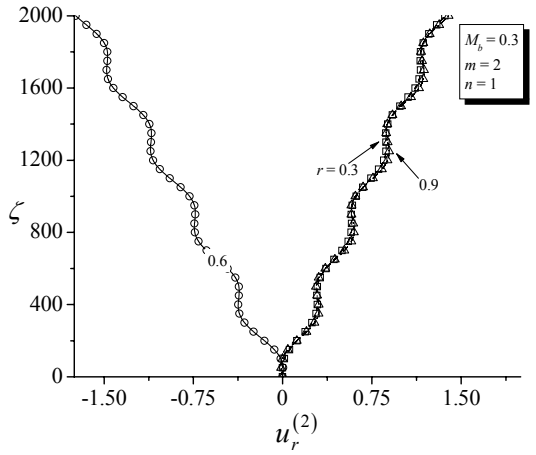
The analytical model utilized in the present studies makes no effort to account for a turbulent mean flow. It is apparent to the author that with the extensively complex injection processes found in non-idealized rocket engines an extremely turbulent flow will be realized very near to the injector faceplate. The focus of this study remaining on the acoustic streaming interactions, attention is now turned to the second-order solutions.

5.2. Second Order Viscous Solution

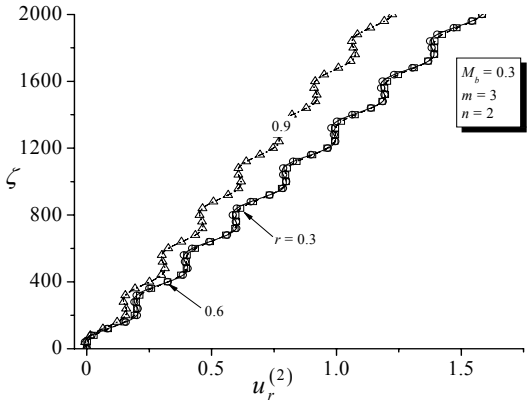
Figures 13 and 14 demonstrate the numerical solution to Eq. (4.52) along with the analytical formulas laid out above. Figures 13 and 14 display the second-order boundary layer at $r = 0.3, 0.6, 0.9$, $\theta = \pi/3$, $M_b = 0.3$ and $\delta = 0.000647$ with the lines denoting the analytical solution and the symbols representing the numerical approximation. Figure 15 displays the second-order radial and tangential velocities at $r = 0.4$, $\theta = \frac{1}{3}\pi$, and $\delta = 0.000647$ versus the axial coordinate at three headwall injection Mach numbers. The radial velocity exhibits an interesting trend displaying alternating spatial excursions that shift outwardly toward increasingly more positive values. This behavior is most apparent in the case of $M_b = 0.03$ (dashed line in Fig. 15a) where the radial velocity starts vacillating around $u_r \approx 0.25$ and then $u_r \approx 0.75$ in the short span of $z = [0,1]$. The same pattern is repeated in the cases of $M_b = 0.3$ and $M_b = 0.003,$ but the positively shifting excursions are masked in the corresponding graphs by the relative scales. These trends



a)

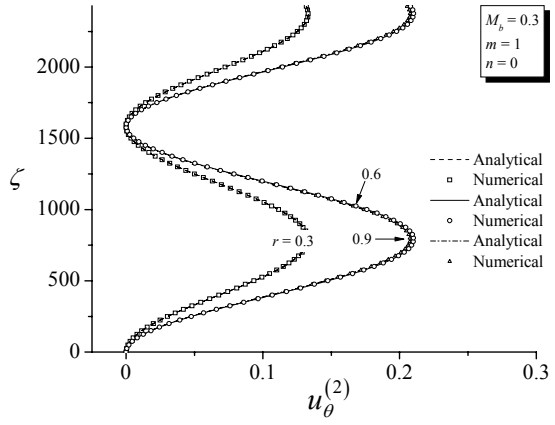


b)

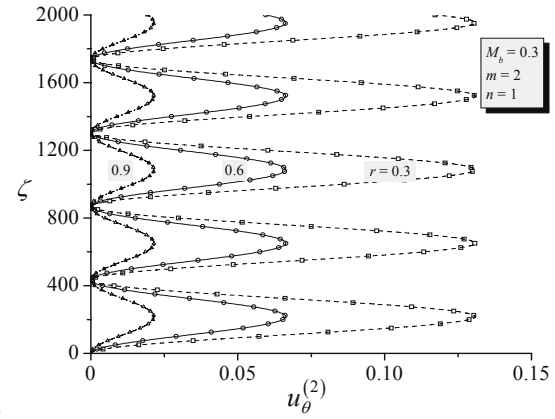


c)

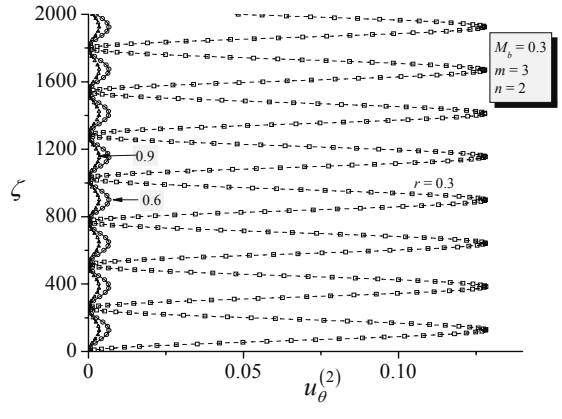
Figure 13. Numerical verification of second-order radial velocity.



a)

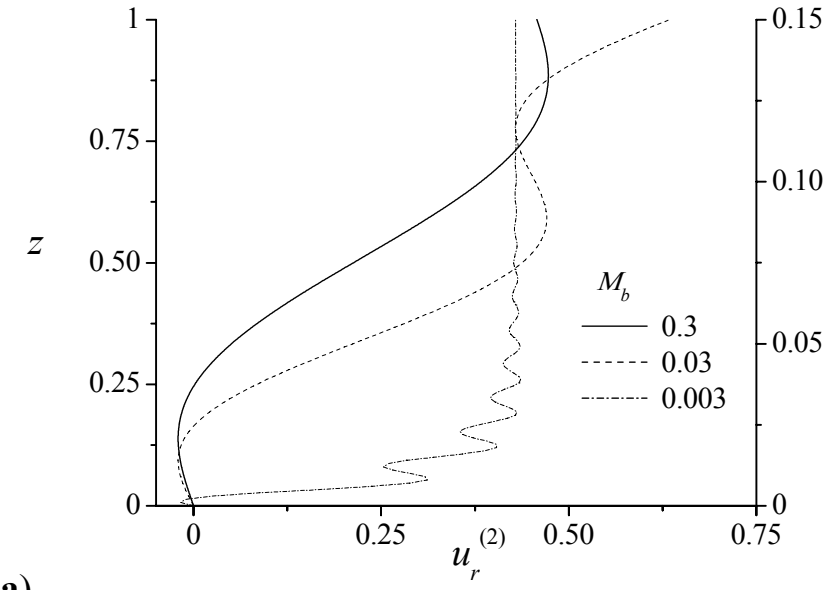


b)

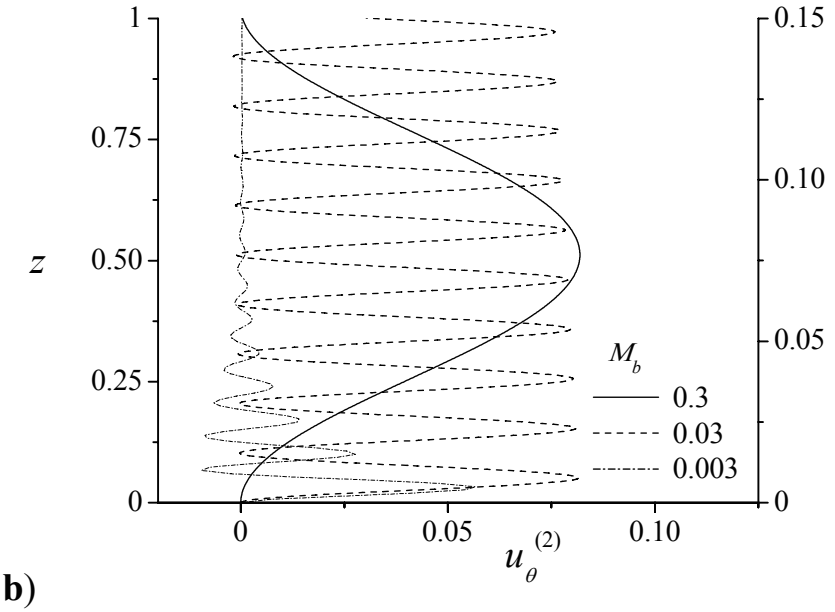


c)

Figure 14. Numerical verification of second-order steady tangential velocity.



a)

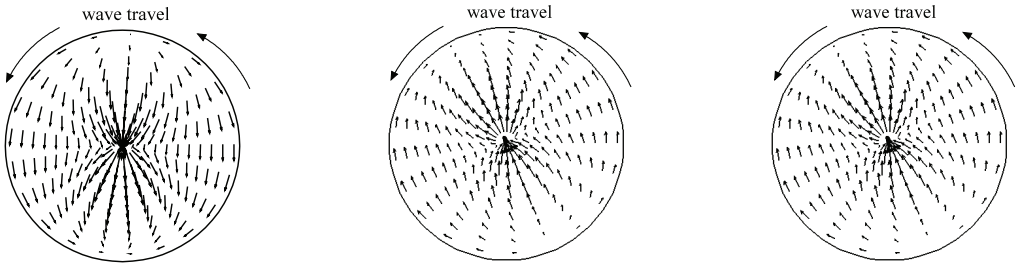


b)

Figure 15. Steady second-order approximations for a) radial and b) tangential velocities. The scale on the left-hand-side is for injection Mach numbers of 0.3. The scale on the right-hand-side is for M_b = 0.03 and 0.003.

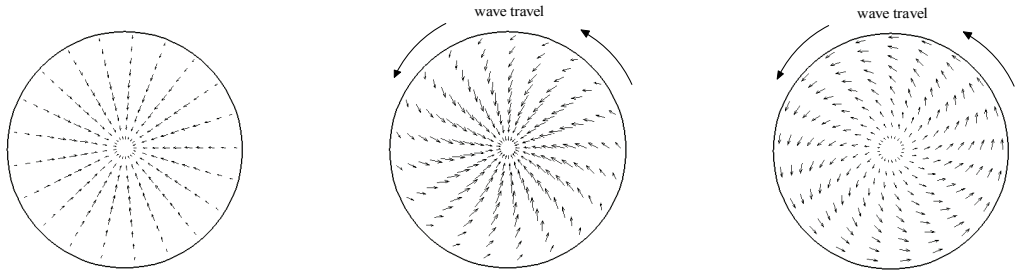
suggest that when fluid particles convect downstream, away from the injector face, the second-order flowfield becomes increasingly influenced by a steady radial velocity that pushes the fluctuations outwardly toward the sidewall.

In order to compare the first and second-order boundary layer flows, it may be useful to consider the entire wave structure in one particular instant of time. Figures 16 and 17 are snapshots of vector fields representing the first tangential mode of oscillation for the first and second-order solutions, respectively, taken at $z = 0.01, t = 1$ and $\delta = 0.00647$. In Fig. 17, only the steady portion of the second-order solution is shown. Note that the first-order solution in Fig. 16 spins in a counterclockwise fashion as a consequence of the convention assumed in the exponential time dependence. The vector traces shown here have comparable patterns that are merely reoriented in the polar plane with successive decreases in the headwall injection Mach number. Velocity vectors moving from one nodal point to the other are identified in all three plots. These patterns are in sharp contrast to the second-order results shown in Fig. 17, where the velocity vectors display distinctly dissimilar motions. In the cases of $M_b = 0.3$ and $0.03,$ the flow pattern is dominated by an inward pointing radial velocity drawing mass toward the chamber's centerline with a slight counterclockwise swirl velocity that is noticeable in the $M_b = 0.03$ case. At first glance, this pattern would appear to universally enhance the first-order motion whose wave structure rotates in a counterclockwise direction. A similar conclusion is reported by Flandro,[5] a closer examination of the flow behavior suggests the contrary effect is at work as well. Noting that the flow vectors of the first-order flow profile have a



a) **b)** **c)**

Figure 16. First-order traveling wave vector plot at z = 0.01 and three headwall injection Mach numbers of a) M_b = 0.3, b) 0.03, and c) 0.003.



a) **b)** **c)**

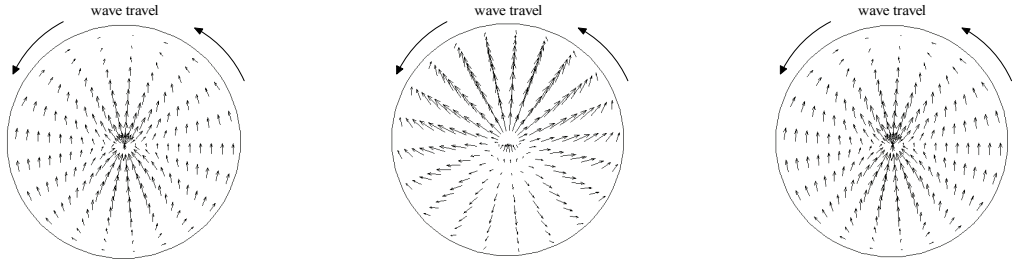
Figure 17. Steady second-order boundary layer velocity vector plot at z = 0.01 and three headwall injection Mach numbers of a) M_b = 0.3, b) 0.03, and c) 0.003.

negative (clockwise) $\theta-$component in one half of the region and positive (counter-clockwise) in the other half, it is seen that the second-order flow will diminish the $\theta-$component in half of the flow and increase it in the other. The same effect is seen in the case of the radial component as well. Note that Fig. 17c displays a strong outward pointing radial velocity with a similar counterclockwise swirl velocity. The disparity between Figs. 17a, 17b and 17c beckons a closer look at Fig. 8. In plotting the second-order radial component, it is seen that the velocity near the headwall fluctuates between positive and negative quantities. At $z=0.01$, deep within the boundary layer, the two larger injection Mach number cases are located in a negative u_r region, whereas the smallest Mach number case falls in a positive region. The corresponding arrowheads are inward pointing in Figs. 17a and 17b but outward in Fig. 17c. However, outside the boundary layer, the arrowheads are always outward pointing as corroborated by the outer limit for $u^{(2)}$, namely, the induced streaming solution.

5.3. Acoustic Streaming

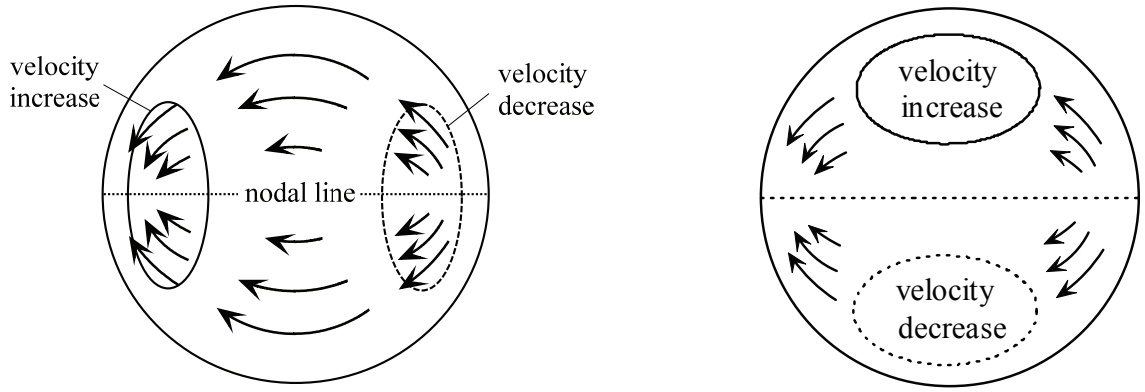
To illustrate the impact of the streaming solution restored in the outer limit, $\bar{u}_r^{(2)}$ and $\bar{u}_\theta^{(2)}$, on the total potential flow solution, Fig. 18 shows vector plots of the second-order approximation first without streaming (a), and then with streaming and either (b) $\delta=0.00647$ or (c) $\delta=0.0647$. All results are shown at $\varepsilon=0.1,\ M_b=0.3,\ t=0,\ m=1,$ and $n=0$ (first order tangential and zeroth order radial). Figure 19 is used as a pictorial representation of the streaming contributions. In Fig. 18a, only the total potential flow is depicted to second order. The results are found to be nearly identical to the first-order

potential solution and to the patterns in Fig. 16 where the first-order viscous solution is shown. This agreement reflects the diminutive nature of the second-order potential flow contribution. When streaming effects are accounted for, Figs. 18b and 18c bring into perspective the behavior of the total potential flow (to second order) combined with the streaming velocities, $\bar{u}_r^{(2)}$ and $\bar{u}_\theta^{(2)}$. It is quite evident in Fig. 18b that, when we use a typical value of $\delta = 0.00647,$ the streaming motion can markedly alter the fundamental flow structure observed in Figs. 16 and 18a. The velocity vectors are pushed outwardly in all directions with the effect being most pronounced in the area around the nodal line where the potential flow vectors are mostly radial. The flow patterns in Figs. 16 and 18a comprise two regions with respect to the axis of rotation, an upstream region where the flow is directed toward the core, and a downstream region where the flow is outward. With the superposition of the streaming correction in Fig. 18b, a reversal in the direction of flow upstream of the centerline may be noted. This flow reversal may be attributed to the large streaming amplitude resulting from the use of a relatively sizable $\varepsilon = 0.01$. In stark contrast to Fig. 18b, no streaming consequences may be linked to Fig. 18c, where the viscous parameter is increased to $\delta = 0.0647$. At first glance, the diminishment in streaming intensity with successive increases in δ appears to be paradoxical, or perhaps counterintuitive, because secondary flows are rooted deep within the viscous boundary layer. Upon further scrutiny, however, one realizes that increasing δ leads to a smaller penetration number as expressed through Eq. (5.2). Decreasing S_p reduces, in turn, the boundary layer thickness or depth of penetration of the rotational segment along which streaming is generated.



a) **b)** **c)**

Figure 18. Total vector plot in the outer region illustrating the behavior of a) the purely inviscid potential approximation up to the second order and b-c) the same total potential solution augmented by the streaming contribution. Results are shown for $t = 0$, $n = 1$, $\varepsilon = 0.01$, $M_b = 0.3$ and (a) $\delta = 0$, (b) 0.00647, and (c) 0.0647.

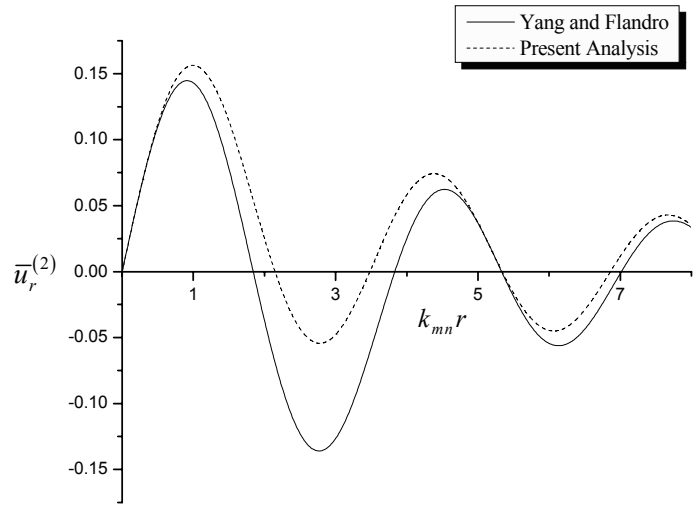


a) **b)**

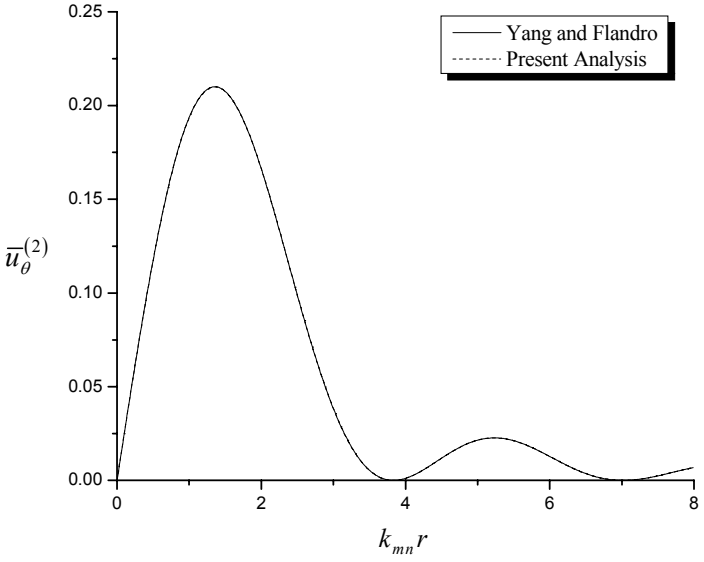
Figure 19. Sectors in which oscillatory waves are enhanced or weakened by virtue of streaming. These illustrate the outcome of interactions between a) radial and b) tangential velocities with the streaming motion

An analysis performed by Yang and Flandro[44] allow for an interesting comparison with the above results. Their analysis was that of secondary flows induced at a solid rocket motor nonreactive head-end. A comparison can be performed by taking the limit of the present analysis as the ratio of the injection Mach number and the dimensionless viscous parameter tend to zero, $M_b/\delta \to 0$. Figure 20 illustrates the similarity of the two solutions with Fig. 20a being the radial velocity and Fig. 20b being the tangential velocity. The above solution has to be recast into the variable used in the Yang and Flandro paper for ease of comparison; in reality the present investigation is only valid for $r < 1$. The relative velocity patterns show good coherence and give credibility to the present investigation.

Figure 20 is also useful in the determination of the injection Mach numbers' influence on the secondary flow amplitudes. Recalling from the above discussion, the streaming profile is dominated by the radial velocity and that the $\theta-$velocity is small in comparison. This is not the case when the injection at the head-end is turned off as is demonstrated by the present analysis and that of Yang and Flandro. Figure 20 demonstrates that the two velocities are of the same order of magnitude with $\bar{u}_\theta^{(2)}$ being greater than $\bar{u}_r^{(2)}$ in the area of interest, $k_{mn} r \le 1.84118378$. The creation of strong vortex structures along the chamber axis is often reported in solid rocket motors experiencing tangential wave combustion instability. These centralized vortex structures bring upon numerous problems including unexpected roll torques and intermittent nozzles blockage. The streaming profile presented here support the production of such structures and hints at a possible



a)



b)

Figure 20. Comparison of streaming velocities in the limit that $M_b/\delta \to 0$.

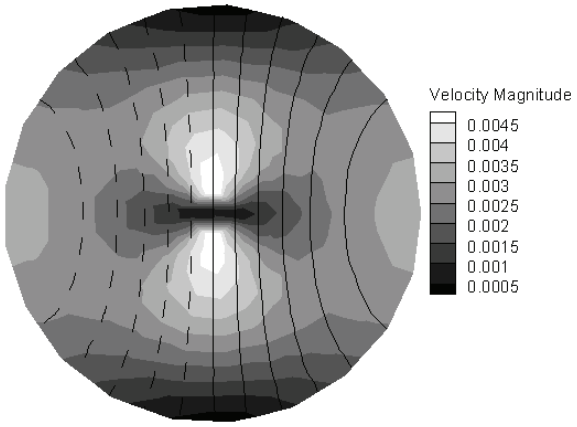
mitigation technique to such instability. As was observed above, the addition of mass transpiration at the rocket head-end decreases streaming in the $\theta-$direction. It is possible that the inclusion of a slow burning propellant at the motor head-end could reduce the occurrence of these strong central vortices.

In Fig. 19, two diagrams are provided to help visualize the key regions of interest. In Fig. 19a, we seek to isolate the coupling between streaming and radial waves. Being radially outward in all directions, streaming opposes the radial velocity waves in the right-hand-side sector of the domain, thus leading to a decreased local wave speed. By the same token, it enhances the radial wave in the left-hand-side sector, where it promotes further growth in the radial velocity. In Fig. 19b, the coupling with the tangential wave is examined. Given that streaming in the outer region is accompanied by small counterclockwise rotation (see Fig. 17c), its superposition on the counterclockwise motion of the tangential waves gives rise to regions with tangential velocity excess or defects, in the top and bottom halves of the domain, respectively. In practice, the coupling configurations shown in Figs. 19a and 19b occur simultaneously, thus leading to the patterns shown in Fig. 18b.

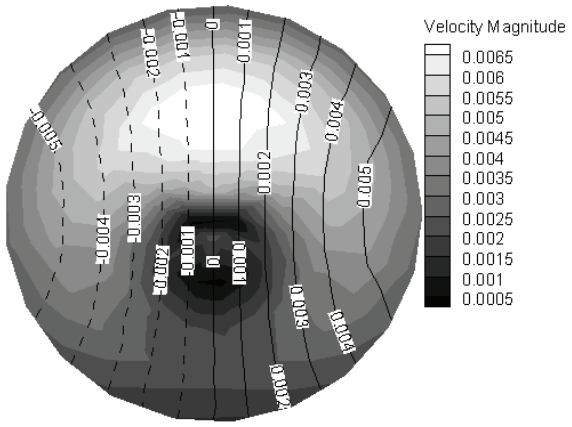
From the flow patterns depicted in Figs. 18 and 19, some interesting results may be inferred. Along the nodal pressure line (equator line in Fig. 18a), the flowfield is heavily dominated by radial velocities. Specifically, it is shown that along the nodal lines the flow is directed toward the center of the chamber on one side and out from the center on the other. Assuming that the velocity is proportional to the gradient of the pressure, a

conclusion about the corresponding wave form may be inferred. In Fig. 18, the region where the velocity vectors are counterclockwise corresponds to a positive pressure region with the peak amplitude occurring along the outer circumference. Conversely, in the region where the flow is clockwise (down below the nodal line), a negative pressure region is formed with the troughs occurring along the outer circumference as well. Along the nodal line, where the velocity vectors converge or diverge, a transition from a positive to a negative pressure region is realized. We note that the second-order streaming flow for a traveling wave is axisymmetric, with a strong outward pointing radial component. Therefore, in the case where the secondary flow is large enough to influence the first-order oscillations, the radial coupling along the nodal line is affected the most. In the absence of streaming, an observer situated at the north or south poles (Fig. 18a) will witness the largest tangential velocities sweeping by. In the presence of streaming, the flow will no longer be tangential as it gains an outward pointing radial component near the poles (Fig. 18b). Along the equator line, the potential flow that is originally radial will be either enhanced or weakened downstream and upstream of the core, respectively. The result is a steepened wave form similar to that described by Pierce[29] in the case of a plane wave. It should be noted that as per Fig. 8, the secondary flow is one order of magnitude smaller than $\boldsymbol{u}^{(1)}$. Recalling that the problem is linearized by the ratio of the pressure fluctuations to the mean pressure, ε, terms at the second order in ε are quite small. This will remain true until the peak-to-peak amplitudes of the pressure oscillations become comparable to the chamber pressure, as reported in Clayton's data[26] and other experimental measurements taken in liquid rockets.

Within the potential flow region where streaming effects are coupled with the inviscid flow profile the magnitude of the pressure gradient can be roughly represented by the magnitude of the velocity vector field. Figure 21 displays contour plots of the velocity magnitude to the second-order with and without streaming terms. On top of the velocity contours is plotted the contour lines of the pressure field to the second-order. Note that due to the linearization used in the perturbation analysis it is not possible to quantitatively establish the acoustic streaming's effect on the pressure field but qualitative results are inferred. In Fig. 21a the expected acoustic wave profile is displayed with symmetric contours demonstrating the sinusoidal transitions from pressure peak to trough. Conversely in Fig 21b a distinctly non-sinusoidal variation in the velocity magnitude is seen. In order to compare this result to those collected by Clayton, Sotter and co-workers,[1,26-28] (see Fig. 3) one must imagine oneself an observer situated at $\theta = 0$ where the pressure peak is located at $t = 0$. As time increases and the wave structure moves in a counterclockwise manner the observer will note a relatively small gradient in pressure (represented by a small velocity magnitude) while its amplitude drops from a peak to a trough. After the pressure trough has passed, the observer will experience a rapid increase in the pressure gradient. This is illustrated by the closely packed contour levels defining the velocity magnitude in the lighter region of the graph. The maximum pressure gradient is realized when the pressure contour line reaches zero. As the traveling wave continues to rotate the process is repeated with the observer seeing the same pattern again.



a)



b)

Figure 21. Velocity magnitude contours for a) second-order potential flow and b) second-order potential flow with streaming contributions.

6. Conclusions

The present investigation was concerned with the complex wave interactions that arise in a simulated liquid injection engine. An assumed constant unidirectional mean flow was utilized in the procurement of analytical solutions to the inviscid unsteady flowfield that was obtained to the second order in the wave amplitude, ε. Establishment of the viscous boundary layer profile to the second order was achieved through the use of the inviscid profile as an "outer" matching solution. As is common in this type of analysis the second order viscous analysis produced both steady and unsteady terms with the steady terms representing the well known "acoustic steaming" mechanism. Streaming terms induced in the viscous headwall flow propagate beyond the boundary layer into the potential field. It was established that for moderate levels of the wave amplitude the magnitude of induced streaming terms could alter the wave structure.

Acoustic streaming was shown to be made up of positive θ and radial components. When superimposed with the potential flow velocities the streaming terms act to increase the θ velocity in one half of the wave and to decrease it in the other. The effect was experienced with the radial components. This leads to the development of large amplitude peak to trough waves with a steepend wave front followed by a long shallow transition. Also, it was shown that the development of a strong vortex structure along the chamber axis was possible in the case of large amplitude waves like those recorded by Clayton *et al.*[26] Under such extreme conditions the present analysis broke down, thus suggesting the need for models.

References

References

[1]Clayton, R. M., Rogero, R. S., and Sotter, J. G., "An Experimental Description of Destructive Liquid Rocket Resonant Combustion," *AIAA Journal,* Vol. 6, No. 7, 1968, pp. 1252-1259.

[2]Culick, F. E. C., "High Frequency Oscillations in Liquid Rockets," *AIAA Journal,* Vol. 1, No. 5, 1963, pp. 1097-1104.

[3]Culick, F. E. C., "Acoustic Oscillations in Solid Propellant Rocket Chambers," *Acta Astronautica,* Vol. 12, No. 2, 1966, pp. 113-126.

[4]Flandro, G. A., "Theoretical Investigations of the Sergeant Roll Transient Problem," Sperry Utah Engineering Laboratory, Technical Rept. 211-SA-526C-61.14, Salt Lake City, April 1961.

[5]Flandro, G. A., "Rotating Flows in Acoustically Unstable Rocket Motors," Dissertation, California Institute of Technology, 1967.

[6]Flandro, G. A., Majdalani, J., and Sims, J. D., "Nonlinear Longitudinal Mode Instability in Liquid Propellant Rocket Engine Preburners," AIAA Paper 2004-4162, July 2004.

[7]Flandro, G. A., Majdalani, J., and Sims, J. D., "On Nonlinear Combustion Instability in Liquid Propellant Rocket Engines," AIAA Paper 2004-3516, July 2004.

[8]Flandro, G. A., and Sotter, J. G., "Unstable Combustion in Rockets," *Scientific American*, 1968.

[9]Hart, R. W., and McClure, F. T., "Combustion Instability: Acoustic Interaction with a Burning Propellant Surface," *The Journal of Chemical Physics,* Vol. 10, No. 6, 1959, pp. 1501-1514.

[10]Krier, H., T'ien, J. S., Sirignano, W. A., and Summerfield, M., "Nonsteady Burning Phenomena of Solid Propellants: Theory and Experiments," *AIAA Journal,* Vol. 6, No. 2, 1968, pp. 278-285.

[11]Maslen, S. H., and Moore, F. K., "On Strong Transverse Waves without Shocks in a Circular Cylinder," *Journal of the Aeronautical Sciences,* Vol. 23, 1956, pp. 583-593.

[12]Swithenbank, J., and Sotter, G., "Vortex Generation in Solid Propellant Rockets," *AIAA Journal,* Vol. 2, No. 7, 1964, pp. 1297-1302.

[13]Yang, V., Wicker, J., and Yoon, M. W., "Acoustic Waves in Combustion Chambers," *Liquid Rocket Engine Combustion Instability*, Vol. 169, edited by V. Yang and W. E. Anderson, AIAA Progress in Astronautics and Aeronautics, 1995, pp. 357-376.

[14]Hart, R. W., and McClure, F. T., "Theory of Acoustic Instability in Solid Propellant Rocket Combustion," *Tenth Symposium (International) on Combustion*, 1964, pp. 1047-1066.

[15]Culick, F. E. C., "Non-Linear Growth and Limiting Amplitude of Acoustic Oscillations in Combustion Chambers," *Combustion Science and Technology,* Vol. 3, No. 1, 1971, pp. 1-16.

[16]Flandro, G. A., "On Flow Turning," AIAA Paper 95-2530, July 1995.

[17]Fischbach, S. R., Majdalani, J., and Flandro, G. A., "Acoustic Instability of the Slab Rocket Motor," *Journal of Propulsion and Power,* Vol. 23, No. 1, 2007, pp. 146-157.

[18]Fischbach, S. R., Majdalani, J., and Flandro, G. A., "Verification and Validation of Rocket Stability Integral Transformations," AIAA Paper 2005-4001, July 2005.

[19]Fischbach, S. R., Majdalani, J., and Flandro, G. A., "Acoustic Instability of the Slab Rocket Motor," AIAA Paper 2004-4061, July 2004.

[20]Fischbach, S. R., Flandro, G. A., and Majdalani, J., "Volume-to-Surface Transformations of Rocket Stability Integrals," AIAA Paper 2004-4053, July 2004.

[21]Flandro, G. A., and Majdalani, J., "Aeroacoustic Instability in Rockets," *AIAA Journal,* Vol. 41, No. 3, 2003, pp. 485-497.

[22]Fabignon, Y., Dupays, J., Avalon, G., Vuillot, F., Lupoglazoff, N., Casalis, G., and Prévost, M., "Instabilities and Pressure Oscillations in Solid Rocket Motors," *Journal of Aerospace Science and Technology,* Vol. 7, No. 3, 2003, pp. 191-200.

[23]Ugurtas, B., Avalon, G., Lupoglazoff, N., Vuillot, F., and Casalis, G., "Stability and Acoustic Resonance of Internal Flows Generated by Side Injection," *Solid Propellant Chemistry, Combustion, and Motor Interior Ballistics*, Vol. 185, edited by V. Yang, T. B. Brill, and W.-Z. Ren, AIAA Progress in Astronautics and Aeronautics, Washington, DC, 2000, pp. 823-836.

[24]Oefelein, J. C., and Yang, V., "Comprehensive Review of Liquid-Propellant Combustion Instabilities in F-1 Engines," *Journal of Propulsion and Power,* Vol. 9, No. 5, 1993, pp. 657-677.

[25]Majdalani, J., Flandro, G. A., and Fischbach, S. R., "Some Rotational Corrections to the Acoustic Energy Equation in Injection-Driven Enclosures," *Physics of Fluids,* Vol. 17, No. n 17, 2005, p. 074102.

[26]Clayton, R. M., "Experimental Measurements on Rotating Detonation-Like Combustion," JPL, Technical Rept. 32-788, Pasadena, CA, August 1965.

[27]Sotter, J. G., Woodward, J. W., and Clayton, R. M., "Injector Response to Strong High-Frequency Pressure Oscillations," *Journal of Spacecraft and Rockets,* Vol. 6, No. 4, 1969, pp. 504-506.

[28]Sotter, J. G., and Clayton, R. M., "Monitoring the Combustion Process in Large Engines," *Journal of Spacecraft and Rockets,* Vol. 4, No. 5, 1967, pp. 702-703.

[29]Pierce, A. D., *Acoustics, an Introduction to Its Physical Principles and Applications*, Acoustical Society of America, New York, 1989.

[30]Farraday, M., "On a Peculiar Class of Acoustical Figures; and on Certain Forms Assumed by Groups of Paricles Upon Vibrating Elastic Surfaces," *Philosophical Transactions of the Royal Society of London,* Vol. 121, 1831.

[31]Andrade, E. N., "On the Circulations Caused by the Vibration of Air in a Tube," *Proc. of the Royal Society of London,* Vol. 134, 1931.

[32]Schlichting, H., *Boundary-Layer Theory*, 7th ed., McGraw-Hill, New York, 1979.

[33]Rayleigh, J. W. S., *Theory of Sound*, Dover, New York, 1954.

[34]Westervelt, P. J., "The Theory of Steady Rotational Flow Generated by a Sound Field," *The Journal Of The Acoustical Society Of America,* Vol. 25, No. 1, 1953, pp. 60-67.

[35]Nyborg, W. L., "Acoustic Streaming Due to Attenuated Plane Waves," *The Journal Of The Acoustical Society Of America,* Vol. 25, No. 1, 1953, pp. 68-75.

[36]Schlichting, H., "Berechnung Ebener Periodischer Grenzschichtstroemungen," *Physikalische Zeitschrift,* Vol. 33, 1932, pp. 327-335.

[37]Majdalani, J., "Improved Flowfield Models in Rocket Motors and the Stokes Layer with Sidewall Injection," Ph.D. Dissertation, University of Utah, 1995.

[38]Majdalani, J., "Characterization of the Laminar Boundary Layer in Solid Rocket Motors," AIAA Paper 98-3699, July 1998.

[39]Majdalani, J., and Van Moorhem, W. K., "Improved Time-Dependent Flowfield Solution for Solid Rocket Motors," *AIAA Journal,* Vol. 36, No. 2, 1998, pp. 241-248.

[40]Majdalani, J., "The Boundary Layer Structure in Cylindrical Rocket Motors," *AIAA Journal,* Vol. 37, No. 4, 1999, pp. 505-508.

[41]Majdalani, J., and Flandro, G. A., "The Oscillatory Pipe Flow with Arbitrary Wall Injection," *Proceedings of the Royal Society, Series A,* Vol. 458, No. 2022, 2002, pp. 1621-1651.

[42]Jankowski, T. A., and Majdalani, J., "Vortical and Acoustical Mode Coupling inside a Porous Tube with Uniform Wall Suction," *Journal of the Acoustical Society of America,* Vol. 117, No. 6, 2005, pp. 3448-3458.

[43]Majdalani, J., and Vyas, A. B., "Inviscid Models of the Classic Hybrid Rocket," AIAA Paper 2004-3474, July 2004.

[44]Yang, J. Y. S., and Flandro, G. A., "Head-End Secondary Flows in Solid -Propellant Rockets Due to Transverse Acoustic Waves," *AIAA Journal* Vol. 9, No. 6, 1971, pp. 11-251129.

[45]Cole, J. D., and Aroesty, J., "The Blowhard Problem-Inviscid Flows with Surface Injection," *International Journal of Heat and Mass Transfer,* Vol. 11, No. 7, 1968, pp. 1167-1183.

[46]Majdalani, J., "A Hybrid Multiple Scale Procedure for Boundary Layers Involving Several Dissimilar Scales," *Journal of Applied Mathematics and Physics,* Vol. 49, No. 6, 1998, pp. 849-868.

[47]Majdalani, J., "Asymptotic Formulation for an Acoustically Driven Field inside a Rectangular Cavity with a Well-Defined Convective Mean Flow Motion," *Journal of Sound and Vibration,* Vol. 223, No. 1, 1999, pp. 73-95.

[48]Majdalani, J., and Roh, T. S., "The Oscillatory Channel Flow with Large Wall Injection," *Proceedings of the Royal Society, Series A,* Vol. 456, No. 1999, 2000, pp. 1625-1657.

[49]Majdalani, J., "The Oscillatory Channel Flow with Arbitrary Wall Injection," *Journal of Applied Mathematics and Physics,* Vol. 52, No. 1, 2001, pp. 33-61.

[50]Flandro, G. A., Cai, W., and Yang, V., "Turbulent Transport in Rocket Motor Unsteady Flowfield," *Solid Propellant Chemistry, Combustion, and Motor Interior Ballistics*, Vol. 185, edited by V. Yang, T. B. Brill, and W.-Z. Ren, AIAA Progress in Astronautics and Aeronautics, Washington, DC, 2000, pp. 837-858.

Appendix

Appendix

In this section standing wave solutions are given for the first and second order potential field along with the first and second order boundary layer approximations. Testing performed on actual motors demonstrate that either traveling or standing waves may appear during firings. To date no universally accepted theory pertaining to the physical mechanisms that causes an engine to establish one wave form over the other. Therefore, the inclusion of standing waves to this analysis is pertinent and practical.

A.1. First Order Potential Flow

Focusing on radial and tangential waves, the first order pressure profile for a standing wave can be written as

$$p^{(1,0)} = \cos(m\theta)\cos(Kt)J_m(k_{mn}r) \tag{A.1}$$

Using Eq. (3.18) the order ε velocity profile becomes,

$$\boldsymbol{u}^{(1,0)} = \begin{bmatrix} \frac{1}{\gamma K}\cos(m\theta)\sin(Kt)J'_m(k_{mn}r)\boldsymbol{e_r} \\ -\frac{1}{\gamma K}\left(\frac{m}{r}\right)\sin(m\theta)\sin(Kt)J_m(k_{mn}r)\boldsymbol{e}_\theta \\ +(0)\boldsymbol{e}_z \end{bmatrix} \tag{A.2}$$

Through similar steps to those outlined in the traveling wave case, the total first-order profile becomes

$$\begin{cases} \boldsymbol{u}^{(1)} = \left(\sum_{j=0}^{\infty} M_b^j \right) \boldsymbol{u}^{(1,0)} = \dfrac{1}{1-M_b} \boldsymbol{u}^{(1,0)} \\ p^{(1)} = \left(\sum_{j=0}^{\infty} M_b^j \right) p^{(1,0)} = \dfrac{1}{1-M_b} p^{(1,0)} = \dfrac{J_m\left(k_{mn} r\right)}{1-M_b} \cos\left(m\theta\right) \cos\left(Kt\right) \end{cases} \tag{A.3}$$

A.2. Second Order Potential Flow

Due to the extensive use of baffle as a trial and error fix to liquid engine instabilities the oscillations may be more accurately represented by a standing wave as opposed to a traveling wave. The conversion of traveling waves into standing waves is fairly straightforward but one can find difficulties when dealing with quadratic groupings of trigonometric functions. For this reason the standing wave solutions for the second-order flow profile will be derived in this section. Starting with the second order wave equation for the previous section, the analysis can be redone with standing waves. As before the wave equation is expanded in terms of the injection mach number:

$$\begin{aligned} &\nabla^2 p^{(2,0)} - p_{tt}^{(2,0)} = \frac{1-\gamma}{2\gamma} \left\{ \left[p^{(1,0)} \right]^2 \right\}_{tt} + \nabla \cdot p_t^{(1,0)} \boldsymbol{u}^{(1,0)} - \gamma \frac{\nabla^2}{2} \left[\boldsymbol{u}^{(1,0)} \cdot \boldsymbol{u}^{(1,0)} \right] \\ &\boldsymbol{n} \cdot \nabla p^{(2,0)} \Big|_{z=0} = 0; \quad \boldsymbol{n} \cdot \nabla p^{(2,0)} \Big|_{r=1} = 0 \end{aligned} \tag{A.4}$$

$$\begin{aligned} \nabla^2 p^{(2,1)} - p_{tt}^{(2,1)} = {} & \frac{1-\gamma}{\gamma} \left[p^{(1,0)} p^{(1,1)} \right]_{tt} + \nabla \cdot \left[p_t^{(1,1)} \boldsymbol{u}^{(1,0)} + p_t^{(1,0)} \boldsymbol{u}^{(1,1)} \right] - \gamma \nabla^2 \left[\boldsymbol{u}^{(1,0)} \cdot \boldsymbol{u}^{(1,1)} \right] \\ & + \left[\nabla \cdot p^{(2,0)} U \right]_t - \gamma \nabla \cdot \left\{ \nabla \left[\boldsymbol{U} \cdot \boldsymbol{u}^{(2,0)} \right] - \boldsymbol{U} \times \boldsymbol{w}^{(2,0)} \right\} \\ \boldsymbol{n} \cdot \nabla p^{(2,1)} \Big|_{z=0} = 0; \quad & \boldsymbol{n} \cdot \nabla p^{(2,1)} \Big|_{r=1} = 0 \end{aligned} \tag{A.5}$$

$$\nabla^2 p^{(2,2)} - p_{tt}{}^{(2,2)} = \frac{1-\gamma}{2\gamma}\left\{2p^{(1,0)}p^{(1,2)} + \left[p^{(1,1)}\right]^2\right\}_{tt} + \nabla\cdot\left[p_t^{(1,1)}\boldsymbol{u}^{(1,1)} + p_t^{(1,2)}\boldsymbol{u}^{(1,0)} + p_t^{(1,0)}\boldsymbol{u}^{(1,2)}\right]$$
$$-\gamma\frac{\nabla^2}{2}\left[2\boldsymbol{u}^{(1,0)}\cdot\boldsymbol{u}^{(1,2)} + \boldsymbol{u}^{(1,1)}\cdot\boldsymbol{u}^{(1,1)}\right] + \left[\nabla\cdot p^{(2,1)}U\right]_t - \gamma\nabla\cdot\left\{\nabla\left[\boldsymbol{U}\cdot\boldsymbol{u}^{(2,1)}\right] - \boldsymbol{U}\times\boldsymbol{w}^{(2,1)}\right\}$$
$$\boldsymbol{n}\cdot\nabla p^{(2,2)}\Big|_{z=0} = 0; \quad \boldsymbol{n}\cdot\nabla p^{(2,2)}\Big|_{r=1} = 0$$

(A.6)

The first order flowfield is used to evaluate the right-hand-side of Eq. (3.35) producing, for the standing wave case

$$\nabla^2 p^{(2,0)} - p_{tt}{}^{(2,0)} = F(r) + G(r)\cos(2m\theta) + B(r)\cos(2Kt) + C(r)\cos(2Kt)\cos(2m\theta) \qquad \text{(A.7)}$$

containing the four radial dependent functions

$$F(r) = \frac{1}{4\gamma K^2}\left\{\begin{array}{l}\left(\frac{3m^2}{r^3} - \frac{K^2}{r}\right)J_m(k_{mn}r)J'_m(k_{mn}r) - \left(K^2 + \frac{m^2}{r^2}\right)J'^2_m(k_{mn}r)\\ -\left(K^2 + \frac{m^2}{r^2}\right)J_m(k_{mn}r)J''_m(k_{mn}r) - \frac{1}{r}J'_m(k_{mn}r)J''_m(k_{mn}r)\\ -J''^2_m(k_{mn}r) - J'_m(k_{mn}r)J'''_m(k_{mn}r) - 2\frac{m^2}{r^4}J^2_m(k_{mn}r)\end{array}\right\} \qquad \text{(A.8)}$$

and,

$$G(r) = \frac{1}{4\gamma K^2}\left\{\begin{array}{l}-\left(\frac{5m^2}{r^3} + \frac{K^2}{r}\right)J_m(k_{mn}r)J'_m(k_{mn}r) + \left(\frac{3m^2}{r^2} - K^2\right)J'^2_m(k_{mn}r)\\ -\left(K^2 + \frac{m^2}{r^2}\right)J_m(k_{mn}r)J''_m(k_{mn}r) - \frac{1}{r}J'_m(k_{mn}r)J''_m(k_{mn}r)\\ -J''^2_m(k_{mn}r) - J'_m(k_{mn}r)J'''_m(k_{mn}r) + 2\frac{m^2}{r^4}J^2_m(k_{mn}r)\end{array}\right\} \qquad \text{(A.9)}$$

$$B(r)=\frac{1}{4\gamma K^2}\left\{\begin{array}{l}\left[K^4(\gamma-1)+\frac{m^2}{r^4}\right]2J_m^2(k_{mn}r)+J_m''^2(k_{mn}r)+J_m'(k_{mn}r)J_m'''(k_{mn}r)\\+\left(\frac{K^2}{r}-\frac{3m^2}{r^3}\right)J_m(k_{mn}r)J_m'(k_{mn}r)+\left(K^2+\frac{m^2}{r^2}\right)J_m'^2(k_{mn}r)\\+\left(K^2+\frac{m^2}{r^2}\right)J_m(k_{mn}r)J_m''(k_{mn}r)+\frac{J_m'(k_{mn}r)J_m''(k_{mn}r)}{r}\end{array}\right\} \quad (A.10)$$

with,

$$C(r)=\frac{1}{4\gamma K^2}\left\{\begin{array}{l}\left[K^4(\gamma-1)-\frac{m^2}{r^4}\right]2J_m^2(k_{mn}r)+J_m''^2(k_{mn}r)+J_m'(k_{mn}r)J_m'''(k_{mn}r)\\+\left(\frac{K^2}{r}+\frac{5m^2}{r^3}\right)J_m(k_{mn}r)J_m'(k_{mn}r)+\left(K^2-\frac{3m^2}{r^2}\right)J_m'^2(k_{mn}r)\\+\left(K^2+\frac{m^2}{r^2}\right)J_m(k_{mn}r)J_m''(k_{mn}r)+\frac{J_m'(k_{mn}r)J_m''(k_{mn}r)}{r}\end{array}\right\} \quad (A.11)$$

From the right-hand-side of Eq. (3.38) it is apparent that the second order pressure will be made up of steady and unsteady parts. These separate parts will be identified as the steady and oscillating parts

$$p^{(2,0)}=p_{st}^{(2,0)}+p_{os}^{(2,0)} \quad (A.12)$$

The particular solution to Eq. (3.38) is

$$p_p^{(2,0)}=H(r)+I(r)\cos(2m\theta)+D(r)\cos(2Kt)+E(r)\cos(2Kt)\cos(2m\theta) \quad (A.13)$$

$$H(r)=-\tfrac{1}{8\gamma K^2}\left\{\left[\left(\tfrac{m}{r}\right)^2+K^2\right]J_m(k_{mn}r)^2+J_m'(k_{mn}r)^2\right\} \quad (A.14)$$

$$I(r) = -\frac{1}{8\gamma K^2}\left\{\left[K^2 - \left(\frac{m}{r}\right)^2\right] J_m\left(k_{mn}r\right)^2 + J_m'\left(k_{mn}r\right)^2\right\} \tag{A.15}$$

$$\begin{aligned} D(r) &= \frac{1}{2\gamma K^2}\left\{\left[\frac{1}{4}\left(\frac{m}{r}\right)^2 + \frac{1}{4}K^2\right] J_m\left(k_{mn}r\right)^2 + \frac{1}{4}J_m'\left(k_{mn}r\right)^2 + K^4(\gamma - 1)g(r)\right\} \\ s/t \;&\mapsto\; g'' + \frac{1}{r}g' + 4K^2 g = J_m\left(k_{mn}r\right)^2 \end{aligned} \tag{A.16}$$

$$\begin{aligned} E(r) &= \frac{1}{2\gamma K^2}\left\{-\left[\frac{1}{4}\left(\frac{m}{r}\right)^2 - \frac{1}{4}K^2\right] J_m\left(k_{mn}r\right)^2 + \frac{1}{4}J_m'\left(k_{mn}r\right)^2 + K^4(\gamma - 1)f(r)\right\} \\ s/t \;&\mapsto\; f'' + \frac{1}{r}f' + 4\left(K^2 - \frac{m^2}{r^2}\right) f = J_m\left(k_{mn}r\right)^2 \end{aligned} \tag{A.17}$$

with the homogenous solution being of the form of the first order solution, specifically

$$p_H^{(2,0)} = \cos(m\theta)\cos(Kt) J_m\left(k_{mn}r\right) \tag{A.18}$$

We are only interested in the steady part of the second order solution.

$$p_{st}^{(2,0)} = H(r) + I(r)\cos(2m\theta) \tag{A.19}$$

As was done in the case of the traveling wave it is important to establish the second order velocity profile for a standing wave. Beginning with Eq. (3.53) the velocity profile is solved using normal techniques. Giving, in the radial direction,

$$\begin{aligned} \left[u_r^{(2,0)}\right]_t = \frac{1}{2\gamma^2}\cos(2Kt) &\left\{\begin{array}{l} \cos(2m\theta)\left[-J_m\left(k_{mn}\right)J_m'\left(k_{mn}r\right) + (1-\gamma)K^2 f'(r)\right] \\ +\left[-J_m\left(k_{mn}\right)J_m'\left(k_{mn}r\right) + (1-\gamma)K^4 g'(r)\right] \end{array}\right\} \\ &-\frac{1}{\gamma}\cos(Kt)\cos(m\theta)J_m'\left(k_{mn}r\right) \end{aligned} \tag{A.20}$$

and so

$$u_r^{(2,0)} = \frac{1}{4K\gamma^2}\sin(2Kt)\begin{Bmatrix}\cos(2m\theta)\left[-J_m(k_{mn})J'_m(k_{mn}r)+(1-\gamma)K^2 f'(r)\right]\\ +\left[-J_m(k_{mn})J'_m(k_{mn}r)+(1-\gamma)K^2 g'(r)\right]\end{Bmatrix} \\ -\tfrac{1}{\gamma K}\sin(Kt)\cos(m\theta)J'_m(k_{mn}r) \tag{A.21}$$

with the azimuthal component being

$$u_\theta^{(2,0)} = \tfrac{1}{4\gamma^2 K}\left(\tfrac{m}{r}\right)\sin(2Kt)\sin(2m\theta)\left[-J_m(k_{mn})^2+2(\gamma-1)K^2 f(r)\right] \\ +\tfrac{1}{\gamma K}\left(\tfrac{m}{r}\right)\sin(Kt)\sin(m\theta)J_m(k_{mn}r) \tag{A.22}$$

The expression for the second order unsteady pressure can be written in a general form with respect to the $p^{(2,0)}$ term:

$$p^{(2)} = p^{(2,0)} + \sum_{n=1}^{\infty} M_b^n\left[(n+1)\,p_p^{(2,0)} + p_H^{(2,0)}\right] \tag{A.23}$$

Moreover, the expression for the second order unsteady velocity can be written in a general form with respect to the $\boldsymbol{u}^{(2,0)}$ term.

$$\boldsymbol{u}^{(2)} = \boldsymbol{u}^{(2,0)} + \sum_{n=1}^{\infty} M_b^n\left[(n+1)\,\boldsymbol{u}_p^{(2,0)} + \boldsymbol{u}_H^{(2,0)}\right] \tag{A.24}$$

A.3. First Order Boundary Layer Flow

The standing wave counterpart for the first-order boundary layer approximation is written as

$$\boldsymbol{u}^{(1)}=\begin{Bmatrix}\frac{1}{\gamma K}J'_m\left(k_{mn}r\right)\sin\left(Kt\right)\left[\cos\left(m\theta\right)-\cos\left(m\theta\right)\cos\left(X_2^i\zeta\right)e^{X_2^r\zeta}\right]\boldsymbol{e}_r\\ \frac{1}{\gamma K}\left(\frac{m}{r}\right)J_m\left(k_{mn}r\right)\sin\left(Kt\right)\left[\sin\left(m\theta\right)\cos\left(X_2^i\zeta\right)e^{X_2^r\zeta}-\sin\left(m\theta\right)\right]\boldsymbol{e}_\theta\\ \frac{\delta K}{\gamma}\left(\frac{J_m\left(k_{mn}r\right)}{X_2^{i2}+X_2^{r2}}\right)\sin\left(Kt\right)X_2^r\left[\cos\left(m\theta\right)\cos\left(X_2^i\zeta\right)e^{X_2^r\zeta}-\cos\left(m\theta\right)\right]+\\ \frac{\delta K}{\gamma}\left(\frac{J_m\left(k_{mn}r\right)}{X_2^{i2}+X_2^{r2}}\right)\sin\left(Kt\right)X_2^i\left[\cos\left(m\theta\right)\sin\left(X_2^i\zeta\right)e^{X_2^r\zeta}\right]\boldsymbol{e}_z\end{Bmatrix} \tag{A.25}$$

A.4. Second Order Boundary Layer Flow

First focusing on the traveling wave in the radial direction the terms on the right-hand-side can be evaluated giving,

$$\frac{1}{\gamma}\frac{\partial p^{(2)}}{\partial r}=\frac{-2}{\left[2K\gamma\left(1-M_b\right)\right]^2}\left\{\sin\left(m\theta\right)^2\frac{m^2}{r^3}\left(J_{mm}^2-rJ_mJ'_m\right)-\cos\left(m\theta\right)^2\left[K^2+J'_mJ''_m\right]\right\} \tag{A.26}$$

$$\frac{M_b}{\delta}\frac{p^{(1)}}{\gamma}\frac{\partial u_r^{(1)}}{\partial\zeta}=0 \tag{A.27}$$

$$\frac{p^{(1)}}{\gamma}\frac{\partial u_r^{(1)}}{\partial t}=\frac{1}{2\gamma^2\left(1-M_b\right)^2}J_mJ'_m\cos\left(m\theta\right)^2\left[1-e^{X_r\zeta}\cos\left(X_i\zeta\right)\right] \tag{A.28}$$

$$-u_\theta^{(1)}\frac{u_\theta^{(1)}}{r}=\frac{-1}{2\gamma^2K^2\left(1-M_b\right)^2}\left(\frac{m^2}{r^3}\right)J_m^2\left[1-2e^{X_2^r\zeta}\cos\left(X_i\zeta\right)+e^{2X_r\zeta}\cos\left(X_i\zeta\right)^2\sin\left(m\theta\right)^2\right] \tag{A.29}$$

$$\frac{u_\theta^{(1)}}{r}\frac{\partial u_r^{(1)}}{\partial\theta}=\frac{-J_mJ'_m}{2\gamma^2K^2\left(1-M_b\right)^2}\left(\frac{m}{r}\right)^2\left[1-2e^{X_2^r\zeta}\cos\left(X_2^i\zeta\right)+e^{2X_2^r\zeta}\cos\left(X_2^i\zeta\right)^2\sin\left(m\theta\right)^2\right] \tag{A.30}$$

$$\frac{u_z^{(1)}}{\delta}\frac{\partial u_r^{(1)}}{\partial\zeta}=\frac{1}{2\gamma^2\left(1-M_b\right)^2}J_mJ'_m\cos\left(m\theta\right)^2\begin{bmatrix}X_i^2e^{2X_r\zeta}\sin\left(X_i\zeta\right)^2-X_iX_re^{X_r\zeta}\sin\left(X_i\zeta\right)\\ +X_r^2e^{X_r\zeta}\cos\left(X_i\zeta\right)-X_r^2e^{2X_r\zeta}\cos\left(X_i\zeta\right)^2\end{bmatrix} \tag{A.31}$$

$$u_r^{(1)}\frac{\partial u_r^{(1)}}{\partial r}=\frac{1}{K^2\gamma^2\left(1-M_b\right)^2}J'_mJ''_m\cos\left(m\theta\right)^2\left[1-e^{X_r\zeta}\cos\left(X_i\zeta\right)+e^{2X_r\zeta}\cos\left(X_i\zeta\right)^2\right] \quad \text{(A.32)}$$

Equation (4.52) can now be rewritten as,

$$\frac{\partial^2\boldsymbol{u}_r^{(2)}}{\partial\zeta^2}-\frac{M_b}{\delta}\frac{\partial u_r^{(2)}}{\partial\zeta}=\text{RHS} \quad \text{(A.33)}$$

Since the focus of this study is on the steady flow the term involving the partial derivative with respect to time has been removed.

$$\text{RHS}=\frac{e^{X_r\zeta}}{2K^2\gamma^2\left(1-M_b\right)^2}\left(\begin{array}{l}\sin\left(X_i\zeta\right)\cos\left(m\theta\right)^2J_mJ'_m\frac{K^2X_i}{\left(X_r^2+X_i^2\right)}\left[X_ie^{X_r\zeta}\sin\left(X_i\right)-X_r\right]\\+\cos\left(X_i\zeta\right)\left\{\begin{array}{l}\cos\left(m\theta\right)^2\left[\left(-K^2+\frac{K^2X_r^2}{\left(X_r^2+X_i^2\right)}\right)J_mJ'_m-2J'_mJ''\right]\\+\sin\left(m\theta\right)^2\left[\frac{2m^2}{r^3}\left(J_m^2-rJ_mJ'_m\right)\right]\end{array}\right.\\+e^{X_r\zeta}\cos\left(X_i\right)^2\left\{\begin{array}{l}\cos\left(m\theta\right)^2\left[\frac{K^2X_r^2}{\left(X_r^2+X_i^2\right)}J_mJ'_m+J'_mJ''\right]\\-\sin\left(m\theta\right)^2\left[\frac{m^2}{r^3}\left(J_m^2-rJ_mJ'_m\right)\right]\end{array}\right.\end{array}\right) \quad \text{(A.34)}$$

Solution to the above equation is gained straightforward. One gets

$$u_r^{(2)}=\frac{1}{2K^2\gamma^2\left(1-M_b\right)^2}\left\{\begin{array}{l}\left[e^{X_r\zeta}\cos\left(X_i\zeta\right)-1\right]\Gamma_{r,1}+e^{X_r\zeta}\sin\left(X_i\zeta\right)\Gamma_{r,2}+\left[e^{2X_r\zeta}-1\right]\Gamma_{r,3}\\+\left[e^{2X_r\zeta}\cos\left(2X_i\zeta\right)-1\right]\Gamma_{r,4}+e^{2X_r\zeta}\sin\left(2X_i\zeta\right)\Gamma_{r,5}\end{array}\right\} \quad \text{(A.35)}$$

$$\Gamma_{r,1}=\frac{1}{\beta_r}\left\{\begin{array}{l}\sin\left(m\theta\right)^2\frac{2m^2}{r^3}\left[\delta X_i^2+X_r\left(M_b-\delta X_r\right)\right]\left\{-J_m^2+rJ_mJ'_m\right\}\\+\cos\left(m\theta\right)^2\left\{\delta X_i^2K^2J_mJ'_m+2\left[\delta X_i^2+X_r\left(M_b-\delta X_r\right)\right]J'_mJ''_m\right\}\end{array}\right\} \quad \text{(A.36)}$$

$$\Gamma_{r,2} = \frac{1}{\beta_r}\left\{\begin{array}{l} \sin\left(m\theta\right)^2 \dfrac{2m^2}{r^3}\left[X_i\left(M_b - 2\delta X_r\right)\right]\left\{J_m^2 - rJ_mJ'_m\right\} \\ +\cos\left(m\theta\right)^2 X_i\left(\delta X_r - M_b\right)\left\{K^2 J_m J'_m - 2J'_m J''_m\right\} \end{array}\right\} \tag{A.37}$$

and

$$\Gamma_{r,3} = \frac{\delta}{4X_r\left(2\delta X_r - M_b\right)}\left\{\begin{array}{l} \sin\left(m\theta\right)^2 \dfrac{m^2}{r^3}\left\{-J_m^2 + rJ_mJ'_m\right\} \\ +\cos\left(m\theta\right)^2\left(K^2 J_m J'_m + J'_m J''_m\right) \end{array}\right\} \tag{A.38}$$

$$\Gamma_{r,4} = \frac{X_i\delta\left(4\delta X_r - M_b\right)}{4\beta_r}\left\{\begin{array}{l} \cos\left(m\theta\right)^2\left\{K^2\left(1 - \dfrac{2X_i^2}{\left(X_r^2 + X_i^2\right)}\right)J_mJ'_m + J'_mJ''_m\right\} \\ +\sin\left(m\theta\right)^2 \dfrac{m^2}{r^3}\left\{-J_m^2 + rJ_mJ'_m\right\} \end{array}\right\} \tag{A.39}$$

Finally, one can put,

$$\Gamma_{r,5} = \frac{X_r\delta\left(2\delta X_r - M_b\right) - 2\delta X_i^2}{4\beta_r}\left\{\begin{array}{l} \cos\left(m\theta\right)^2\left\{K^2\left(1 - \dfrac{2X_i^2}{\left(X_r^2 + X_i^2\right)}\right)J_mJ'_m + J'_mJ''_m\right\} \\ +\sin\left(m\theta\right)^2 \dfrac{m^2}{r^3}\left\{-J_m^2 + rJ_mJ'_m\right\} \end{array}\right\} \tag{A.40}$$

$$\beta_r = \left(X_r^2 + X_i^2\right)\left[\delta^2 X_i^2 + \left(M_b - \delta X_r\right)^2\right] \tag{A.41}$$

Note that the limitations of the analysis discussed during the derivation of the first order boundary layer solution appear in the second order solution as well. Specifically we see that the radial velocity does not vanish at the chamber sidewall. This is a direct result of the square of the azimuthal velocity on the right-hand-side of Eq. (4.52). Next our atten-

tion is turned to the right-hand-side terms of the second order azimuthal velocity, giving

$$u_r^{(1)}\frac{u_\theta^{(1)}}{r}=\frac{\sin\left(2m\theta\right)}{\left[2K\gamma\left(1-M_b\right)\right]^2}\frac{m}{r^2}J_mJ'_m\left[-1+2e^{X_r\zeta}\cos\left(X_i\zeta\right)-e^{2X_r\zeta}\cos\left(X_i\zeta\right)^2\right] \quad \text{(A.42)}$$

$$u_r\frac{\partial u_\theta^{(1)}}{\partial r}=\frac{\left(J_mJ'_m-rJ'^2_m\right)}{\left[2K\gamma\left(1-M_b\right)\right]^2}\sin\left(2m\theta\right)\frac{m}{r^2}\left[1-2e^{X_r\zeta}\cos\left(X_i\zeta\right)+e^{2X_r\zeta}\cos\left(X_i\zeta\right)^2\right] \quad \text{(A.43)}$$

$$\frac{p^{(1)}}{\gamma}\frac{\partial u_\theta^{(1)}}{\partial t}=\frac{-1}{\left[2\gamma\left(1-M_b\right)\right]^2}\left(\frac{m}{r}\right)J_m^2\sin\left(2m\theta\right)\left[e^{X_r\zeta}\cos\left(X_i\zeta\right)-1\right] \quad \text{(A.44)}$$

$$\frac{1}{\gamma r}\frac{\partial p^{(2)}}{\partial\theta}=\frac{-1}{\left[2K\gamma\left(1-M_b\right)\right]^2}\sin\left(2m\theta\right)\left(\frac{m}{r}\right)\left[\left(K^2-\tfrac{m^2}{r^2}\right)J_m^2+J'^2_m\right] \quad \text{(A.45)}$$

$$\frac{u_\theta^{(1)}}{r}\frac{\partial u_\theta^{(1)}}{\partial\theta}=\frac{\sin\left(2m\theta\right)}{\left[2K\gamma\left(1-M_b\right)\right]^2}J_m^2\left(\frac{m}{r}\right)^3\left[1-2e^{X_r\zeta}\cos\left(X_i\zeta\right)+e^{2X_r\zeta}\cos\left(X_i\zeta\right)^2\right] \quad \text{(A.46)}$$

$$\frac{M_b}{\gamma\delta}p^{(1)}\frac{\partial u_\theta^{(1)}}{\partial\zeta}=0 \quad \text{(A.47)}$$

$$\frac{u_z^{(1)}}{\delta}\frac{\partial u_\theta^{(1)}}{\partial\zeta}=\frac{mJ_m^2\sin\left(2m\theta\right)}{r\left({X_r}^2+{X_i}^2\right)\left[2\gamma\left(1-M_b\right)\right]^2}\begin{bmatrix}-e^{2X_r\zeta}\sin\left(X_i\zeta\right)^2{X_i}^2+e^{2X_r\zeta}\cos\left(X_i\zeta\right)^2{X_r}^2\\+e^{X_r\zeta}\sin\left(X_i\zeta\right)X_iX_r-e^{X_r\zeta}\cos\left(X_i\zeta\right){X_r}^2\end{bmatrix} \quad \text{(A.48)}$$

Equation (4.52) can now be rewritten as,

$$\frac{\partial^2\boldsymbol{u}_\theta^{(2)}}{\partial\zeta^2}-\frac{M_b}{\delta}\frac{\partial\boldsymbol{u}_\theta^{(2)}}{\partial\zeta}=\mathrm{RHS}\left(\theta\right) \quad \text{(A.49)}$$

with,

$$\mathrm{RHS}(\theta)=\frac{\sin(2m\theta)}{\left[2K\gamma(1-M_b)\right]^2}\frac{m}{r}\left(\begin{array}{l} e^{X_r\zeta}\sin(X_i\zeta)\frac{K^2X_i}{(X_r{}^2+X_i{}^2)}J_m^2\left[X_r-X_ie^{X_r\zeta}\sin(X_i)\right] \\ +e^{X_r\zeta}\cos(X_i\zeta)\left[\left(K^2-\frac{2m^2}{r^2}-\frac{K^2X_r{}^2}{(X_r{}^2+X_i{}^2)}\right)J_m^2+J_m'{}^2\right] \\ +e^{2X_r\zeta}\cos(X_2^i)^2\left[\left(\frac{m^2}{r^3}+\frac{K^2X_r{}^2}{(X_r{}^2+X_i{}^2)}\right)J_m^2-J_m'{}^2\right] \end{array}\right) \tag{A.50}$$

Solution to the above equation may be readily obtained

$$u_\theta^{(2)}=\frac{\sin(2m\theta)}{\left[2K\gamma(1-M_b)\right]^2}\left\{\begin{array}{l}\left[e^{X_r\zeta}\cos(X_i\zeta)-1\right]\Gamma_{\theta,1}+e^{X_r\zeta}\sin(X_i\zeta)\Gamma_{\theta,2}+\left[e^{2X_r\zeta}-1\right]\Gamma_{\theta,3} \\ +\left[e^{2X_r\zeta}\cos(2X_i\zeta)-1\right]\Gamma_{\theta,4}+e^{2X_r\zeta}\sin(2X_i\zeta)\Gamma_{\theta,5}\end{array}\right\} \tag{A.51}$$

with

$$\Gamma_{\theta,1}=\frac{1}{\beta_r}\left(\frac{m}{r}\right)\left[2\left(\delta X_i{}^2-\delta X_r{}^2+X_rM_b\right)\left(\frac{m^2}{r^2}J_m^2-J_m'^2\right)-K^2\left(\delta X_i{}^2+\delta X_r{}^2-X_rM_b\right)J_m^2\right] \tag{A.52}$$

$$\Gamma_{\theta,2}=\frac{1}{\beta_r}\left(\frac{m}{r}\right)X_i\left[2\left(M_b-2\delta X_r\right)\left(-\frac{m^2}{r^2}J_m^2+J_m'^2\right)-K^2M_bJ_m^2\right] \tag{A.53}$$

and,

$$\Gamma_{\theta,3}=\frac{d}{X_r4\left(2\delta X_r-M_b\right)}\left(\frac{m}{r}\right)\left[\left(\frac{m^2}{r^2}+2K^2-\frac{4K^2X_i}{X_r{}^2+X_i{}^2}\right)J_m^2-J_m'^2\right] \tag{A.54}$$

$$\Gamma_{\theta,4}=\frac{-\delta\left[2\delta X_i{}^2+X_r\left(M_b-2\delta X_r\right)\right]}{4\left(X_r{}^2+X_i{}^2\right)\left[4\delta^2X_i{}^2+\left(M_b-2\delta X_r\right)^2\right]}\left(\frac{m}{r}\right)\left[\left(\frac{m^2}{r^2}+2K^2\right)J_m^2-J_m'^2\right] \tag{A.55}$$

$$\Gamma_{\theta,5} = \frac{-X_i\delta\left(M_b - 4\delta X_r\right)}{4\left(X_r{}^2 + X_i{}^2\right)\left[4\delta^2 X_2^{i2} + \left(M_b - 2\delta X_r\right)^2\right]}\left(\frac{m}{r}\right)\left[\left(\frac{m^2}{r^2} + 2K^2\right)J_m^2 - J_m'^2\right] \quad \text{(A.56)}$$

The axial component of velocity is best found through the use of the second order continuity Eq. (2.8). One gets

$$\frac{\partial \rho^{(2)}}{\partial t} = -\nabla\cdot\boldsymbol{u}^{(2)} - \nabla\cdot\left[\rho^{(1)}\boldsymbol{u}^{(1)}\right] - M_b\nabla\cdot\left[\rho^{(2)}\boldsymbol{U}\right] \quad \text{(A.57)}$$

when combined with Eq. (3.31) this becomes,

$$\tfrac{1}{\gamma}p_t^{(2)} - \tfrac{\gamma-1}{2\gamma^2}\left[p^{(1)}\right]_t^2 = -\nabla\cdot\boldsymbol{u}^{(2)} - \tfrac{1}{\gamma}\nabla\cdot\left[p^{(1)}\boldsymbol{u}^{(1)}\right] - M_b\nabla\cdot\left[\tfrac{1}{\gamma}p^{(2)}\boldsymbol{U} - \tfrac{\gamma-1}{2\gamma^2}\left[p^{(1)}\right]^2\boldsymbol{U}\right] \quad \text{(A.58)}$$

The above equation can be further simplified owing to the fact that the first and second order pressure solutions are not functions of z and the mean flow in invariant. Hence,

$$\tfrac{1}{\gamma}p_t^{(2)} - \tfrac{\gamma-1}{2\gamma^2}\left[p^{(1)}\right]_t^2 = -\nabla\cdot\boldsymbol{u}^{(2)} - \tfrac{1}{\gamma}\nabla\cdot\left[p^{(1)}\boldsymbol{u}^{(1)}\right] \quad \text{(A.59)}$$

In terms of the boundary layer coordinate the above equation becomes

$$\frac{\partial u_z^{(2)}}{\partial\zeta} = -\delta\left\{\frac{\partial u_r^{(2)}}{\partial r} + \frac{u_r^{(2)}}{r} + \frac{1}{r}\frac{\partial u_\theta^{(2)}}{\partial\theta} + \frac{1}{\gamma}p_t^{(2)} - \frac{\gamma-1}{2\gamma^2}\left[p^{(1)}\right]_t^2 - \frac{1}{\gamma}\nabla\cdot\left[p^{(1)}\boldsymbol{u}^{(1)}\right]\right\} \quad \text{(A.60)}$$

$$\frac{1}{\gamma}p_t^{(2)} = 0;\ \ \frac{\gamma-1}{2\gamma^2}\left[p^{(1)}\right]_t^2 = 0;\ \ \frac{1}{r}\frac{\partial u_\theta^{(2)}}{\partial\theta} = 0 \quad \text{(A.61)}$$

$$-\frac{1}{\gamma}\nabla\cdot\left[p^{(1)}\boldsymbol{u}^{(1)}\right]=\frac{e^{X_r\zeta}}{2K\gamma^2\left(1-M_b\right)^2}\left(\begin{array}{l}\sin\left(X_i\zeta\right)\left\{\left[\frac{m^2}{r^2}+K^2\left(\delta-1-\frac{2\delta X_i}{\left(X_r{}^2+X_i{}^2\right)}\right)\right]J_m^2+J_m'^2\right\}\\+\cos\left(X_i\zeta\right)K^2\frac{2\delta X_iX_r}{\left(X_r{}^2+X_i{}^2\right)}\end{array}\right) \tag{A.62}$$

$$u_z^{(2)}=\int\delta\left\{\frac{-\partial u_r^{(2)}}{\partial r}-\frac{u_r^{(2)}}{r}-\frac{e^{X_2^r\zeta}}{2K\gamma^2\left(1-M_b\right)^2}\left(\begin{array}{l}\sin\left(X_i\zeta\right)\left[\frac{m^2}{r^2}+K^2\left(\delta-1-\frac{2\delta X_i}{\left(X_r{}^2+X_i{}^2\right)}\right)\right]J_m^2\\+\sin\left(X_i\zeta\right)J_m'^2+\cos\left(X_i\zeta\right)K^2\frac{2\delta X_iX_r}{\left(X_r{}^2+X_i{}^2\right)}\end{array}\right)\right\}d\zeta$$

(A.63)

$$u_z^{(2)}=\frac{-\frac{\delta}{r2K^2\gamma^2\left(1-M_b\right)^2}}{\left(X_r{}^2+X_i{}^2\right)}\left\{\begin{array}{l}\frac{\left(X_r{}^2+X_i{}^2\right)}{4\left(X_r\right)^2\left(2X_r-\frac{M_b}{\delta}\right)}\left[\begin{array}{l}\frac{2m^2}{r^3}J_m^2+\left(\frac{m^2}{r^2}+K^2\right)\left(J'_m{}^2+J_mJ''_m\right)+J'_mJ''_m\\\left(K^2-\frac{3m^2}{r^2}\right)J_mJ'_m+rJ''_m{}^2+rJ'_mJ'''\end{array}\right]\left(e^{2X_r\zeta}-1\right)\\+\left[\begin{array}{l}X_r\left(\begin{array}{l}r\frac{\mathrm{d}\Lambda_{r,1}}{dr}+\Lambda_{r,1}\\+rK\left[\frac{m^2}{r^2}+K^2\left(\delta-1-\frac{2\delta X_i}{\left(X_r{}^2+X_i{}^2\right)}\right)\right]J_m^2\end{array}\right)\\+rKX_rJ'^2_m+X_i\left(r\frac{\mathrm{d}\Lambda_{r,2}}{dr}+\Lambda_{r,2}+K^3r\frac{2\delta X_iX_r}{\left(X_r{}^2+X_i{}^2\right)}\right)\end{array}\right]e^{X_r\zeta}\sin\left(X_i\zeta\right)\\+\left[\begin{array}{l}X_r\left(r\frac{\mathrm{d}\Lambda_{r,2}}{dr}+\Lambda_{r,2}+K^3r\frac{2\delta X_iX_r}{\left(X_r{}^2+X_i{}^2\right)}\right)\\-X_i\left(rKJ'^2_m+r\frac{\mathrm{d}\Lambda_{r,1}}{dr}+\Lambda_{r,1}\right)\\-X_i\left(rK\left[\frac{m^2}{r^2}+K^2\left(\delta-1-\frac{2\delta X_i}{\left(X_r{}^2+X_i{}^2\right)}\right)\right]J_m^2\right)\end{array}\right]\left[e^{X_r\zeta}\cos\left(X_i\zeta\right)-1\right]\end{array}\right\} \tag{A.64}$$

Vita

Sean Robert Fischbach was born in Des Moines, IA on August 17th, 1979. After finishing high school in 1997 he accepted a soccer scholarship to attend Aquinas College of Grand Rapids, MI. In the Spring of 2001 he received a Bachelor of Science degree in Mathematics with a minor in Physics. He later received a Bachelor of Science degree in Mechanical Engineering from the University of Tennessee at Knoxville in the summer of 2003.

In August of 2003 he began graduate studies in the Mechanical, Aerospace and Biomedical Engineering Department at the University of Tennessee Space Institute. From 2003 to 2005 Sean studied Combustion Instability in solid rocket motors under the tutelage of Dr. Majdalani and Dr. Flandro. His Master of Science degree in Aerospace Engineering was completed in May of 2005. Since May of 2005 Sean continued his studies of Combustion Instability but shifted the focus to liquid rocket engines while remaining under the tutelage of Dr. Majdalani and Dr. Flandro. He will be graduating with a Doctorate of Philosophy degree in Aerospace Engineering in December of 2007.